UNIVERSITY OF CALGARY

The Observation and Analysis of the Cepheid SZ Tauri

by

Joseph Edwin Postma

A THESIS

SUBMITTED TO THE FACULTY OF GRADUATE STUDIES

IN PARTIAL FULFILLMENT OF THE REQUIREMENTS FOR THE

DEGREE OF MASTER OF SCIENCE

DEPARTMENT OF PHYSICS AND ASTRONOMY

CALGARY, ALBERTA

NOVEMBER 2007

UNIVERSITY OF CALGARY

FACULTY OF GRADUATE STUDIES

The undersigned certify that they have read, and recommend to the Faculty of Graduate Studies for acceptance, a thesis entitled "The Observation and Analysis of the Cepheid SZ Tauri" submitted by Joseph Edwin Postma in partial fulfillment of the requirements for the degree of Master of Science.

_____

Supervisor, Dr. Eugene F. Milone, Physics and Astronomy

_____

Dr. William J. F. Wilson, Physics and Astronomy

_____

Dr. Denis A. Leahy, Physics and Astronomy

_____

Dr. James Parker, Computer Science, Drama

_____

Date

ABSTRACT

The Cepheid variable star SZ Tauri was photometrically observed at Mount Laguna Observatory in November, 2004, and new elements of its pulsation and physical properties were determined. The pulsation was found to have a period of P = 3.1488 ± 0.0033 days, with an epoch in the Johnson V passband of HJD 2,453,316.5166. Epoch lagging of the UBVRI passbands was discovered, and theoretical analysis and modeling is presented which explains it. This should ultimately lead to improvement in the accuracy of the period-luminosity relationship, as well as lend observational insight into stellar photospheric structure and behaviour. Baade-Wesselink and Balona analyses were carried out with archival radial velocity data, and the radii were determined to be 37.9 ± 2.1 R_{Sun} and 42.5 ± 2.3 R_{Sun} respectively. The Balona radius is suggested as the more accurate of the two. This radius confirms SZ Tau's pulsation mode as being in the first overtone.

ACKNOWLEDGEMENTS

I would like to first thank Dr. Eugene F. Milone for his unlimited patience and understanding throughout the entire course of my tenure as a graduate student at the University of Calgary. His tolerance has allowed me the time to develop extensive expertise in computer programming and data reduction, and allowed exploration of the unexpected results found in the data of this work. It has been my very good fortune to have him as my thesis supervisor.

I would also like to acknowledge the tremendous emotional and spiritual support offered by my very best of friends, Miss Allison J. Foskett. Her positive, shining spirit led a path through the most difficult of times, and I certainly would not have been where I am today without her company. The most important things I have learned as a graduate student, I have learned from her.

In addition, I would like to thank my friend Michael D. Williams for the countless hours, afternoons, and rounds of discussion on topics ranging from stellar pulsation to how to solve all the world's problems! Having Mike as a sounding board to filter and structure some of my more convoluted ideas has been exceptionally valuable in the resolution of some of the lesser-known properties of Cepheid pulsation.

Finally, I would most of all like to thank my parents. The enrichment that only a Friesian couple could provide a child has truly provided for me a strength and perspective of which I am extremely grateful.

DEDICATION

I wish to dedicate this work to my four siblings: Angela, Bart, Alisha, and Peter. I was fortunate enough to have been born in the middle of the gang, giving me the wonderfully enriching experience of being part of an incredibly wide variety of sibling interaction. My life has truly been blessed by their presence.

Angela is a fundamental force of nature – I worry for the man who gets in her way. My earliest childhood memory is of her pointing out Ursa Major to me. Thanks Ang!

Bart is a natural leader, who knows the right thing to do without ever having to question it. He makes an excellent pilot, and is naturally gifted in art, music, and mechanics.

Alisha has always been the cute one, with a great sense of humour and incredibly strong for her size. One of the hardest workers I know (after Angela!).

Peter also has a great sense of humour. And when I say "great" I mean warped – just the way I like it! I think he recently took from me the crown of being tallest in the family…but it's not like anyone was keeping track.

Joseph E Postma

Calgary, June 23 2007

TABLE OF CONTENTS

LIST OF TABLES

LIST OF FIGURES

For everyone must see

that astronomy compels the soul to look upwards

and leads us from this world

to another.

Plato

Chapter 1: Historical Overview

1.1 Development of Modern Theory

The prototype for the class of pulsating stars known as Cepheids is δ Cephei, a star that was first observed to vary in light by a young English astronomer named John Goodricke, on October 19, 1784 (Goodricke 1786). In the following ten months, Goodricke observed the star on at least one hundred separate occasions - reportedly a record in the English clime - but this devotion was ultimately Goodricke's end, as "in the consequence of exposure to night air in astronomical observations" (Fernie 1985)[1], he caught pneumonia and died at the early age of twenty-one, on April 20, 1786. The term "Cepheid" was coined by a Miss Clerke (as cited by Brunt (1913)), who used it to classify short-period variable stars in which the rise to maximum brightness from minimum occupied less than half of the period of variation. This taxonomy has subsequently been changed to include a wider class of stars whose pulsation is due to an envelope ionization mechanism, as described below.

In 1894, Belopolsky (1894) discovered the radial velocity variations of δ Cephei through spectral analysis, and in 1899 Schwarzschild[2] found that changes in the brightness of a Cepheid accompanied changes in the effective temperature. However, this was considered

---

[1] Original source of quotation not specified.
[2] See Fernie, 1985.

evidence that Cepheids were in binary systems, though non-eclipsing. The light and temperature variation was thought to be due to tidal effects from the companion, even though a second spectrum could never be found. However, already by 1879 the German physicist August Ritter[3] had suggested that the variations in light could be due to the radial pulsations brought about via adiabatic changes in the effective temperature, and when Shapley (1914) proposed the pulsation hypothesis as a serious alternative to the other theories, that perspective started to gain wider acceptance. Shapley's reasoning was based on an analysis of observed facts and the known problems with the other theories. For example, the newly developed classification system that sorted stars into dwarfs and giants placed Cepheids well into the supergiant class (based on work by Russell and Hertzsprung), and this placed the theoretical orbits of the companions of Cepheids well inside the Cepheid atmospheres. The light variations of Cepheids then quickly gained acceptance as being due to the dynamical effects of a single star, although the exact physical nature of the effect had to await a fundamental explanation almost fifty years later. However, by 1918 Eddington had published two papers (Eddington 1917, 1918) which brought the pulsation hypothesis to the level of a "major astrophysical theory" (Rosseland 1949). This work was based on the adiabatic pulsations of a gaseous star with a given density distribution, as opposed to a homogeneous star, as in the case of Ritter's earlier work.

Even without a clear understanding of the mechanism of Cepheid pulsation, these stars rose to a centrally important status in astronomy. In 1912, Henrietta Leavitt (Leavitt & Pickering 1912) discovered that Cepheids in the Small Magellanic Cloud showed a clear

---

[3] See Rosseland, 1949.

relationship between period and apparent luminosity. Hertzsprung later used this relation to determine the distance to the Small Magellanic Cloud, Shapley for that to both Clouds and a number of globular clusters, and Hubble for the distance to the Andromeda Galaxy and other galactic systems. This allowed for proof of the existence of extragalactic systems, and almost overnight the dimension of the universe grew to a previously incredulous scale. The study of Cepheids has also shed light on the processes of stellar evolution and stellar atmospheric structure.

The works by Baker & Kippenhahn (1962) and by Cox (1963) and Zhevakin (1963) finally explained the physical cause of Cepheid pulsation in terms of non-adiabatic opacity effects of an ionizing element within the stellar atmospheric envelope. Earlier ground work by Eddington (1941a, 1941b, 1942) had suggested a mechanism similar to this; however, he had identified hydrogen as the crucial element, and also considered core nuclear reactions as being the driving source behind the pulsations, with hydrogen ionization acting as only a damping effect. In fact, nuclear reactions provide only the mean luminosity of the star, and have no effect on surface pulsations due to strong interior damping and due to the highly centralized nature of the nuclear core in the late-type stars to which Cepheids belong (Cox 1985; Epstein 1950). The pulsations actually originate in the outer layers of the star, and the crucial ionizing element was identified as singly ionized helium, He II (Cox 1980).

The envelope ionization mechanism absorbs heat from the layer upon compression, and releases heat upon expansion. Because the source of heat ultimately comes from the luminosity of the nuclear reactions many layers below, the only way to store and lose heat is through modulation of the radiation flowing through the upper atmosphere. A driving mechanism can be set up only in a transition region between quasi-adiabacity and non-

adiabacity (Cox 1985), and where coincidentally there is enough ionizing material (i.e., He II) for the process to have a strong enough physical influence. The lower limit for the concentration of helium is in the vicinity of ten to fifteen percent, with 50% of it being ionized (Kukarkin 1975). The depth of the region of critical He II to He III ionization is that corresponding to a temperature of 35000 to 55000 K (Bohm-Vitense 1958; Zhevakin 1953), which is far above the core nuclear reactions but still well below the radiative photospheric layers. Because this happens at only a very narrowly defined window of effective surface temperature, the "instability strip" on the Hertzsprung-Russell diagram has a nearly vertical orientation, shown in Figure 1-1 below. There is only a minor dependence on the other physical parameters, such as gravity. The instability strip contains almost all the types of pulsating variable stars on the H-R diagram including Cepheid, RR Lyrae, W Virginis, ZZ Ceti, RV Tauri, Delta Scuti, SX Phoenicis, and rapidly oscillating Ap stars. The existence of the red edge of the pulsation instability strip is due to the damping effect of strong convection currents in the cooler stars (Dupree 1977). The existence of the blue edge is due to the surface temperature of such stars being too high for the helium ionization mechanism to occur, such that the ionization region is too close to the surface or doesn't even exist at all.

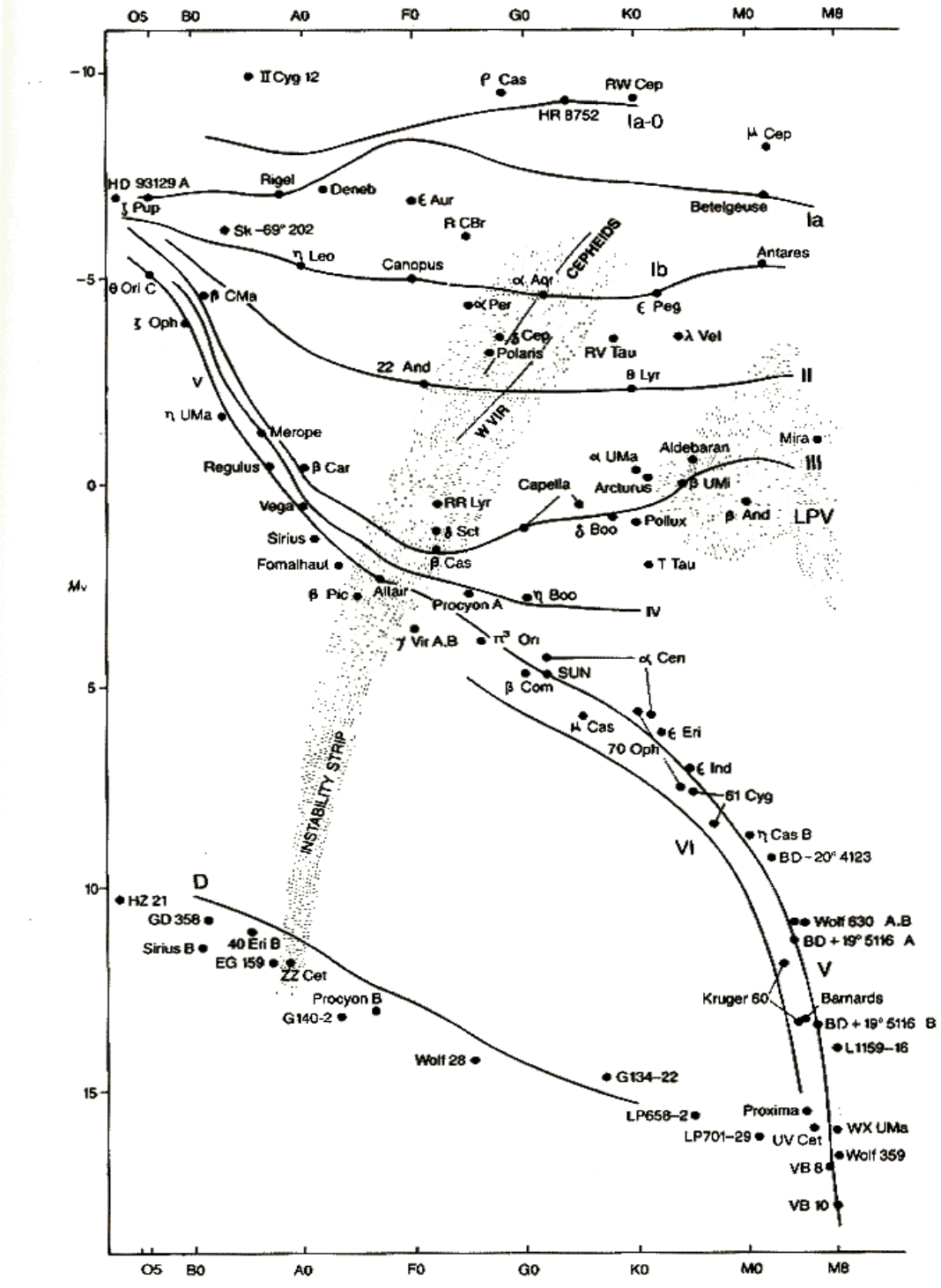

Figure 1-1: Hertzsprung-Russell diagram. The instability strip cuts though almost the entire range of stellar classes. Image source: http://web.njit.edu/~dgary/321/Lecture6.html, copied with permission.

There are ultimately three mechanisms which provide the instability and driving force of Cepheid pulsation. The dominant ionization effect is to provide another degree of freedom to the gas of the atmosphere, so that under compression the energy does not all go to thermal kinetic energy, as it would adiabatically. Therefore, the gas remains relatively cool upon compression and causes the opacity in the region to increase, instead of decreasing as it normally would. Under adiabatic conditions the opacity, commonly referred to as the mass absorption coefficient $\varkappa$ (kappa), varies as $\frac{1}{T^3}$, but due to the ionization the temperature remains relatively constant. But opacity also varies linearly with density, and therefore kappa will increase upon compression. This is referred to as the "kappa mechanism" (Baker & Kippenhahn 1962). The increase of kappa upon compression traps energy inside the region (it ionizes the gas), and causes the pressure upon expansion to be larger than if it had been only adiabatic. The effect "pumps" the pulsation phase as the gas cools by transferring the ionization energy back into the region as radiative and then thermal energy. Second, the relative coolness of the gas causes the layer to radiate less energy, so that it and higher layers compress more easily. This effect is called the "gamma mechanism" (Cox et al. 1966). Lastly, when compressed, the surface area of the star is reduced, so that the total radiation emitted by the star is also less. This serves to further trap the radiation inside the star and pump the cycle upon expansion, and this effect known as the "r (radius) mechanism" (Baker 1966).

The three mechanisms work together to produce a stable oscillation. Suppose some initial, static state of the star and of the critical He II region in particular. Although the region might be initially static, it is not in a stable equilibrium because of the quasi-adiabatic

state induced by the potential ionization of the He II. The region is unstable to pressure and temperature fluctuations. Now upon some perturbation, suppose it to be toward a state of higher compression, the gas partly becomes doubly ionized (He II to He III) instead of only warming. There is then not enough thermally induced counter-pressure to retard the compression, even though the density is increasing. The thermal energy is used to ionize the gas instead. The relative coolness of the gas, its now-smaller surface area, and the local increase in opacity means that less energy is radiated to higher layers, further destabilizing the outer envelope toward compression. But while the region is compressing less energy is radiated outwards from it, and so more energy is trapped below and the radiation pressure builds. This combines with the slowly increasing (i.e., quasi-adiabatically) temperature until a crossover point is reached such that the pressure differential begins to point outwards, and the region then begins to re-expand or "bounce" back. But instead of a simple thermal increase in volume, the expansion gets pumped by the higher than normal radiative pressure from below, and further by the deionization of the gas. The de-ionizing gas provides additional energy, i.e. heat, to the region. This pumps the thermal contribution of the expansion, and so the region becomes unstable towards it. When enough gas has de-ionized and the surface area of the star becomes large enough, the pump disappears and the region again becomes unstable toward compression, thus setting up a repeating cycle (Cox, et al. 1966). The He II ionization mechanism thus acts as an engine, providing heat to the region upon expansion, and absorbing heat upon compression. But this can only occur at the very delicate temperature, compositional, and structural balance of stars of the appropriate mass and position on the H-R diagram.

There are important observational consequences to this mechanism of pulsation, the main one being a de-coupling between the common thermodynamic quantities of density and temperature. Belopolsky (1894) was the first to note the general phase relationship between the radial velocity and light curves for Cepheids – that maximum radial velocity occurs near the time of minimum light. Integration of the radial velocity curve gives the more intuitive parameter of radial displacement. In this form the relation shows that the time of maximum temperature occurs some time *after* the that of minimum radius. However, this relation was not fully appreciated until the pulsation theory gained in popularity, at which point it was thought to present a problem for the theory (Kukarkin 1975; Rosseland 1949). The problem was that, under adiabatic conditions, a state of minimum radius should correspond to one of maximum density. But at maximum density, the thermodynamic temperature should be maximized as well. Further confusion worsened this issue, with the thought that the time of maximum brightness should also correspond to the time of maximum temperature (Rosseland 1949). This confusion may still exist today. However, even if the pulsation was completely adiabatic, maximum luminosity should not occur at maximum temperature. Luminosity is dependent on both temperature and radius, and so will maximize at some time other than either of those parameters' individual maxima.

The modern quasi-adiabatic theory of pulsation and the depth at which the pulsations originate successfully explain the lag of maximum temperature to minimum radius. The heating of the upper layers caused by the deionization of the gas below, which occurs only *after* the star begins to re-expand, can easily be seen to shift the time of maximum temperature to a latter phase. And the depth at which this heating occurs

necessitates a time lag for the process to be reflected in the higher photospheric layers, where the surface brightness and temperature are actually observationally measured.

Already by 1926, however, Baade (1926) had developed a method of testing the pulsation theory of Cepheid variability. First, he correctly recognized that the brightness of the star comes from both temperature and radius. The pulsation theory implied that the changes in brightness were due to changes in both of these quantities. Because the temperature variation could be measured through the colour indices, it was possible to separate the two effects from the luminosity curve and derive a plot of the radial variation with phase. Second, it was possible to independently derive a plot of the radial variation through integration of the radial velocity curve. If the pulsation theory were true, the two plots should, at least qualitatively, agree in phase. As an aside from the test, if the temperature contribution was properly separated from the luminosity curve, it would be possible to derive a radius for the Cepheid as well. For lack of suitable data Baade did not undertake any observational proof of the test, but subsequent work by Becker, van Hoof, and Wesselink (Becker & Strohmeier 1940; van Hoof 1943; Wesselink 1946b) confirmed the pulsation hypothesis by this method.

Bottlinger (1928) had made a first attempt at the test in 1928 using observations of ζ Geminorum, but failed to find the two curves in phase. However, Baade's test required the assumption that stars radiate as blackbodies, so Bottlinger concluded that that assumption was incorrect instead of blaming the pulsation hypothesis. Stars do approximately radiate as blackbodies, but not to the extent needed for an accurate separation of the temperature from the luminosity. Even today, very carefully calibrated colour indices provide a resolution only on the order of 100 K, and this of the same order as a Cepheids' change in temperature.

Both Becker and van Hoof, in separate work, modified Baade's test so that the only assumption required was that there exists a single valued relation between the colour index and surface brightness for all Cepheids. The relation used was that determined observationally for δ Cephei, and was thought to extend to the whole population of Cepheids. Wesselink simplified this latter postulate, stating his "basic assumption" that there is a *unique* relation between colour and surface brightness for *each* Cepheid. This allowed for a more definitive formulation of the radius determination through Baade's pulsational test, and has subsequently become known as the Baade-Wesselink method (Baade 1926; Wesselink 1946a, 1946b, 1946c, 1947). The method has survived in utility to the present day and has extended itself to further simplification and methodology (Balona 1977; Caccin et al. 1981). See Chapter 2 for further detail.

1.2 SZ Tauri

The following table lists all the relevant properties of SZ Tau used and/or calculated in this work.

Quantity	Value	Reference
Current Period (days)	3.1488 ± 0.0033	This work (with MLO photometric data)
Average Period (days)	3.1488236 ± 0.0000015	This work (with O-C analysis)
<U>, <B>, <V>, <R>, <I>	7.96, 7.39, 6.54, 6.04, 5.52 ± .07, .05, .05, .05, .04	This work
ΔU, ΔB, ΔV, ΔR, ΔI	.63, .51, .34, .27, .21	This work
Effective Temperature (K) (max, mean, min)	6284, 6021, 5747 ± 40, 38, 36	This work
Spectral Type (max, mean, min)	F6, F7.5, F9	This work
Luminosity Class	Ib Supergiant	This work
Radius (R_{Sun})	42.5 ± 2.3	This work
Luminosity (L_{Sun})	2138 ± 235	This work
E_{B-V}	0.29	Turner (1992)
Mass (M_{Sun})	5.72	Sanewal & Rautela (1989)

Table 1-1: List of properties for SZ Tauri.

SZ Tau is located on the face of Taurus at right ascension $04^h\ 37^m\ 14^s.78$ and declination $+18^0\ 32'\ 34".91$ (epoch J2000). It has been considered a halo member of the galactic cluster NGC 1647 (Gieren 1985; Turner 1992), although this has been disputed (Gieren, Fouque, & Gomez 1997). It is a short period low-amplitude s-Cepheid which displays that type's characteristic sinusoidal variation in its light curve. The s-Cepheids were classified originally by Efremov (1968) were all Cepheids with sinusoidal light curves; however, the *General Catalogue of Variable Stars* (Khopolov 1985) lists 42 Cepheids with amplitudes less than $\Delta V = 0.5$ magnitudes and almost symmetric light curves, and classifies these as DCEPS (*D*elta *CEP*hei *S*-type)[4]. They are a relatively rare breed of Cepheid. Antonello et al. (1990) proposed that these Cepheids were all first-overtone pulsators, but Platais & Mandushev (1993) report otherwise based on their study of three representative s-types SU Cas, SZ Tau, and V1726 Cyg. They found that of the three, only SZ Tau appeared to be an overtone pulsator, and we will see that the derived radius and measured period in this work confirm that classification. Milone et al. (1999) subsequently determined SU Cas to be an overtone pulsator, but whether or not all DCEPS are overtone pulsators is still open to debate (Sachkov 1997). Overtone pulsation is analogous to the harmonic oscillations of a vibrating string. The fundamental pulsating mode has two fixed nodes at the extremities of the oscillating medium (i.e., the string or atmosphere), and uniform bulk motion of the medium occurs between these two points. For a string, the motion of the pulsation is transverse to the medium, while for a Cepheid atmosphere the motion is radial, i.e., away from and towards the center of the star. The first overtone of pulsation has an

---

[4] Classical Cepheids have asymmetric light curves, larger amplitudes, and longer periods of variation.

additional fixed node midway between[5] the two fundamental nodes, such that uniform bulk motion of the medium occurs above and below the additional central node, but in opposite directions. The extension to even higher modes of pulsation follows obviously. Alcock, et al. (1995) report on 15 beat Cepheids discovered in the Large Magellanic Cloud pulsating in the 2nd overtone; pulsation modes higher than this are not generally expected, but may be possible.

SZ Tau has a long history in the study of Cepheid variables[6]. Its variability was first reported by Schwarzschild (1910), who gave it the provisional designation of 41.1910 Tauri. Hertzsprung initially thought the proper motion of the Cepheid to be similar to that of the Hyades stream, and so the star was considered for further photometric observation by Munch & Hertzsprung because of the possibility that its parallax could be determined. The results of those observations (Figure 1-2) were reported by Schwarzschild (1911), who found the elements for the times of minimum to be $\text{J.D. } 2,418,724.16 \text{ M.E.Z.} + 3^d.1484E$.[7]

[5] In a pulsating medium of uniform density the additional node will occur exactly half-way between the two fundamental nodes; in a medium where density is a function of length, the additional node will generally occur at a point weighted towards the region of higher density.

[6] Though the following is not an exhaustively complete history, it highlights all important developments and includes the best quality data.

[7] "M.E.Z." is Mitteleuropäische Zeit, or Central European Time. "*E*" is the epoch number since JD 2,418,724.16 M.E.Z.

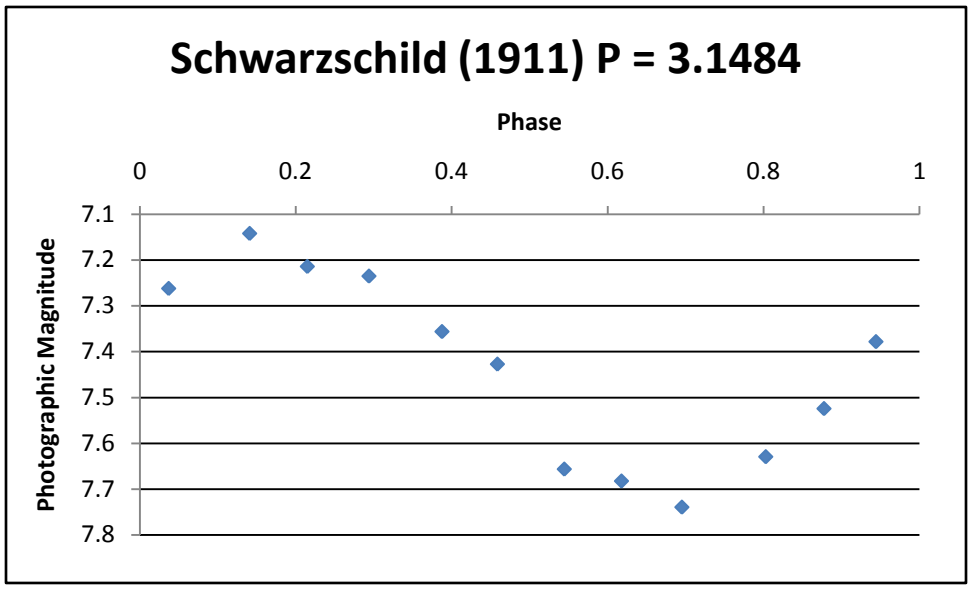

Figure 1-2: Photographic light curve of SZ Tauri by Schwarzschild.[8]

Shapley (1913) subsequently used the 1911 data to explore the hypothesis that the variation in light was due to an axially-rotating ellipsoidal body. Although he did treat the body as a limb-darkened star, he did not put forth an explanation as to how such a star would maintain itself in equilibrium. Although the data could be modeled extremely well with the predicted photometric variation of such a rotating body, simply because SZ Tau's light curve is so nearly sinusoidal, Shapley himself ultimately propounded the pulsation hypothesis as being the best explanation for the cause of the light variations (Shapley 1914). Later the same year however, following Shapley's work, Haynes (1913) further explored the ellipsoidal-body hypothesis using spectrographic radial velocity measurements taken by himself at Mt. Hamilton's Lick Observatory. In addition to establishing that the

[8] It is not clear what epoch was used for the determination of the phases. It may not yet have been customary to place the maximum at phase zero.

spectrographic variations occurred with the same period as the light variations, he noted the radical difference in radial velocity between the Hyades stream and SZ Tau (approximately 40km/s), thus indicating that the star was not likely a member of the stream. Haynes briefly mentions "…it is probable that SZ Tauri should be classified as a Cepheid". He appears to be the first to have done so.

Leavitt and Pickering (1914) followed up the analysis of SZ Tau, using their own archival photographic data from 210 plates taken between 1891 and 1914 at the Harvard College Observatory, to establish a more precise period for the light variation. They reported the elements for the times of maximum as $\text{J.D. } 2,410,000.60 \text{ G.M.T. } +3^d.1487E$, a difference in the period from Schwarzschild's work easily within the error of either's determination (see Table 1-2 on page 22).

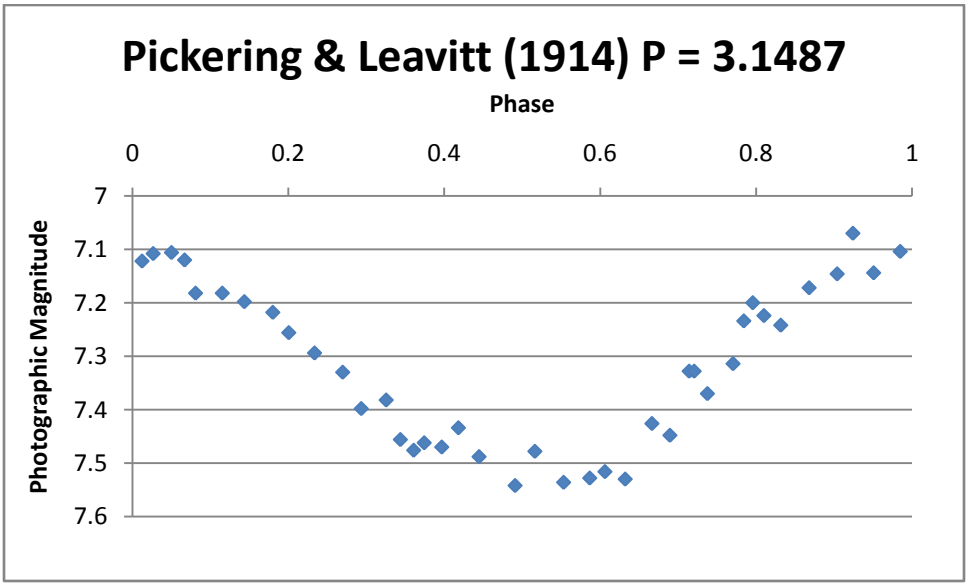

Figure 1-3: Photographic light curve of SZ Tauri by Pickering and Leavitt.[9]

[9] Normal values were computed using averages of every 5 successive points from the 210 observations. A re-determination of the period using the originally published data gives P = 3.14868.

The final "classic" investigation of SZ Tau was done by Shapley (1916), in observations of spectral type variations carried out at Mt. Wilson Observatory, in a set of 20 Cepheids. SZ Tau's classification as a Cepheid was by then widely accepted. Shapley clearly demonstrated that the spectral type of a Cepheid changes in accordance with the periodic light and radial velocity variations of the stars, and says in regards to this that it "…constitute(s) one of the general and fundamental properties of Cepheid variables". Also, "The variation in spectrum of a Cepheid is undoubtedly as important a part of the phenomenon as the fluctuation in light; moreover, it should be as definite a method of detecting a star's peculiar variability as the measures of magnitude." Precise spectral measurements of most astronomical phenomena, including Cepheids, are now fundamental in their study.

Using Pickering & Leavitt's light curve, Shapley superimposed his spectral type classifications at various points throughout the cycle, indicating G spectral type at minimum light, F1 to F0 at maximum light, A9 one-quarter day after maximum light, and reverting to G thereafter with a claimed uncertainty in these determinations of one or two tenths of a spectral interval (Figure 1-4). He indicated that a re-phasing of his data with an increase of 5 seconds in the period would place spectral type A9 a quarter of a day earlier, to coincide with the time of maximum light, and that such a change is well within the uncertainty of the light elements. Indeed, spectral type as a measure of effective temperature would require the hottest type to occur shortly *before* the time of maximum light, because for Cepheids the stellar surface area maximizes approximately 0.3 phase after that.

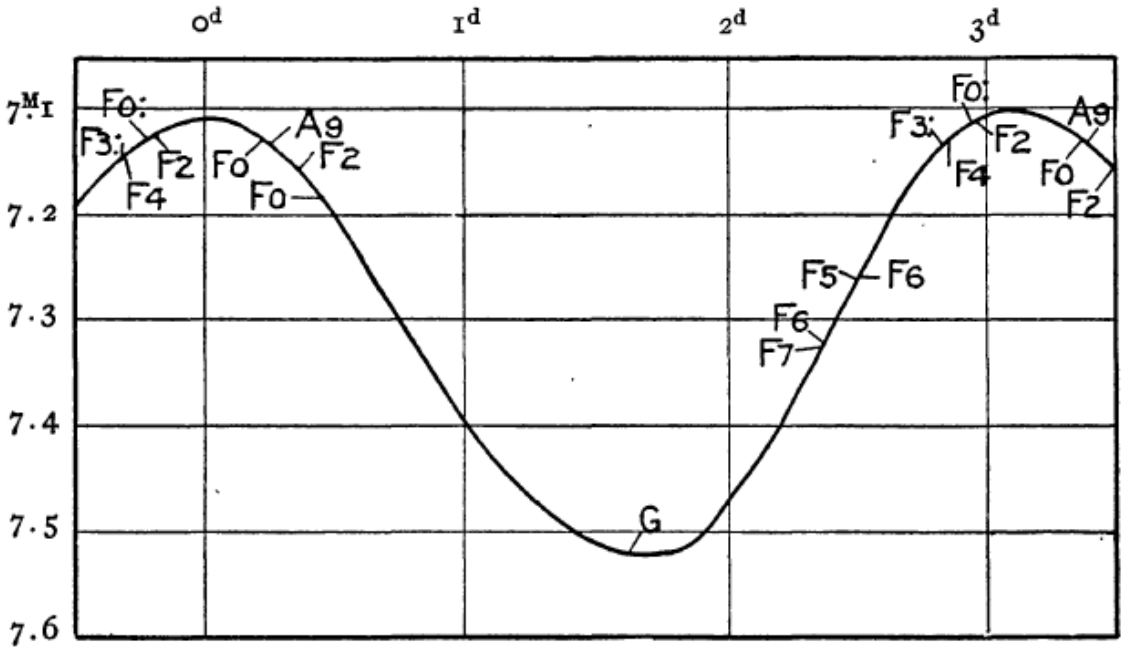

Figure 1-4: Spectral type as a function of period, as determined by Shapley (1916).

Beginning in 1929, Robinson (1929, 1930a, 1930b) undertook an investigation of forty Cepheid light curves utilizing over 30 years of archival photographic data at the Harvard College Observatory. Leavitt had already done this for SZ Tau up to 1914 (Figure 1-3), so if one assumes that Robinson did not include[10] data previous to this time in his determination of a new light curve for the star, the light curve and period determined by him show a marked change from the previous analysis, in that a rise at minimum was manifest at 0.45 phase (Figure 1-5). He also re-reduced Shapley's spectral observations to the Harvard system, correcting their phase by his epoch and period, and these new determinations of spectral type seem to agree with the change of light curve and indicate a possible shift to earlier spectral type during the rise (Figure 1-6). It should be pointed out that Shapley's

[10] Only normal points and phases are listed in his publications, so it is not possible to check the raw Julian dates which make up his data.

observations were done only over SZ Tau's observational cycle of 1915-1916, whereas Robinson's data spans from at least 1914 up to 1930, assuming equal observational density throughout. That the earliest spectral type correctly occurs before maximum light lends credence to the fidelity of Robinson's work. This may indicate that, if the change in the light curve was real, it appeared near or shortly after the time of Leavitt's 1914 analysis and remained a static feature of the oscillation for a long enough period to become evident in the phased light curve data spanning approximately 15 years, or around 1700 cycles. However, Collmann (1930) had measurements of SZ Tau taken visually by himself during the 1927-28 observational cycle (Figure 1-7). There is no discernible rise at 0.45 phase and aside from what are likely outlying data near phase zero, the curve is smooth. If Robinson's rise at minimum was real it seems to have disappeared by 1927 and was the only recorded occurrence of the event.

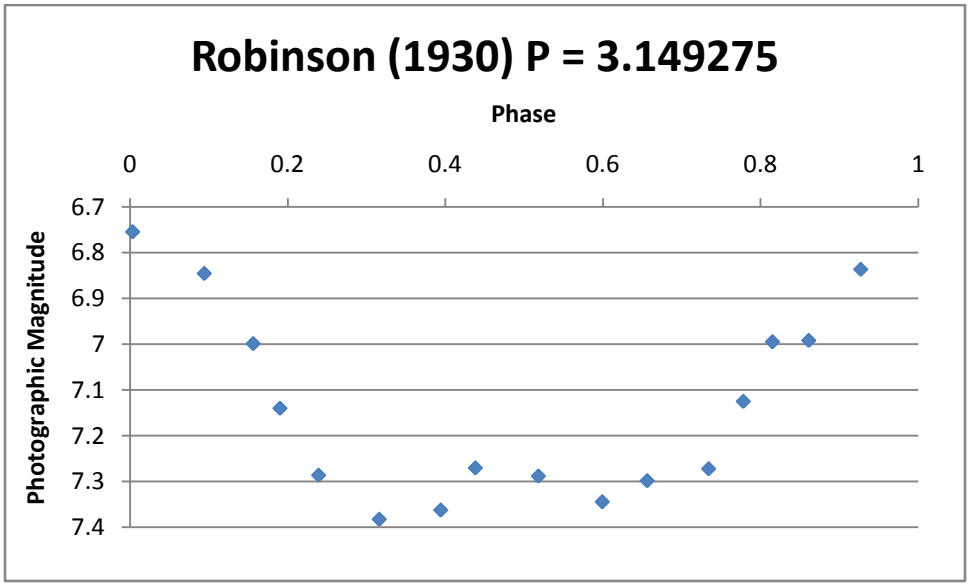

Figure 1-5: Photographic light curve of SZ Tauri by Robinson.[11]

[11] The light curve for SZ Tau seems to have a rise at minimum light during this era.

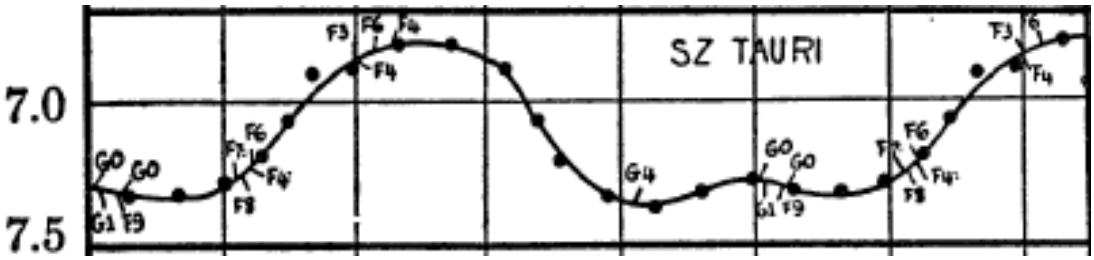

Figure 1-6: Photographic light curve of SZ Tauri with the spectral type superimposed.[12]

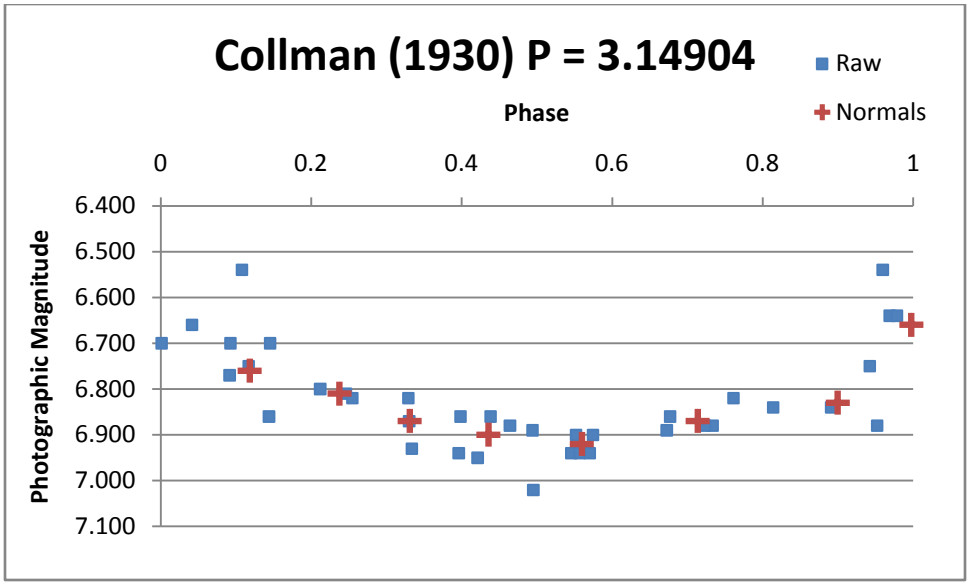

Figure 1-7: Plot of normal points.

The first colour curve for SZ Tau appears to have been determined by Eggen (1951) in a study of 32 Cepheids brought about through testing of a new "photomultiplier for the precise measurement of magnitudes and colors of stars" (Eggen 1950). These also appear to be the first photoelectric data for SZ Tau. He did not compute new light elements for the data, but used those from the 1948 General Catalogue of Variable Stars in the computation

[12] The rise at minimum light may be associated with a change to earlier spectral type.

of the phases. As sparse as the data are, no rise is seen at minimum and the light variation is smooth. He indicates the use of "blue" and "yellow" filters in the determination of the colour curve (Figure 1-8).

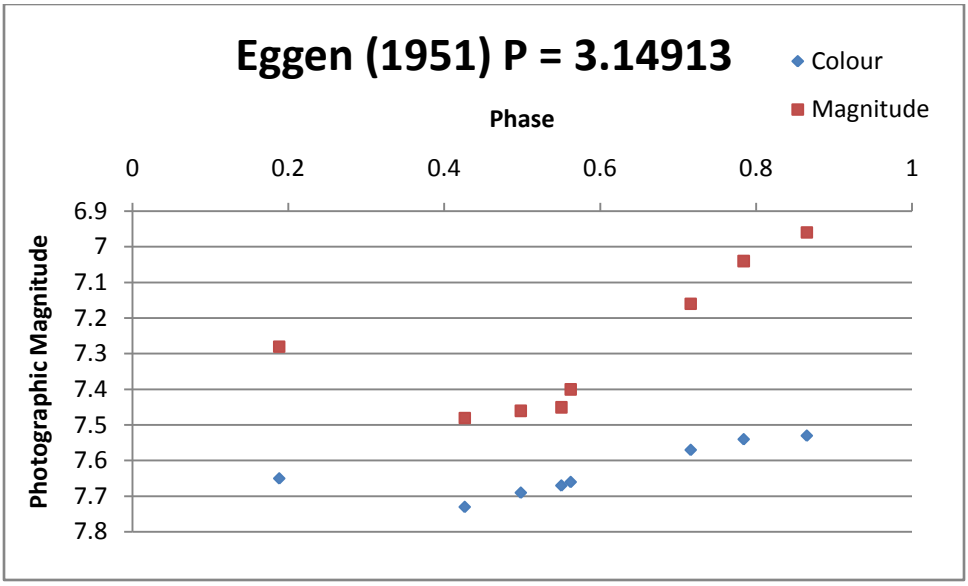

Figure 1-8: Eggen's light and colour curves for SZ tau.

Milone (1967, 1970) and Wamsteker (1972) both have data from the 1965 observing cycle of SZ Tau. Although structure may be found at the minimum of Wamsteker's light curve (Figure 1-10), Milone's excellent photometry clearly shows a smooth variation throughout the pulsation (Figure 1-9). Improperly reduced photometry or observational error may be the simplest explanation for the rise seen in Robinson's data.

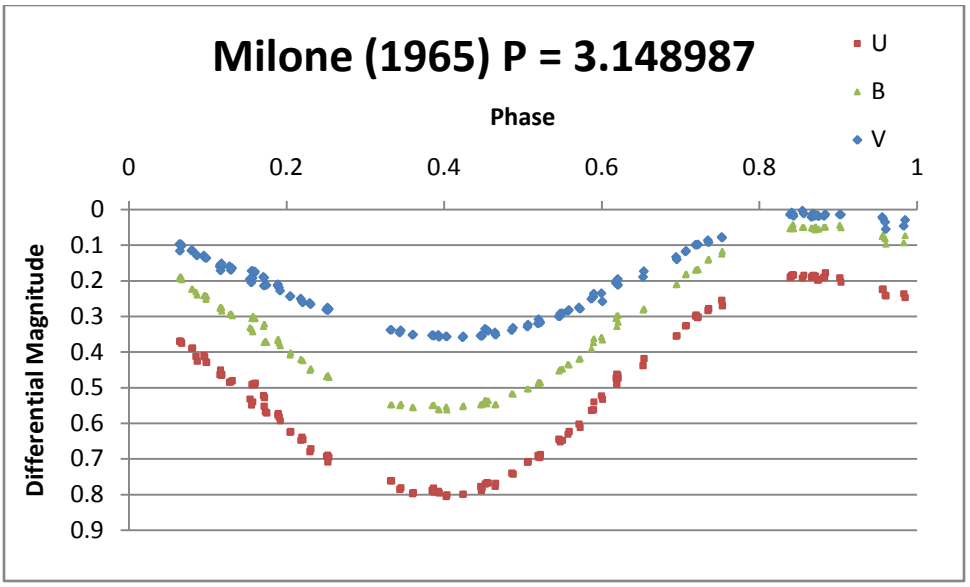

Figure 1-9: Milone's UBV (Johnson) light curves for SZ Tau..

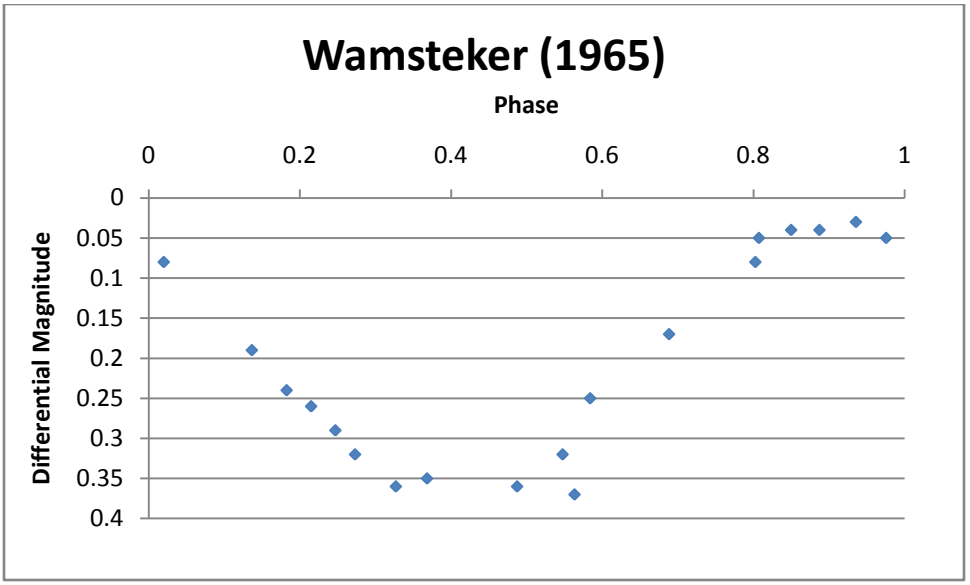

Figure 1-10: Wamsteker's light curve for SZ Tau.

Quality data subsequent to 1965 can be found in Szabados (1977), Moffett & Barnes (1980), Laney (1992), Bersier et al. (1994a), and Barnes et al. (1997). For all published data in

which the Julian Day times of observation were recorded along with the magnitudes, the author has re-determined the pulsational period of the star and listed them, in comparison to the originally determined values, in Table 1-2. The method used to re-determine the period and their errors (where possible) is identical to that as discussed in Chapter 3.1.2.

Reference	Reported Period	Re-determined Period	# of Cycles
Schwarzschild (1911)	3.1484	3.14863	123
Pickering & Leavitt (1914)	3.1487	3.14868	2590
Milone (1965)	3.148987	3.1494 ± 0.0006	12
Szabados (1977)	3.14838	3.1492 ± 0.0004	228
Moffett & Barnes (1980)	3.14873	3.1492 ± 0.0002	263
Laney (1992)	3.14873	3.1495 ± 0.0007	214
Bersier et al. (1994)	3.149138	3.1506 ± 0.0010	29
Barnes et al. (1997)	3.148727	3.1492 ± 0.0005	80
Postma (2004)	(Chapter 3.1.2)	3.1488 ± 0.0033	5
Average[13]	3.1488 ± 0.0002	3.1493 ± 0.0006	-

Table 1-2: Period Determinations for SZ Tauri.[14]

[13] The "Reported Period" average is the mean of its values and the error is the standard deviation; its dispersion is low merely because several values were reported from the same source. The "Re-determined Period" average has weighted each value by the inverse of their errors, and does not include the 1911 and 1914 determinations because no error can be assigned to them.

[14] Schwarzschild's and Pickering & Leavitt's single passband data do not allow for determinations of error on their periods; the determinations are included for reference, however. The periods reported in Moffett & Barnes, Laney, and Barnes et al. came from the GCVS - they were not originally determined.

Almost every author who has studied SZ Tau has commented on an apparently variable period of light pulsation for the star, as is reflected in the 2nd column of the above table. However, this author suspects that the supposed changes in period, based solely on what has been interpreted from the reports in column 2, are perhaps due to nothing more than different treatments of the data. Whereas changes in Cepheid period are expected and have undoubtedly been detected in observations of other stars, for at least the case of SZ Tau the claim is not as well proven as thought. As of 1965 every single period the author re-determined is equal within experimental error, as seen in column three of Table 1-2. It is curious that not a single astronomer, out of the 125 or so references in this report (let alone those in the table), lists or even discusses an error of determination for their reported periods - this actually seems to be the norm. It not surprising then that the "observed" minus "computed" (O-C) times of maximum brightness for SZ Tau show the random residuals as reported by various authors, for example Trammell (1987), Szabados (1991), and Berdnikov (1997).

It is important to appreciate that the methodology by which one determines a period and epoch from a set of data has a significant effect on the result. For example, 2nd, 3rd, 4th or higher order Fourier polynomials can equally be fitted to a light curve depending on the quality of the data and shape of the curve, and each will result in a period which is easily different in the third decimal place. The effect on the calculated time of maximum (the epoch) is then of at least the same error, which will propagate quickly for a star of short period or for any star given a long enough era. The density profile of observations have a significant effect on the computation of the time of maximum also. In Barnes et al. (1997) a gap in the observations of SZ Tau around the time of maximum results in a poor fit of the

light curve around that time, and this ultimately results in an improperly determined epoch and a large O-C residual for those data. Although rates of period change and accuracies of determination may undoubtedly exceed the "noise" introduced by overlooking such issues, for at least the case of SZ Tau one must seriously question the vast majority of reports in which the methodology is not discussed at all, and in which periods and epochs are listed to apparently arbitrary precision and without errors of determination.

One should appreciate also the subtle fact that a period determination from a set of data represents merely the *average* (i.e., best fitting) period for that era. There may well be short term (on the order of one to several epochs) variations in Cepheid period which are smoothed over in what are normally sparse observations over a large number of cycles. The larger error in the period determined from the author's observations covering only 5 cycles (despite being the most excellent quality photometry) of pulsation may be reflective of this, while on the other hand, Leavitt's best fitting period on poor photometry covering 2590 cycles can be quite well determined. Also, while several authors have commented on SZ Tau's "change in period" between Schwarzschild's and Leavitt's original determinations, it appears to be an incorrect assessment: Leavitt's data come from a time span completely overlapping that of Schwarzschild's observations. One must realize that Leavitt's period is only an average over the Leavitt and Pickering data, as is Schwarzschild's period - though, the latter's period is likely less accurately determined because it ranges over a much smaller number of cycles, and is quite likely equal to the former's period within experimental error (as can be seen in column 3 of Table 1-2).

It would seem, to the author at least, quite a remarkable feat of precision if a body as large, tenuous and turbulent as a supergiant star, forty times the diameter of the sun, could

pulsate in its outermost atmospheric layers to a regularity of milliseconds from one epoch to the next, *as opposed to an average value over many cycles*. For pulsars and binary systems, where the moments of inertia which drive the rotation are astronomically large and require equally large opposing forces to counteract, this degree of precision from cycle to cycle is not intuitively unreasonable. Unfortunately, most observing programs of Cepheids are not arranged to take a large number of accurate brightness measurements over *each* cycle of pulsation, but rather take a small number of poorer photometric measurements scattered throughout a large number of cycles - the frequency of observation is almost always much less than one per pulsation cycle. Indeed this is adequate for determining the average period over a large number of cycles and may well lead to a very well determined one, but the knowledge of cycle-to-cycle variations in period (and pulsation profile) is lost. And because this analysis does not seem to have ever been done before, there is an undercurrent of perhaps unjustified belief that a Cepheid variable pulsates to extreme precision in general. This is an issue worthy of further study.

Giving Schwarzschild's and Pickering & Leavitt's re-determined periods reasonable values of error[15], the author computed a weighed line of best fit through all the re-computed periods from Table 1-2; this is shown in Figure 1-11. However, the rate of $\log|\dot{P}| = -0.17$, when $\dot{P}$ is expressed in seconds per year, does not agree very well with the predictions from stellar evolutionary models explored recently by Turner, et al. (2006), for either an overtone

---

[15] Because Pickering and Leavitt's observations cover such a large number of cycles, the data for that era produce a very sharply peaked scatter vs. period curve (as the method in Chapter 3.1.2), resulting in what must be a very well determined average period; the error for the determination was set to 0.0001d. Schwarzschild's re-determined period was given an error magnitude of 0.0004d.

or fundamental pulsator in any crossing of the instability strip. This ambiguity is a common problem for SZ Tau, as the irregular rates of period change reported by Berdnikov & Pastukhova (1995), Trammell (1987), and Szabados (1977) can attest to. The radius derived later in this work does place SZ Tau as an overtone pulsator however, agreeing with results by Barnes et al. (2003), Sachkov (1997), and Turner (1992) for example.

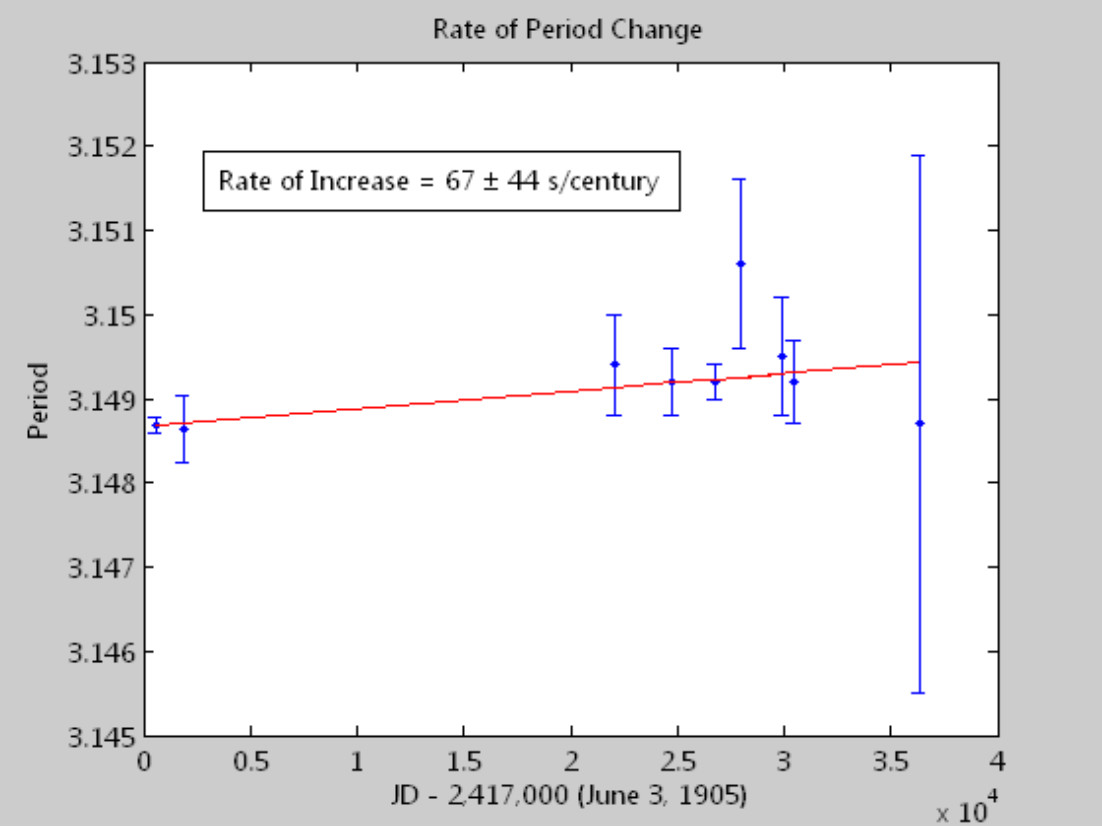

Figure 1-11: Possible rate of period change for SZ Tau.[16]

[16] The error bars are the 95% confidence interval. The Julian Dates are the means from the respective author's dates of observations.

In a personal communication with the author, David G. Turner (of St. Mary's University) kindly provided a spreadsheet tabulation of the results of Berdnikov & Pastukhova's (1995) O-C analysis of SZ Tau. The observed epoch determined in this work was entered into the spreadsheet and can be seen as the last point in Figures 1-12 & 1-13 below. Berdnikov and Pastukhova fit a quadratic polynomial to the O-C data in order to determine a possible rate of period change for the star, and this was repeated by the author with the added data point (Figure 1-12). The downward-facing parabola indicates a negative rate of period change, and its value is -37 ± 4 s/century, or $\log|\dot{P}| = -0.43$ s/year. This would place SZ Tau in the second crossing of the Cepheid instability strip if it is an overtone pulsator (see Turner, et al. (2006)). The average period calculated in the O-C analysis is <P> = 3.1488236 ± 0.0000015 days.

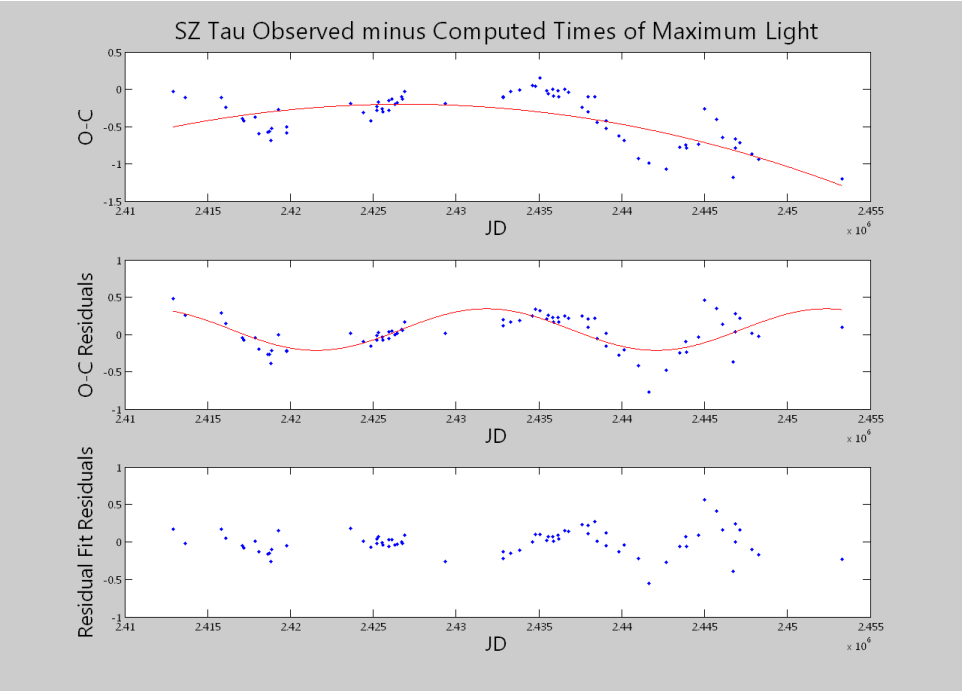

Figure 1-12: Quadratic fit through the O-C determinations of Berdnikov and Pastukhova. The period of the sinusoidal fit to the residuals is 55.9 years.

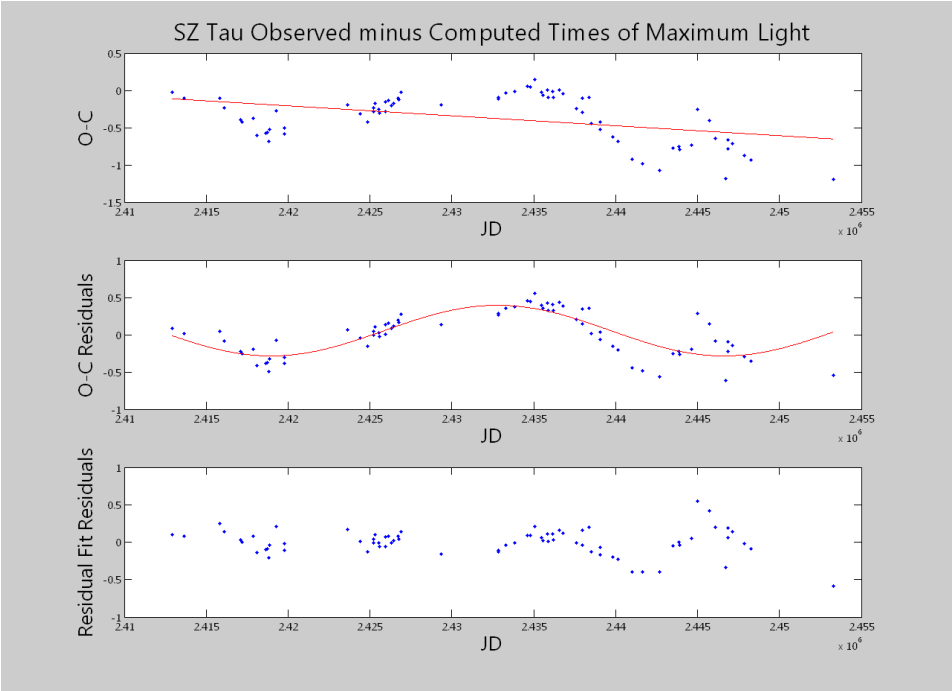

Figure 1-13: Linear fit through the O-C data. The period of the sinusoidal fit to the residuals is 75.7 years.

The residuals of the O-C fits in Figure's 12 & 13 clearly show a sinusoidal oscillation. In Figure 13 a linear polynomial was fit to the O-C data instead, in order to determine if it improved the sinusoidal (i.e., 1st order Fourier) fit of the residuals; the root mean squared error for the linear residuals fit was 0.181, while for the quadratic residuals fit it was 0.167. There is visually very little difference between the two fits, but one might consider the quadratic one to be more physically reasonable as it produces a rate of period change within expected theoretical limits.

A possible explanation for the oscillating residuals is a light-time variation due to a binary orbit about a companion star. Based on the sinusoidal fit in Figure 1-12, however, this hypothesis can be disproven. The period of the oscillation for the quadratic fit is 55.9 years, and Sanewal & Rautela (1989) give an evolutionary mass for SZ Tau of 5.72 M_{Sun}. If we assume a companion of solar mass, Kepler's Third Law gives a semi-major axis for the binary orbit of 27.6 au. On the other hand, the amplitude of the sinusoid oscillation is 0.564 days. Under the binary companion hypothesis, this is the light-time difference between when SZ Tau is closest to us in its orbit and then furthest from us. The amplitude of 0.564 days is equivalent to 97.7 au, and this is will be the diameter of SZ Tau's orbit about the barycenter of the binary system projected perpendicularly to the plane of the sky. If the inclination of the system was near 90^0 there would be (essentially) no projection, and so 97.7 au is the minimum diameter of the said orbit. The radius about the barycenter of orbit for a solar mass companion would then be 5.72x48.85 au = 278.4 au, giving a total minimum semi-major axis of the system of 327.3 au. This result clearly violates the binary companion hypothesis because the minimum semi-major axis computed here must be smaller than the actual one computed through Kepler's Third Law. If we assume a companion mass much

larger than SZ Tau, so that the projected radius of SZ Tau's orbit is *equal* to the total semi-major axis, Kepler's Third Law stipulates a companion of at least 31.6 M_{Sun}. A star of such mass would have a luminosity approximately 10^6 times that of the sun, swamping SZ Tau's luminosity of $10^{3.33}$ L_{Sun}, and would have a life-time of only a few million years. Thus, there is no reasonable solution for which the binary companion hypothesis can be validated using the O-C data, and this agrees with other findings by Evans (1985) and Szabados (1985). One can therefore only suppose evolutionary changes within the star itself as the cause of the O-C residuals. As an overtone pulsator, one may intuitively suspect that the oscillation of SZ Tau would not be as stable as, and would be more suspect to various changes than, a less energetic fundamental-mode pulsation. The worsening with time of the sinusoidal fit to the O-C residuals (the "Residual Fit Residuals" in the bottom panels of Figures 12 & 13 above) may be indicative of a growing evolutionary effect.

Chapter 2: Methods of Analysis

An excellent account of the development of the Baade-Wesselink and Balona methods for determining stellar radii can be found in Gautschy (1987).

2.1 The Baade-Wesselink Method

With the Baade-Wesselink method we wish to determine the phases of equal stellar colour index of a periodic variable star, which as representative of the effective temperature, represent phases of equal stellar surface brightness. If at these two phases there is a difference in the total luminal output of the star as measured through some passband, it must be due to a difference in the stellar radius between the two phases, the implication being that the surface area of the emitting source must be either larger or smaller between them. This leads to a methodology for the determination of the stellar radius in absolute measure. One does not expect changes in metallicity to affect the spectral intensity distribution over the short time scale of Cepheid variability, and for low amplitude radial pulsations pressure effects on the same are also expected to be minor. This is not always the case however, in particular for the usual (Johnson-type) U and B passbands which are sensitive to the ionization opacity variations of the Balmer discontinuity at the typical Cepheid temperatures and pressures. This has naturally been the drive behind the use of longer-wavelength passbands for surface brightness determinations, so as to avoid such

opacity effects when determining the variation in magnitude at such phases. Also, longer wavelength passbands are less sensitive to temperature variations, and more sensitive to radius variations. However, it can be difficult to form accurate colour index curves out of IR data because their amplitude variations are so low, making determinations of phases of equal temperature very poor. This is a crucial requirement for both the Baade-Wesselink and Balona methods. It is ultimately much more important to be able to separate the temperature effects from the photometric data than it is the radial effects; the radial contribution to the light curve is taken into account though the radial velocity data, and so the photometric data should *primarily* be used for the separation of the temperature contribution. Because of the very high sensitivity of the Balmer discontinuity to temperature at typical Cepheid temperatures, one could argue that U-y[17] would make the best colour index for use in the Baade-Wesselink and Balona methods for determining the radius of the star. In any case, it is the radial variation between the two phases of equal surface brightness which is the prominent origin of the magnitude difference between those phases.

That there can be a difference in magnitude at phases of equal colour temperature has a subtle implication for the nature of the radial pulsation: it must follow that the radial displacement curve is not conformal with the colour index variation, so that phases of maximum brightness do not correlate with phases of maximum radius and vice-versa. In effect, there must be a phase lag between the displacement curve and the colour index and light curves, the latter two of which *are* highly conformal to one another (see Figure 3-31 on page 108 for further discussion). The effective temperature is the overriding determiner in

---

[17] Where 'y' is some other, longer wavelength passband. The Johnson U filter transmission profile is centered directly on top of the Balmer discontinuity, making that filter the most sensitive to temperature variations.

the Cepheid's time of maximum brightness, while the radial displacement has a secondary, lower order effect on the filtered-passband light curve. This can be expected because the (bolometric) luminosity is effectively dependent on temperature to the fourth power, while on radius only to the second via the surface area. If there were no phase lag between the radial displacement curve and the colour index, it would not be possible to formulate a methodology based on differences in magnitude since such a condition could never exist.

The derivation of the Baade-Wesselink method is quite simple. In general, the luminal output of a star is dependent on the wavelength of the light observed, its effective temperature, and its radius (i.e., surface area). So

$$L(\lambda, T_{eff}, R) \propto F(\lambda, T_{eff})R^2 \tag{2.1}$$

where L is the luminosity[18], R is the radius, and $F(\lambda, T_{eff})$ is some function representing the surface brightness, and is usually thought to be blackbody but doesn't necessarily have to be. For a pulsating star there is a phase dependence on the temperature and radius parameters, so that $T_{eff} = T_{eff}(\varphi)$ and $R = R(\varphi)$.[19]

If we convert to magnitudes we have

$$m = -2.5\log(L(\lambda, T_{eff}(\varphi), R(\varphi))) + c = -2.5\log(F(\lambda, T_{eff}(\varphi))R(\varphi)^2) + c, \tag{2.2}$$

where the constant of proportionality 'c' has been taken out of the logarithm. Then a difference in magnitude, what will be called here a 'magnitude index' (MI), can be found from

$$m_1 = -2.5\log(L(\lambda_1, T_{eff}(\varphi_1), R(\varphi_1))) = -2.5\log(F(\lambda_1, T_{eff}(\varphi_1))R(\varphi_1)^2)) + c$$

---

[18] Luminosity is generally defined bolometrically, so here the λ dependence on L is to indicate a monochromatic or passband luminosity.

[19] We could perhaps note that, similar to effective temperature, this radius is also an effective radius.

and

$$m_2 = -2.5\log(L(\lambda_2, T_{eff}(\varphi_2), R(\varphi_2))) = -2.5\log(F(\lambda_2, T_{eff}(\varphi_2))R(\varphi_2)^2)) + c,$$

so that

$$MI_{2,1} = m_2 - m_1 = -2.5\log\left(\frac{F(\lambda_2, T_{eff}(\varphi_2))R(\varphi_2)^2}{F(\lambda_1, T_{eff}(\varphi_1))R(\varphi_1)^2}\right)$$

or,

$$MI_{2,1} = -2.5\log\left(\frac{F(\lambda_2, T_{eff}(\varphi_2))}{F(\lambda_1, T_{eff}(\varphi_1))}\right) - 5\log\left(\frac{R(\varphi_2)}{R(\varphi_1)}\right). \quad (2.3)$$

Now when we consider $\varphi_1 = \varphi_2$, so that $T_{eff}(\varphi_1) = T_{eff}(\varphi_2)$ and $R(\varphi_1) = R(\varphi_2)$, but specify $\lambda_1 \neq \lambda_2$, we obtain the commonly known colour index parameter representative of stellar effective temperature. For constant-magnitude non-pulsating stars the radius term in (2.3) is always zero and the temperature is constant with time as well, so that the colour index is a ratio of fluxes at different wavelengths or integrated wavelength passbands. The ratio at these wavelengths can be related to simple model blackbody curves in order to obtain an estimate of the star's effective temperature.

With the surface brightness term being a function of only wavelength and temperature, the Baade-Wesselink method determines phases $\varphi_1 \neq \varphi_2$ but where $T_{eff}(\varphi_1) = T_{eff}(\varphi_2)$, as determined via the colour index curve, which itself *should* not depend on the radius. In this case, the surface brightness term in (2.3) goes to zero and we are left with

$$MI_{2,1} = -5\log\left(\frac{R(\varphi_2)}{R(\varphi_1)}\right). \quad (2.4)$$

As opposed to colour index, (2.4) could be considered a "radius index", as it is a measure of the variation in light due to a variation in radius between the two phases of equal surface brightness. The magnitude difference $MI_{2,1}$ is in this case the variation in magnitude between the two points of phase of equal surface brightness, measured at a *single* wavelength or passband. Differential photometry is therefore wholly sufficient for the purposes here.

Considering the fact that the radius is a periodic function of phase and can be expected to oscillate about some mean radius R_0, we can write $R(\varphi) = R_0 + \delta R(\varphi)$, and substituting this into (2.4) we have

$$MI_{2,1} = -5\log\left(\frac{R_0 + \delta R(\varphi_2)}{R_0 + \delta R(\varphi_1)}\right). \tag{2.5}$$

In Chapter 3.2.3 we see how it is possible to derive $\delta R(\varphi)$ from the radial velocity curve and its integration, and thus we can solve for R_0 from (2.5) and it will be determined via all-measurable quantities. Rearranging (2.5) for R_0 we have

$$R_0 = \frac{\delta R(\varphi_2) - 10^{-.2MI_{2,1}}\,\delta R(\varphi_1)}{10^{-.2MI_{2,1}} - 1}, \tag{2.6}$$

and this is the Baade-Wesselink solution for a periodic variable star's mean radius.

2.2 The Balona Method

The Balona Method is essentially the continuous analog of the discrete Baade-Wesselink method. The Baade-Wesselink method is discrete because only 2 points are chosen at any single time in the solution for the stellar radius, while the Balona method fits a continuous function to the entire light, colour, and radial velocity curves.

We begin as before with equation (2.2),

$$m = -2.5\log(L(\lambda, T_{eff}(\varphi), R(\varphi))) + c = -2.5\log(F(\lambda, T_{eff}(\varphi))R(\varphi)^2) + c.$$

Substituting $R(\varphi) = R_0 + \delta R(\varphi)$ (where R_0 is the mean radius) expanding the logarithm and noting that m is a function of all of its dependants, we have

$$m(\varphi) = -2.5\log(F(\lambda, T_{eff}(\varphi))) - 5\log(R_0 + \delta R(\varphi)) + c. \qquad (2.7)$$

Now $m(\varphi)$ is a measured quantity, i.e., it is a light curve in some filter passband, and in Chapter 3.2.3 we see how it is possible to derive $\delta R(\varphi)$ from the radial velocity curve. We can assume a linear relationship between the surface brightness term $-2.5\log(F(\lambda, T_{eff}(\varphi)))$ and the effective temperature, colour index, and bolometric correction because the range of variation of a Cepheid's effective temperature is small (i.e., the exponential dependence on temperature of the Planck radiation law can accurately be approximated by a linear function). Then $-2.5\log(F(\lambda, T_{eff}(\varphi))) = A \cdot CI + B$, where 'CI' is the colour index between two passbands and 'A' and 'B' are constants, so that

$$m(\varphi) = A \cdot CI(\varphi) + B - 5\log(R_0 + \delta R(\varphi)), \qquad (2.8)$$

where the constant 'c' in (2.7) has been absorbed into 'B'. In the past it was necessary to linearize the logarithm by assuming $\delta R(\varphi) \ll R_0$, converting $\log_{10}$ to $\log_e$ and expanding in order to facilitate iterative linear least-squares fitting of the relevant light and radial velocity curves, but this is no longer necessary as non-linear least squares data fitting algorithms and the computational power to do so now exist. Then (2.8) can be solved numerically (see Chapter 4.2) for the parameters A, B, and R_0, and this is the Balona solution for obtaining a periodic variable star's radius. Equation (2.8) can just as easily be used to derive the Baade-Wesselink result of (2.6), which shows the intimate similarity between the two methods.

See Chapter 4 for discussion and application of the Baade-Wesselink and Balona methods to real data.

Chapter 3: Data Analysis

3.1 Photometric Reduction and Phasing

3.1.1 Differential Magnitudes from the Mount Laguna Observatory

Five colour photometry of UBV Johnson and RI Cousins was obtained for SZ Tauri during a two week observing run at MLO[20] from November 07 through November 20, 2004. The Smith[21] 24" (0.6m) Cassegrain f/20 reflector was used with a thermoelectrically cooled Hammamatsu R943-02 GaAs photomultiplier. Due to SZ Tau's short period of approximately 3.14 days, and 10-hour long nights, the phase coverage for this observing run was nearly complete (Figure 3-1) with small phase gaps occurring at approximately 0.2, 0.52, and 0.84 phase, and with quadruple overlap occurring at 0, 0.4 and 0.7 phase. Inclement and "spotty" weather limited the coverage (Figure 3-2), so that 3 nights of observation as well as some intra-night cloudy periods were lost. However, the quadruple observational redundancy alleviated some of this loss of phase coverage. As will shortly be shown in the data presentation, two coverage gaps of about 0.15 phase span occur centered at 0.5 and 0.8,

[20] Mount Laguna Observatory, San Diego State University, San Diego, California.
[21] Named after Clifford Smith, who founded the SDSU Astronomy Department

at the phases of minimum light and mid-way up the ascending branch of the light curve, respectively.

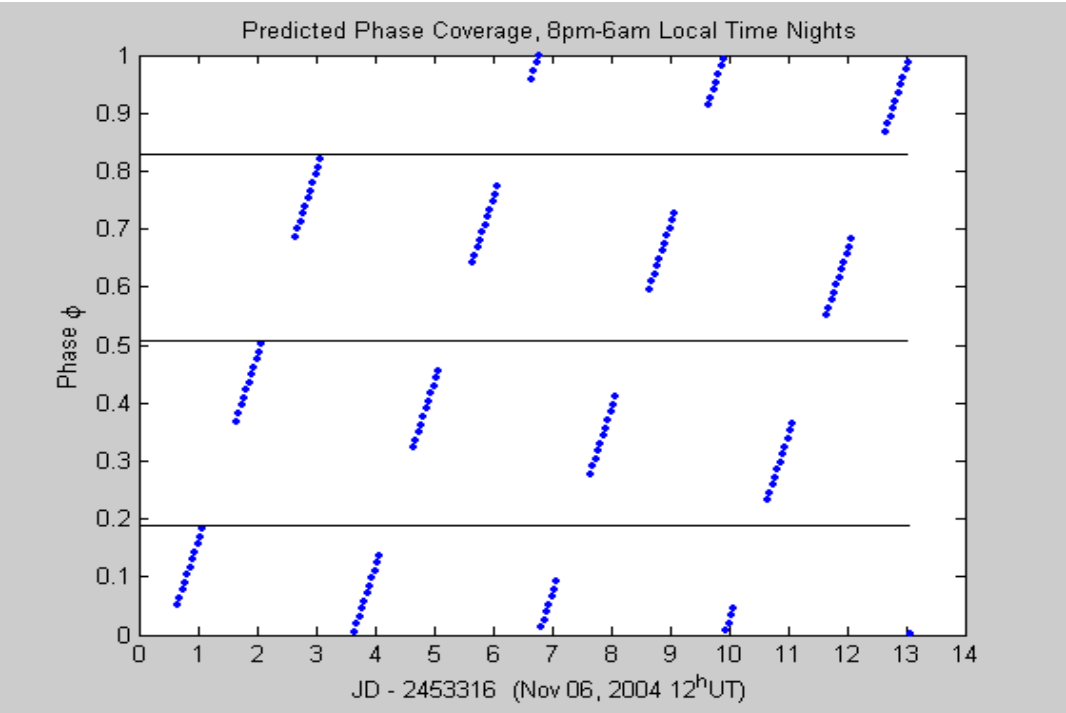

Figure 3-1: Predicted Phase Coverage for MLO run. Observation gaps are denoted by the solid lines.

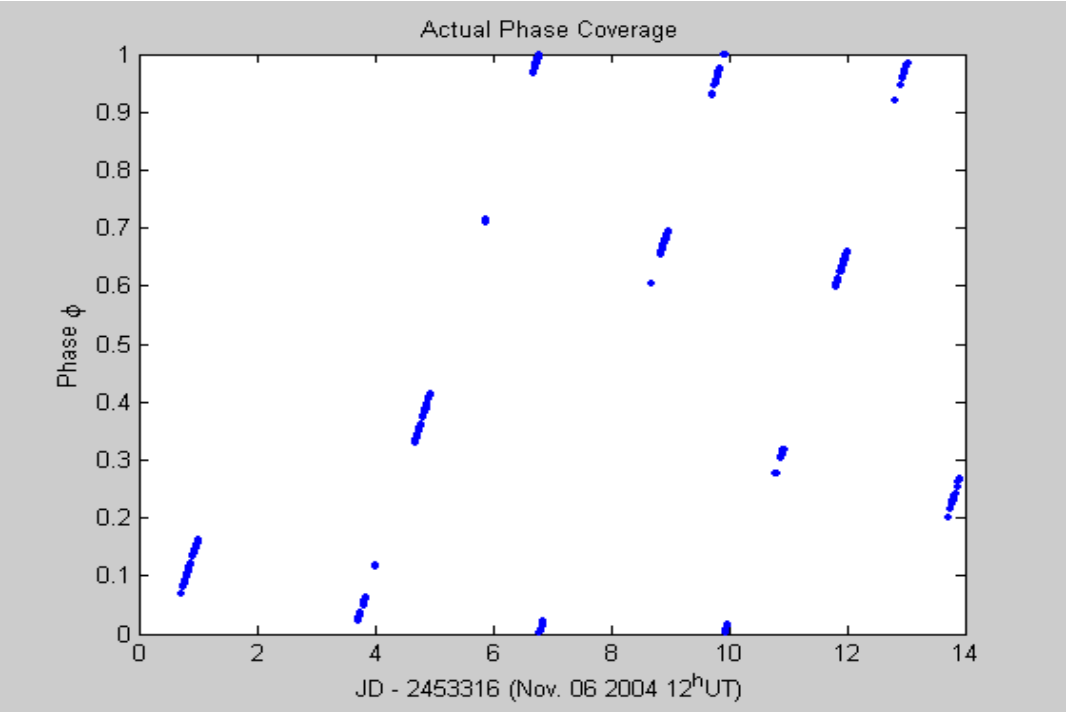

Figure 3-2: Actual Phase Coverage

The comparison star used for the differential photometry was HD 29103 (BD +19 740), an F8 star with V magnitude of 7.25 and B-V of 0.52[22]. This is the same star as used by Milone (1967, 1970) for a check to HD 29104 (BD +19 742) in his photometric investigation of SZ Tau; he found mean-standard-errors (m.s.e.) in the difference between them of ±0.002, ±0.001, and ±0.002 for differential light data in U, B, and V, respectively, and standardized magnitudes of V = 7.262 ± .002, B-V = .549 ± .002, and U-B = .128 ± .002. To obtain UBVRI standardized magnitudes of the comparison star in this work, eight Landolt (1983) standard stars were observed on the night of UT Nov 20, 2004 in order to obtain both extinction and transformation coefficients; the stars are listed below in Table 3-1. Most nights proved insufficiently photometric for purposes of standardization of

[22] Source: SIMBAD Astronomical Database

standard star data, and even this night did not produce highly constrained parameters for the extinction and standardization coefficients; more will be discussed ahead.

Star	RA	Dec	V	B-V	U-B	V-R	R-I
SA 93-332	1 54 17	0 35 48	9.789	0.518	-0.024	0.296	0.306
SA 94-308	2 55 28	0 27 41	8.743	0.494	-0.004	0.29	0.287
SA 95-206	3 53 30	0 14 44	8.737	0.502	0.015	0.29	0.285
SA 97-351	5 56 51	0 13 38	9.783	0.205	0.084	0.124	0.142
SA 114-172	22 42 03	0 09 10	6.969	0.311	0.105	0.187	0.189
SA 114-272	22 42 11	0 19 37	7.737	0.864	0.473	0.48	0.462
SA 96-393	4 51 44	0 00 39	9.652	0.598	0.042	0.345	0.343
SA 99-358	7 53 57	-0 22 10	9.605	0.776	0.509	0.432	0.405

Table 3-1: Stars used for the Hardie standardization.

Pairing	dX	dv	d(b-v)	d(u-b)	d(v-r)	d(r-i)	dV	d(B-V)	d(U-B)	d(V-R)	d(R-I)	d(X(b-v))	d(X(u-b))	d(X(v-r))	d(X(r-i))
332-308	-0.570	0.840	-0.056	-0.217	-0.028	-0.004	1.046	0.024	-0.020	0.006	0.019	-0.608	-1.037	-0.228	0.239
332-206	-0.703	0.971	-0.071	-0.287	-0.031	-0.016	1.052	0.016	-0.039	0.006	0.021	-0.764	-1.351	-0.279	0.272
332-206	0.011	1.040	0.018	-0.006	0.002	0.009	1.052	0.016	-0.039	0.006	0.021	0.032	0.006	0.006	0.006
332-393	-0.542	0.092	-0.155	-0.257	-0.064	-0.068	0.137	-0.080	-0.066	-0.049	-0.037	-0.754	-1.068	-0.281	0.116
308-206	0.581	0.200	0.074	0.211	0.030	0.013	0.006	-0.008	-0.019	0.000	0.002	0.640	1.042	0.234	-0.233
308-206	-0.133	0.131	-0.016	-0.070	-0.003	-0.012	0.006	-0.008	-0.019	0.000	0.002	-0.156	-0.315	-0.051	0.034
308-393	0.028	-0.748	-0.099	-0.040	-0.036	-0.063	-0.909	-0.104	-0.046	-0.055	-0.056	-0.146	-0.032	-0.053	-0.122
206-206	-0.714	-0.069	-0.090	-0.281	-0.033	-0.026	0.000	0.000	0.000	0.000	0.000	-1.827	-1.967	-1.877	-2.012
206-393	-0.553	-0.948	-0.173	-0.251	-0.066	-0.077	-0.915	-0.096	-0.027	-0.055	-0.058	-0.786	-1.074	-0.287	0.110
206-393	0.161	-0.879	-0.083	0.030	-0.033	-0.051	-0.915	-0.096	-0.027	-0.055	-0.058	0.010	0.283	-0.002	-0.156
351-172	0.669	2.961	-0.025	0.166	-0.034	-0.039	2.814	-0.106	-0.021	-0.063	-0.047	0.419	1.144	0.078	-0.424
393-358	0.533	0.121	-0.114	-0.263	-0.048	-0.036	0.047	-0.178	-0.467	-0.087	-0.062	0.422	0.430	0.143	-0.238
272-358	-0.023	-1.871	0.079	-0.016	0.045	0.065	-1.868	0.088	-0.036	0.048	0.057	0.067	-0.057	0.043	0.085
206-172	0.714	1.856	0.271	0.183	0.134	0.110	1.768	0.191	-0.090	0.103	0.096	1.011	1.240	0.406	-0.166
308-172	0.581	1.987	0.255	0.113	0.131	0.098	1.774	0.183	-0.109	0.103	0.098	0.856	0.926	0.355	-0.132

Table 3-2: Pairing values for the parameters in the Hardie analysis.

The extinction equation takes the form

$$y_0 = y - k' \cdot X - k'' \cdot X \cdot c \tag{3.1}$$

where y_0 is the outside-atmosphere magnitude in any passband, y is the observed-system magnitude in any (corresponding to the previous) passband, k' & k'' are the first and second order coefficients respectively, X is the airmass, and c is the observed-system colour index (for example, b-v). The airmasses were computed using the rational polynomial given by Young (1994),

$$X = \frac{1.002432\cos^2(z) + 0.148386\cos(z) + 0.0096467}{\cos^3(z) + 0.149864\cos^2(z) + 0.0102963\cos(z) + 0.000303987} \tag{3.2}$$

where z is the zenith distance of the target; Young claims a maximum error (at the horizon) of 0.0037 airmass. The standardization equation takes the form

$$Y = y_0 + \varepsilon(B-V) + \zeta \tag{3.3}$$

where Y is the standard magnitude in any passband, ε is the standardization coefficient, and $B\text{-}V$ is the standard system colour index. Employing the Hardie (1962) method of differencing pairs of standard stars of similar colour index (from Table 3-1, and then Table 3-2) for determining the coefficients, equations (3.1) and (3.3) become

$$dy_0 = dy - k'dX - k''d(Xc) \tag{3.4}$$

$$dY = dy_0 + \varepsilon d(B-V). \tag{3.5}$$

Generally, the outside-atmosphere magnitudes dy_0 are not known in advance, and so the two above equations can be combined to give

$$dY = dy - k'dX - k''d(Xc) + \varepsilon d(B-V). \tag{3.6}$$

The parameters *dY* and *d(B-V)* are the previously known standard star data, while *dy*, *dX*, and *d(Xc)* are the measured quantities, and so equation (3.6) can be solved for k', k'' & ε through linear least squares. In Matlab, the backslash operator effects the linear regression

$$[k' \; k'' \; \varepsilon] = [-dX \;\; -d(Xc) \; d(B-V)] \backslash (dY - dy) \tag{3.7}$$

where all the input parameters are column vectors, and the output estimators are scalar values. The error matrix was formed to obtain the standard errors on the estimators, such that

$$E_{kl} = \sqrt{H_{kl}^{-1}} \tag{3.8}$$

$$H_{kl} = \frac{\partial^2}{\partial\theta_k \partial\theta_l}\left(\frac{1}{2}\sum\left[\frac{dY_i - (dy_i - k'dX_i - k''d(Xc)_i + \varepsilon d(B-V)_i)}{\sigma_i}\right]^2\right) \tag{3.9}$$

where $\theta_{(k,l) \; = \; 1,2,3}$ are the estimators k', k'' & ε from (3.7), and σ_i are the errors in measurement. Typically, it is best to use the differences between each known value of *dY* and their values computed through equation (3.6) (the bracketed quantity in the numerator of equation (3.9), after the estimators have been found via equation (3.7)) for the σ_i errors in measurement; the scalar-valued standard deviation of the differences can alternatively be used so that $\sigma_1 = \sigma_2 = \ldots = \sigma_n = \sigma$. Evaluation of equation (3.9) leads to the symmetric square matrix

$$H = \begin{bmatrix} \sum\frac{dX_i^2}{\sigma_i^2} & \sum\frac{dX_i \cdot d(Xc)_i}{\sigma_i^2} & -\sum\frac{dX_i \cdot d(B-V)_i}{\sigma_i^2} \\ \sum\frac{dX_i \cdot d(Xc)_i}{\sigma_i^2} & \sum\frac{d(Xc)_i^2}{\sigma_i^2} & -\sum\frac{d(Xc)_i \cdot d(B-V)_i}{\sigma_i^2} \\ -\sum\frac{dX_i \cdot d(B-V)_i}{\sigma_i^2} & -\sum\frac{d(Xc)_i \cdot d(B-V)_i}{\sigma_i^2} & \sum\frac{d(B-V)_i^2}{\sigma_i^2} \end{bmatrix} \tag{3.10}$$

and then the diagonal elements $k = l = 1, 2, 3$ of equation (3.8) are the standard errors for k', k'' & ε, respectively. Finally, ζ is determined by evaluating equation (3.1) and then solving (3.3) for the mean value and standard deviation of ζ. In the evaluations of equations (3.1) though (3.10) the observed-system colour index $c = b\text{-}v$ was used for all passbands; using passband-colour pairings of *u* & *u-b*, *b* & *b-v*, *v* & *b-v*, *r* & *v-r*, and *i* & *r-i* did not significantly affect the results, which are listed in Table 3-3 below along with the ensuing standard magnitudes calculated for the comparison star. The UBV values match well within their error to the values as determined by Milone (1970).

Filter-Colour	**k'**	**k"**	**ε**	**ζ**	**HD 29103**
U, B-V	.733±.044	-.047±.017	-.028±.085	19.315±.034	7.89±.07
B, B-V	.412±.032	-.079±.015	.022±.050	20.019±.035	7.79±.05
V, B-V	.286±.028	-.081±.015	.018±.075	20.249±.034	7.26±.05
R, B-V	.234±.018	-.078±.012	-.036±.074	20.230±.031	6.94±.05
I, B-V	.212±.026	-.086±.016	-.064±.040	19.482±.032	6.64±.04

Table 3-3: Extinction and transformation coefficients, and standard magnitudes of the comparison star.

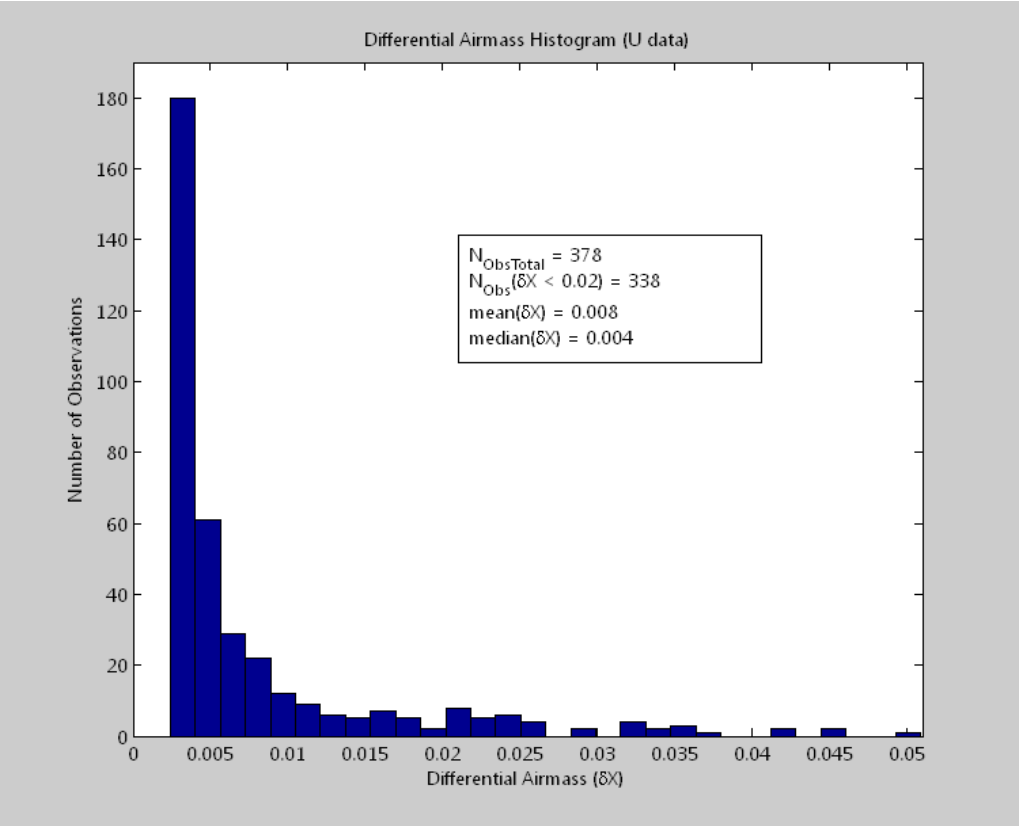

Figure 3-3: A histogram of the differential airmasses shows that most observations were done well below δX = 0.02.

The errors on the parameters in Table 3-3 are quite large, and the resulting precision of the UBVRI magnitudes for HD 29103 would not generally be considered high enough to conclude that the star is constant, hadn't it already been previously determined. In the end, most nights were not of high enough photometric quality to allow the use of the first order coefficients from Table 3-3 for all of them, and so each night was treated separately for those using the Bouguer method as described below. Fortunately, the difference in air mass between SZ Tau and HD 29103 was quite small (as shown above in Figure 3-3) so that the differential extinction effects were minimal.

A graphical user interface program called MLOphot[23] was written to assist in the reduction of the raw SZ Tau and HD 29103 count data into differential magnitudes. The data output stream from the photometer contained 5 columns; in order they were exposure count, universal time, exposure time, a miscellaneous entry, and a filter/object combination code. The filter/object combination code is used for sorting through the data rows in order to find the observational results of a specific filter for a particular object. For example, the UBVRI filters were coded 1 through 5 respectively, while the star object, comparison object, sky object, and check object were numbered 1 through 4, respectively. Therefore, to find all of a particular data file entries corresponding to the star counts in "U", one simply searches the filter/object column for all entries equal to "11" and then cross-references these indices to the other data columns. In this way the target star counts, comparison star counts, sky counts and their times of observation can easily be extracted by computer software from the large file containing all the night's data.

MLOphot allows one to interactively fit smoothing splines to the background sky counts and the comparison star counts for subtraction and division from the target star data. Only the background sky count is subtracted from the comparison star data. First, a best fit is visually estimated for the sky counts (Figure 3-4, top panel) by varying the smoothing factor of the smoothing spline fitting function. A smoothing spline is the best fitting function to use for these purposes because the variations in background brightness and atmospheric transparency, although smooth, cannot be expected to be non-pathological[24]. We are thus limited to interactively determining the best smoothing factor because an

---

[23] Created using Matlab's Graphical User Interface Development Environment, called GUIDE.
[24] Pathological (in present context): as in not being well represented by any known analytical function.

automated least squares routine would not work. It is also appropriate to have curvature between the data points, because this likely mimics the natural variation of the sky more reasonably than simple straight-line interpolation.

Once a satisfactory curve is fit to the background sky data, MLOphot automatically computes the interpolated sky counts at the midpoint of the times of the target star and comparison star exposures, and then subtracts those values from the target star and comparison star data.

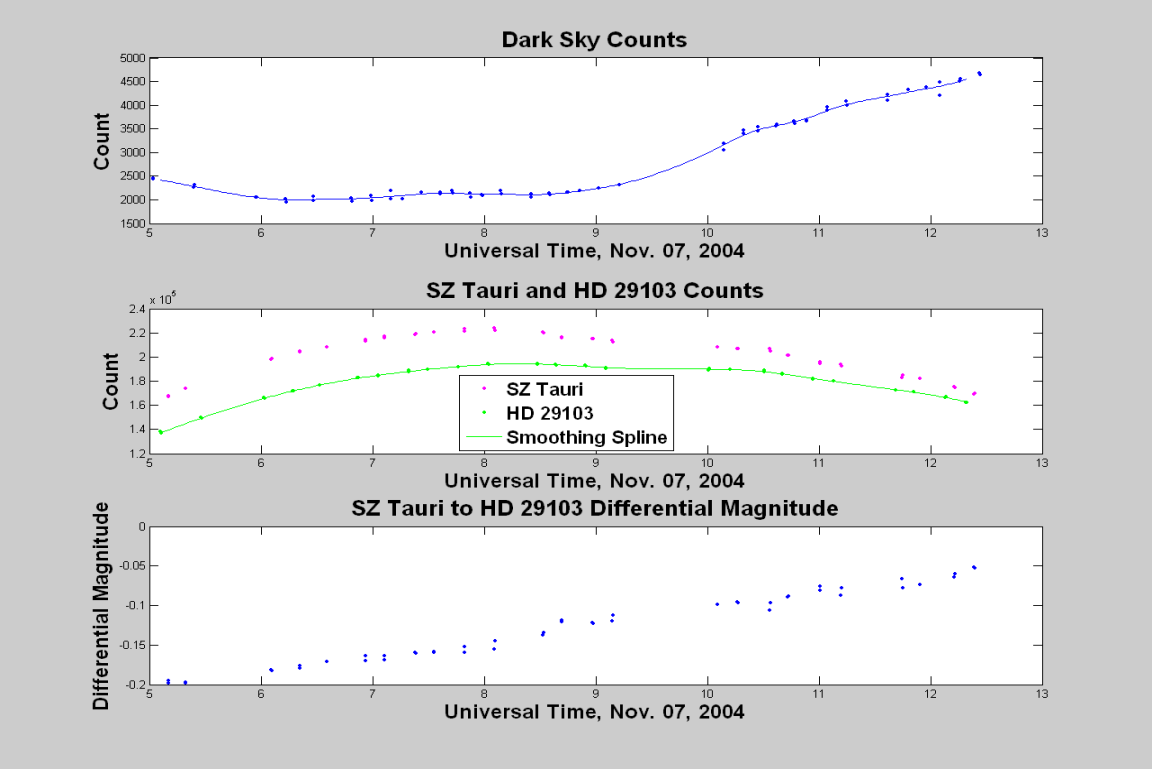

Figure 3-4: Example of MLOphot

The next step essentially repeats the first, but now the fitting procedure is applied to the comparison star data. One should note the smooth variations of the background sky

counts and comparison star counts in Figure 3-4, indicating that this particular night was clear and stable with perhaps some transparency variation beginning at 8:30 hours UT, as evidenced by the variation in the comparison star curve as well as the increasing level of background sky light contributing to the increase in the rates thereof. The comparison star counts are then interpolated to the times of observation of the target star data using the smoothing spline fit, and these values along with the target star counts are recorded and used for the differential photometry.

The raw differential magnitudes are computed using

$$dm = -2.5 \log_{10} \left(\frac{Star\ Count}{Comparison\ Count} \right), \tag{3.11}$$

which converts the counts into un-standardized differential ground-magnitudes, and then the outside-atmosphere differential magnitudes are computed using the differential extinction equation of (3.4), where now the differences are between the measured quantities for SZ Tau and HD 29103. For each night of observations, the first-order extinction coefficient was calculated using the Bouguer method of plotting the constant-star magnitude vs. its airmass, and then determining the slope of the line of best fit for the first-order extinction coefficient. The quality of the observations is evidenced in that the difference between this set of differential data and published standard data for SZ Tau is a simple zero-point offset (as seen in section 3.1.3), which is entirely expected for *any* differential data. This is wholly inconsequential because the solutions to the Baade-Wesselink and Balona methods require only differences in magnitude in their solution, which thereby negates the need for knowledge of the zero-point and the need for full photometric zero-point standardization. This is clarified in the chapters on the Baade-Wesselink and Balona

methods. Lastly, the times of observation were all converted to the heliocentric frame using standard algorithms[25], and Appendix B contains the complete listing of the reduced photometric data.

[25] As such found in The Astronomical Almanac; see Appendix A for a Matlab script.

3.1.2 Procedures in Periodicity, Phasing, and Epoch Determination

With data reduced to differential magnitudes it is possible to determine the periodicity of the variations, assuming they are uniform. Certainly, periodicity has no meaning for non-uniform variations and in that case one might be more interested in the frequency components of the pulsation instead. We begin by finding an estimate for the period by performing Fourier fits of various orders to the differential magnitude curves vs. their heliocentric Julian times of observation. Any data reduction package worth its merit can readily perform these fits instantaneously and visually, as is the case for Matlab. The data must be treated interactively because it is difficult to determine which order of fit (in this case a Fourier fit) is the best to use for representing the data. Similar to fitting higher order polynomials, the higher the order of Fourier fit the greater the number of data points the fitting curve will pass through, reducing the root-mean-square scatter of data points about the fit. This cannot be interpreted to mean, however, that higher orders produce better quality fits – it is quite the contrary. It is up to the researcher to determine the best order fit through interactive, visual analysis. Fourier fits are especially dangerous as high orders can produce beats and resonances which are physically completely nonsensical. Figure 3-5 shows that reasonable Fourier orders give a period of around 3.146 days, and this can be used as a starting point for a more detailed analysis.

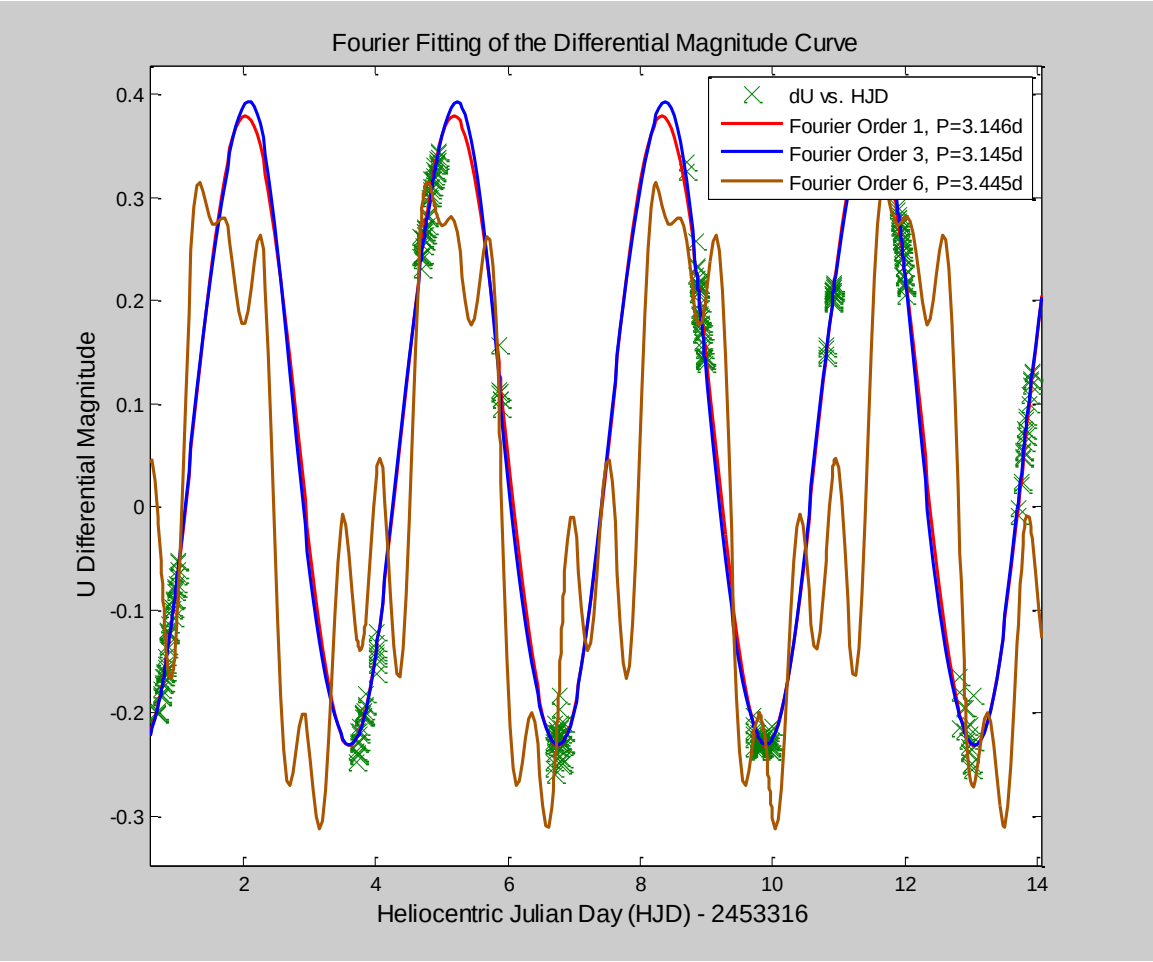

Figure 3-5: Sample of 3 Fourier fits to the U differential light curve.

The data are then phased using

$$\phi = \frac{HJD}{Period} - floor\left(\frac{HJD}{Period}\right)^{26}, \tag{3.12}$$

where ϕ is the phase which will vary between 0 and 1, *HJD* is the Heliocentric Julian Day, and the period is the initial estimate found above. The data are now Fourier-fitted at various orders in order to determine the best order. One should choose a fit of high enough order

[26] The "floor" function is simply the integer part of its argument. This form of the phase equation temporarily ignores the epoch starting point.

so that the low amplitude frequencies are accounted for, but of a low enough order so that high frequency components are not inadvertently introduced (as can be seen for Fourier order 6 in the last figure).

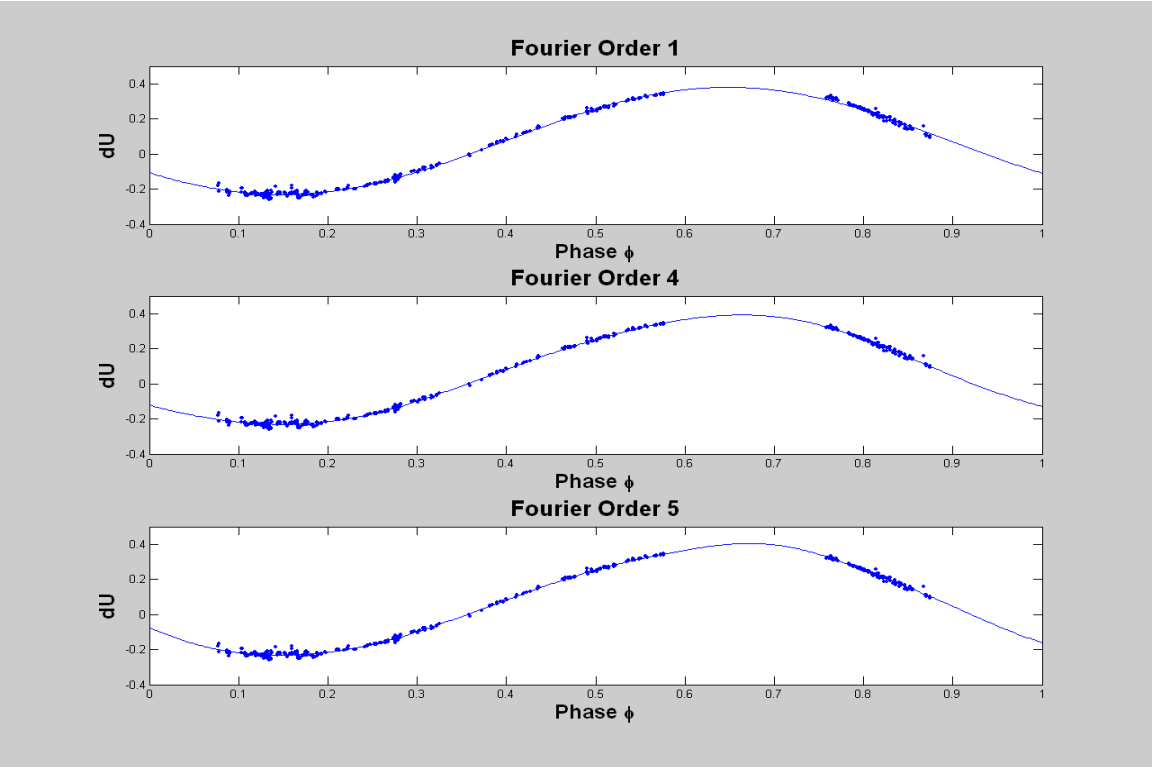

Figure 3-6: Fourier Order 4 seems to be the best choice of order to represent the phased data.

The top panel of Figure 3-6 illustrates how fitting with too few frequency components in the low order Fourier fit does not adequately represent the data, as there is noticeable skew between the fitting curve and the data in the region bracketing 0.8 phase. In the bottom panel, fitting with too many frequency components creates the oddly shaped or 'out-of-round' curve observed in the data gap surrounding 0.68 phase, which one has no physical reason to expect. The periodicity is also not well reproduced in that the curve does

not return to the same values at 0 and 1 phase. The center panel of Figure 3-6 shows a satisfactory Fourier fit of order 4, adequately modeling the data as well as properly reproducing the periodicity. The fits were not constrained in period in the above analysis; at this point we are only determining the best Fourier order to use for the representation of the data. An arguably more quantitative method for determining the correct order for the Fourier fit is to examine the error on the fit parameters: when the order of the fit is too high, the higher order coefficients will not be significant as compared to their errors. This method would lend itself very well to automation inside a computer program.

With an appropriate Fourier order selected, it is possible to determine a much more accurate period for the star's cycle of pulsation. A range of periods of 101 points, spanning 0.05 days and bracketing the initial period estimate of 3.146 days, are used to re-phase the data and Fourier fits of the chosen order are determined for each. The periods are highly constrained (to $\pm 10^{-12}$) in the Fourier fit in order to force the fit to use each period as its fundamental frequency. For each of the periods and their Fourier fits, the summed RMS[27] of the residuals is recorded and the sequence of these is plotted against their corresponding period. The trend of the RMS verses period graph will have a minimum at the best fitting period, and Figure 3-7 shows an example for the U passband. Essentially, the period which phases the data to the least RMS scatter about the fit is assumed to be the period which best models the pulsation.

---

[27] RMS is the root-mean-square.

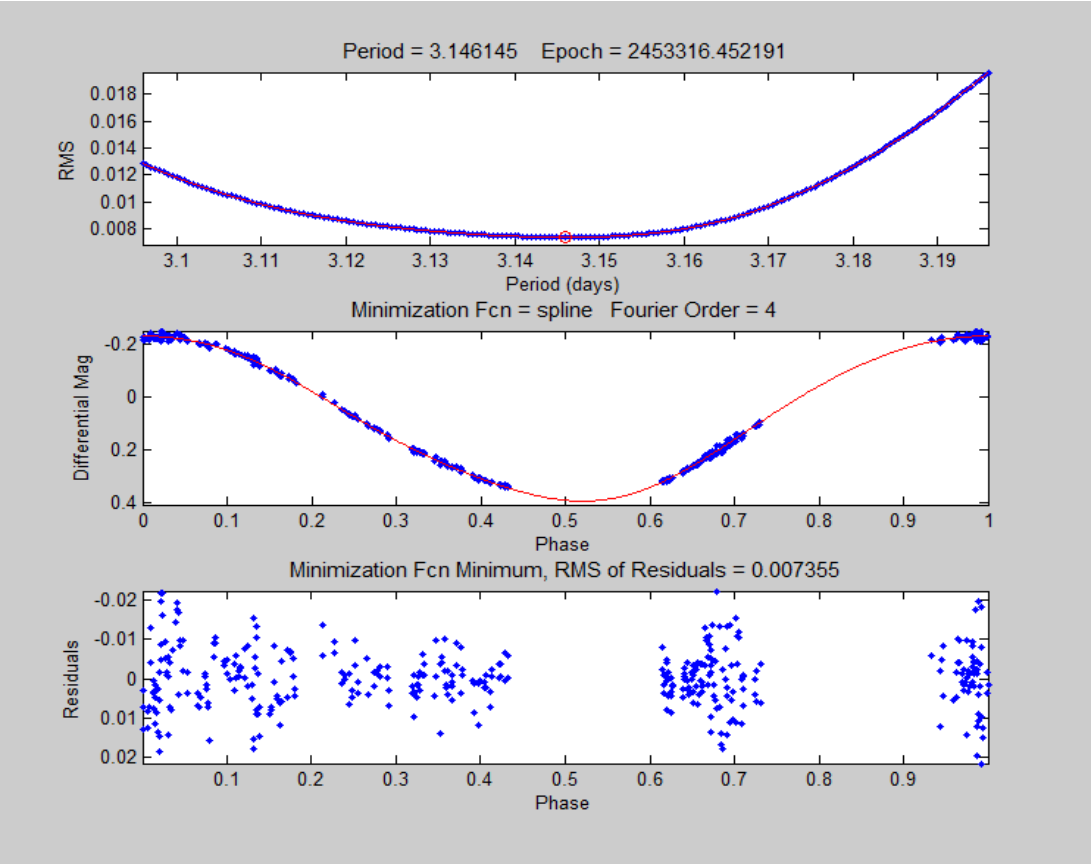

Figure 3-7: RMS vs. Period. The minimum of the trough in the top panel gives the period of least squares fit.

Data sets which cover a much larger number of epochs (as illustrated in Chapter 1.2) typically have a much more sharply defined minimum in the RMS vs. period curve than that found in the top panel of the above figure. This lends credence to the possibility that epoch-to-epoch variations in period may be quite real and much larger than the variations in average period over a large number of cycles (see the discussion following the table on page 22). A sharper minimum vertex allows for a smaller bracketing range of the 101 periods, and therefore, smaller spacing between RMS evaluations and a (presumably) better determined minimum. Too small a bracketing range, however, will in all cases produce random point-to-point noise in the RMS vs. period curve of such a magnitude as to render it impossible to

fit. In any case, the plot of RMS vs. period is typically quite pathological, making it difficult to fit with an analytic function; polynomials of even 10^{th} order are inadequate. It is important to properly fit the curve with a function because one must then use that function to find its minimum, using some minimization algorithm. Cubic spline interpolating polynomials have been found to work best, and Matlab can readily create and then minimize the polynomial structure to any arbitrary precision. The procedure is carried out for each of the five UBVRI light curves, and the mean and standard deviation of the results are used as the period and its error. The results for the UBVRI data from MLO are shown below in Figure 3-8 and tabulated in Table 3-4.

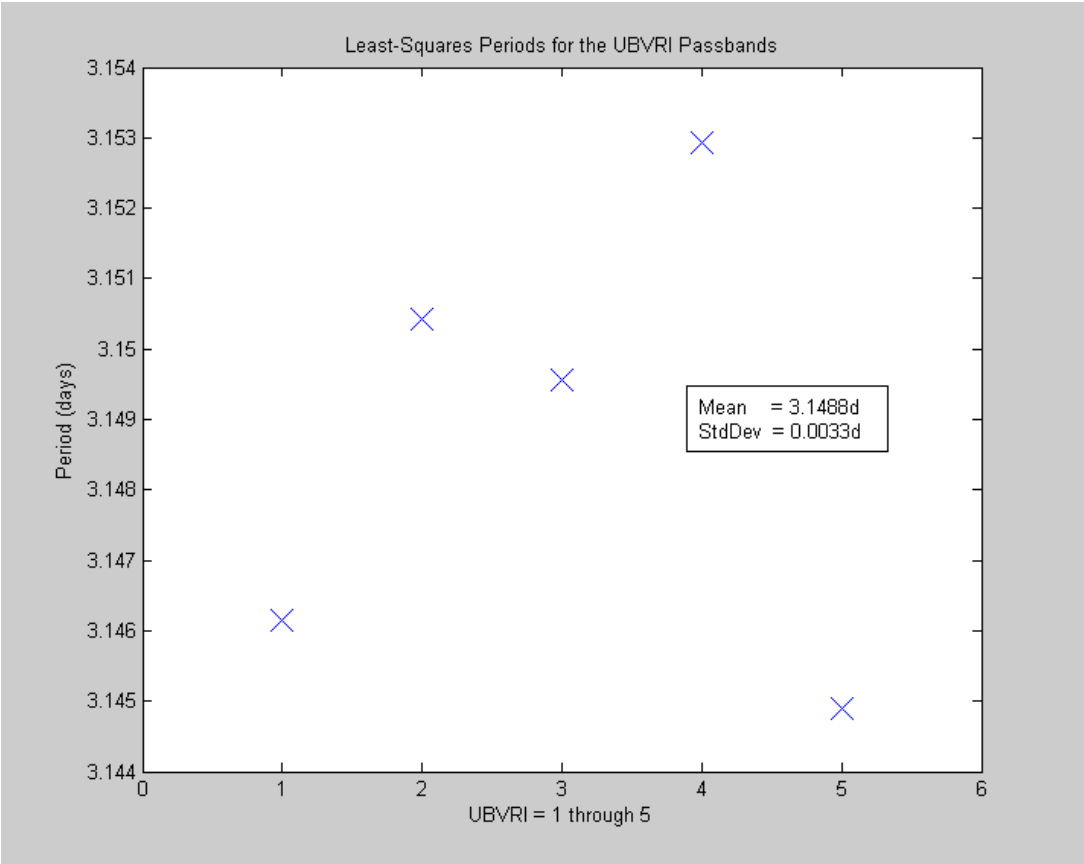

Figure 3-8: Least-squares period for the UBVRI passbands.

Filter	Period (days)	RMS of Fit (mags)
U	3.146145	0.0074
B	3.150372	0.0065
V	3.149550	0.0059
R	3.152765	0.0062
I	3.145097	0.0073
Average	3.1488 ± 0.0033	-

Table 3-4: UBVRI passband periods.[28]

The results of the least-squares-period fitting procedure, performed on all passbands of 5 epochs of variation, shows relatively significant scatter. However, the *average* period (i.e., the period over a large enough number of cycles) for each passband should obviously all be identical, or else a phase discrepancy would build up between the passbands until each varied in brightness in completely nonsensical ways - for example U brightening with B dimming. This would not be expected behaviour for a pulsating star, nor for any other object which varies isotropically and monotonically with temperature. Therefore, the variation of period with passband as seen in Figure 3-8 must originate from scatter which is in some way intrinsic to the data, and so the standard deviation of the periods will be the highest accuracy we can hope to obtain for that quantity from this particular data set. It is clearly possible that the different periods are simply due to basic experimental error introduced by the photometry. But it is not impossible that, on the time scale of one to several pulsations, there can be *real* variations in period between passbands, given that different filters peer to

[28] The period-finding algorithm does not allow errors of determination to be computed for each passband.

different depths in the radiative photosphere. In his definitive work on stellar photospheres, Gray (1992) shows that flux in different filter passbands form at non-commensurate optical depths, such that bluer light generally forms in regions of higher temperature deeper in the photosphere, compared to redder light which forms higher in the photosphere where it is cooler. Because the surface gravity of a Cepheid supergiant star is quite low, the range in optical depth of the formation of the continuum corresponds to a significant range in geometric depth as well. Only loose coupling between the photospheric layers can be expected given that they are relatively rarified and geometrically quite deep. There is at least a possibility, then, of epochal variations in reaction time and behaviour of each passband layer to the driving pulsations coming from the ionization pumping region below. This is an issue clearly worthy of further study both observationally and theoretically, and would be a unique extension to the study of Cepheids for stellar astrophysics.

The mean and standard deviation of the data plotted in Figure 3-8 give the resulting period estimate and its error,

$$P = 3.1488 \pm 0.0033\, d, \tag{3.13}$$

and it is this value that will subsequently be used for the remainder of this study. The error of 0.0033 days on the period estimate is $4^{m}45^{s}$.

It is common practice to phase the light curve data of pulsating stars such that the time of maximum brightness corresponds to zero phase. This requires the determination of an epoch for the light curve and introduces a modification to equation (3.12); it now takes the form

$$\phi = \frac{(HJD - epoch)}{Period} - floor\left(\frac{HJD - epoch}{Period}\right). \tag{3.14}$$

The V passband is chosen for the determination of the epoch. In published literature normally only one epoch is specified and it is usually from the V passband, although we will see in this work that the epoch actually differs for different filter passbands. Most authors do not cite in which passband their epoch was determined. The data are re-phased using the period found above (3.13) and a Fourier fit of appropriate order (in this case, 4) is determined. The minimum of this Fourier fit (i.e. the maximum brightness) and its corresponding phase can be found to an arbitrary degree of accuracy using numerical search techniques, and the subsequent Julian Date is determined through comparison of this phase to that of a phase with a known Julian Date from the data. The epoch is thus determined as

$$epoch = (\phi_{\min} - \phi_0)P + HJD_0 \tag{3.15}$$

where $\phi_{\min}$ is the phase of the Fourier-fit minimum (i.e., maximum magnitude), and ϕ_0 and HJD_0 are a matching phase and heliocentric Julian Date from any point in the real data respectively, and P is the period. The returned value plus or minus multiples of the period can be used as the epoch, but it should be specified within or very near the dates of the observations in order to avoid the error propagated by the period. The result for the V passband near the end of the observation run was thus

$$epoch_V = HJD\ 2,453,316.5166 \pm {}^{0.0023}_{0.0038}. \tag{3.16}$$

The error limits on the epoch were determined by re-phasing the data at the limits of the error on the period, re-fitting new Fourier curves with the new phases, and determining the difference of the new epochs from that of using the mean period.

This procedure was done for the other 4 filters, and their differences from the V epoch are shown in Figure 3-9 and listed in Table 3-5. The differences are well above the error in the determination of the period and the epoch, and varies little upon variation of the fitting routines as described above. This epoch lagging[29] of the passbands is a phenomenon not well discussed in any of the literature. Berdnikov & Pastukhova (1995) report on 11 Cepheids for which they performed O-C analyses, and in table 3 of their work they list "phase correction(s) to the standard light curve in the B band to make it coincident with the standard light curve in the V band...". Out of the more than 120 references in this thesis, their statement appears to be the most any author has had to say on the subject of epoch lagging between passbands. It implies that the data are supposed to be re-phased with the added correction, and that this is even a standard procedure. It would be a rather ad-hoc change to make to the data and is demonstrably an incorrect thing to do on several counts: First, there is the obvious objection of introducing such a change to the data without giving clear justification or reasoning - none is given. Second, following the previous discussion on photospheric passband stratification and that the driving pulsation occurs well below the photosphere, it is quite likely that the different passband layers mechanically react through a *sequence* of times as the pulsation passes through one layer to the next - there is no clear reason to expect that all layers will react simultaneously. And third, aside from any insight into the internal astrophysics of stellar photospheres, there is the very simple fact that the total brightness of a star is the product of its surface brightness *and* surface area. Because the surface brightness variations obviously have different amplitudes in different passbands,

[29] Epoch lagging in the sense used here, and phase lagging, are terms usually used interchangeably. However, it is more accurate to call this phenomenon epoch lagging only, as phase lagging should imply changes in period which then give rise to differences in phase.

whether or not they originate from geometrically different layers, they will combine uniquely with the stellar surface area variation to produce curves which all maximize at unique times. If one considers that the effective surface area of the star may also be unique for each passband given photospheric stratification, the case is made more clearly. SZ Tau's nearly sinusoidal variation in light lends a simple starting point for modeling such pulsations, and this will be discussed in Chapter 5.

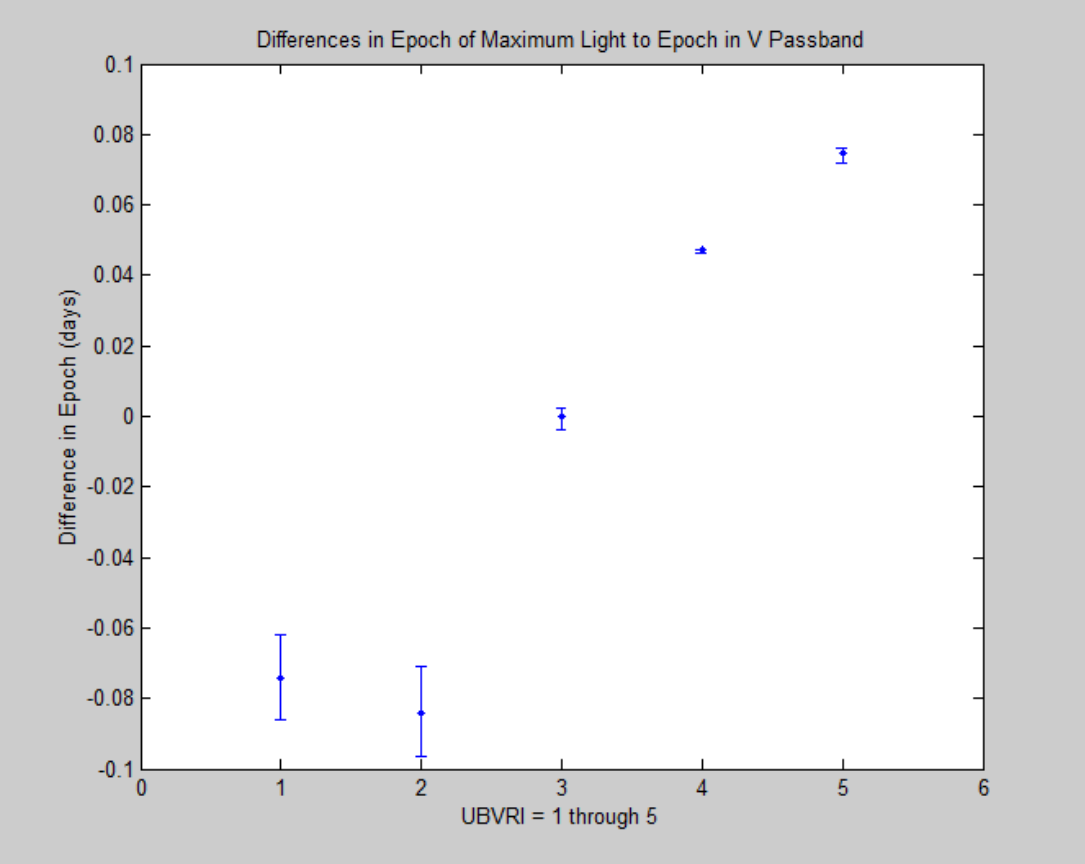

Figure 3-9: UBVRI passband epochs. There is a significant amount of epoch lag between filter passbands.

Passband	Epoch	Difference from V
U	$2{,}453{,}316.4423 \pm {}^{0.0123}_{0.0117}$	-0.0743
B	$2{,}453{,}316.4323 \pm {}^{0.0135}_{0.0123}$	-0.0843
V	$2{,}453{,}316.5166 \pm {}^{0.0023}_{0.0038}$	0
R	$2{,}453{,}316.5637 \pm {}^{0.0000}_{0.0008}$	0.0471
I	$2{,}453{,}316.5912 \mp {}^{0.0028}_{0.0015}$	0.0746

Table 3-5: The UBVRI epochs with all passbands phased to the same period.

3.1.3 Fourier Representations for the Light and Colour Index Curves & Comparison to Published Data

With the period and epoch of the stellar variations determined and a Fourier order selected which best represents the data, we can create Fourier functions for the differential light curves and then use those to create the colour index curves. Fourier functions will also be used for representing the radial velocity data, and these will all subsequently be used in the Baade-Wesselink and Balona analyses. Using such curves greatly simplifies the analysis because data values can then be calculated at any arbitrary and corresponding phase points in the light, colour, and radial velocity data. And it can be reasonably argued that this will produce the same results as if the individual data points were (somehow) used in their original form, because minimization of scattered data points should give the same result as minimization of a curve which is the average of the original data points. The UBVRI differential magnitude curves and their Fourier fits are shown in Figure 3-10.

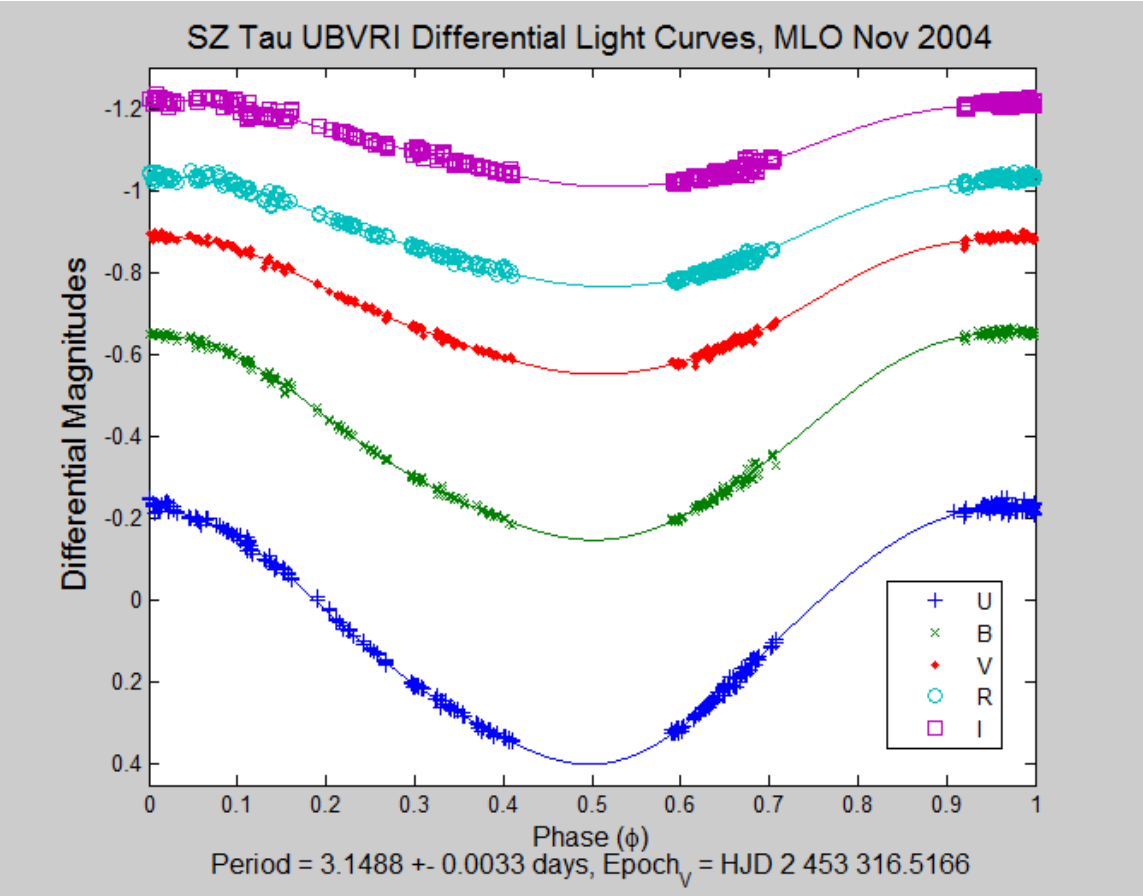

Figure 3-10: SZ Tau UBVRI light curves.

A table of 4th order Fourier coefficients and their ninety-five percent confidence intervals are presented in Table 3-6. The Fourier polynomial takes the form

$$dM(\varphi) = a_0 + a_1\cos(\omega\varphi) + b_1\sin(\omega\varphi) + a_2\cos(2\omega\varphi) + b_2\sin(2\omega\varphi) + a_3\cos(3\omega\varphi) + b_3\sin(3\omega\varphi) + a_4\cos(4\omega\varphi) + b_4\sin(4\omega\varphi) \quad (3.17)$$

where the angular frequency ω is set to exactly 2π because the data has already been phased by the average period, and φ is the phase.

Coefficient	dU	dB	dV	dR	dI
a_0	0.0721 ± 0.0028	-0.4042 ± 0.0025	-0.7231 ± 0.0023	-0.9021 ± 0.0025	-1.1171 ± 0.0030
a_1	-0.3108 ± 0.0024	-0.2545 ± 0.0021	-0.1704 ± 0.0020	-0.1347 ± 0.0020	-0.1051 ± 0.0024
b_1	0.0446 ± 0.0037	0.0266 ± 0.0033	0.0067 ± 0.0031	-0.0006 ± 0.0033	-0.0073 ± 0.0038
a_2	0.0093 ± 0.0023	0.0001 ± 0.0020	-0.0002 ± 0.0019	0.0006 ± 0.0019	0.0011 ± 0.0023
b_2	0.0063 ± 0.0032	0.0098 ± 0.0020	0.0080 ± 0.0019	0.0061 ± 0.0019	0.0063 ± 0.0023
a_3	-0.0032 ± 0.0016	0.0024 ± 0.0028	0.0025 ± 0.0026	0.0011 ± 0.0028	0.0012 ± 0.0032
b_3	-0.0081 ± 0.0007	-0.0051 ± 0.0014	-0.0039 ± 0.0013	-0.0043 ± 0.0014	-0.0024 ± 0.0016
a_4	0.0038 ± 0.0020	0.0042 ± 0.0017	0.0031 ± 0.0016	0.0012 ± 0.0017	0.0014 ± 0.0020
b_4	0.0006 ± 0.0021	-0.0009 ± 0.0018	-0.0028 ± 0.0017	-0.0023 ± 0.0018	-0.0025 ± 0.0021

Table 3-6: Coefficients for the Fourth Order UBVRI Fourier Curves.

Colour index curves can be created through the simple subtraction of these coefficients from one passband to the other. The usual U-B, B-V, V-R and R-I colour indexes are plotted in Figure 3-11. These colour indexes are not fully standardized as they were formed via subtraction of differential light curves, so though they are on the correct magnitude scale they do not have the correct zero point. Again, this is not a problem because both the Balona and Baade-Wesselink methods require knowledge of only the positions (i.e., phases) of equal colour index magnitudes and so differential photometry and colour indices are sufficient.

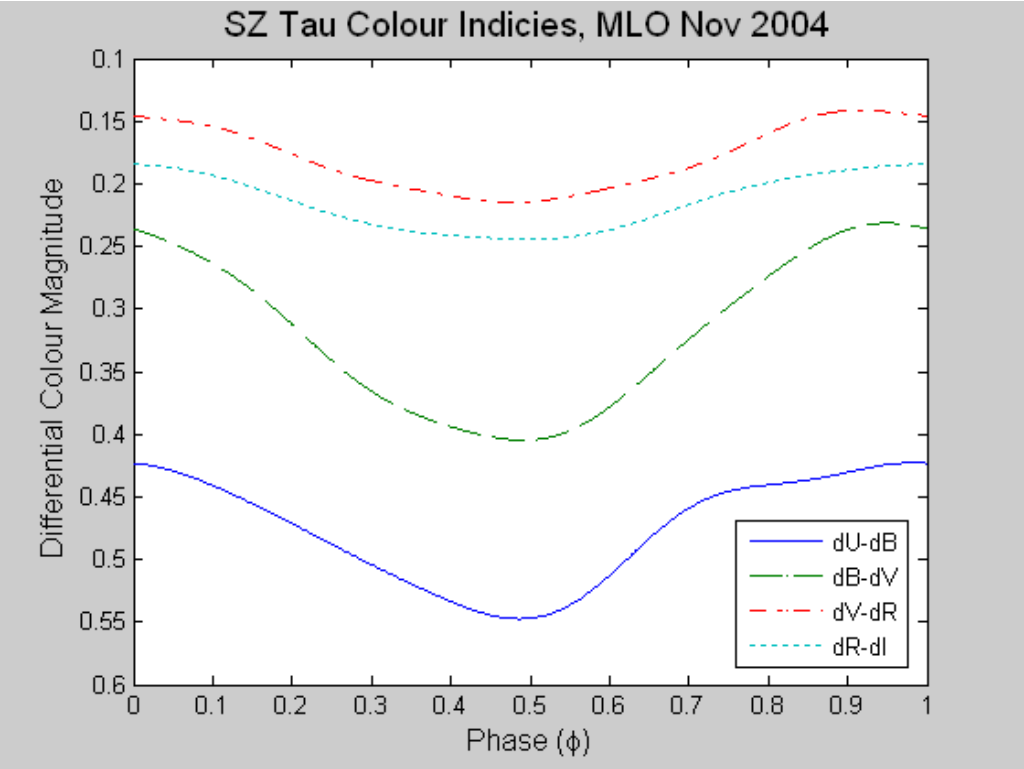

Figure 3-11: Differential colour index curves from subtraction of the Fourier-fitted light curves.

In Figure 3-12 the U-B, V-R, and R-I colour index curves have been scaled to the B-V curve through linear least squares. In comparison to the scatter about the Fourier fits of the original differential magnitude data, the dispersion of the mean colour index curve is quite satisfactory. An obvious correlation is found in that the dispersion in phase regions where the data are dense is the most accurate, while the scaling is more error prone in the phase gaps lacking coverage. Table 3-7 lists the Fourier polynomial coefficients for the mean colour index curve and its dispersion.

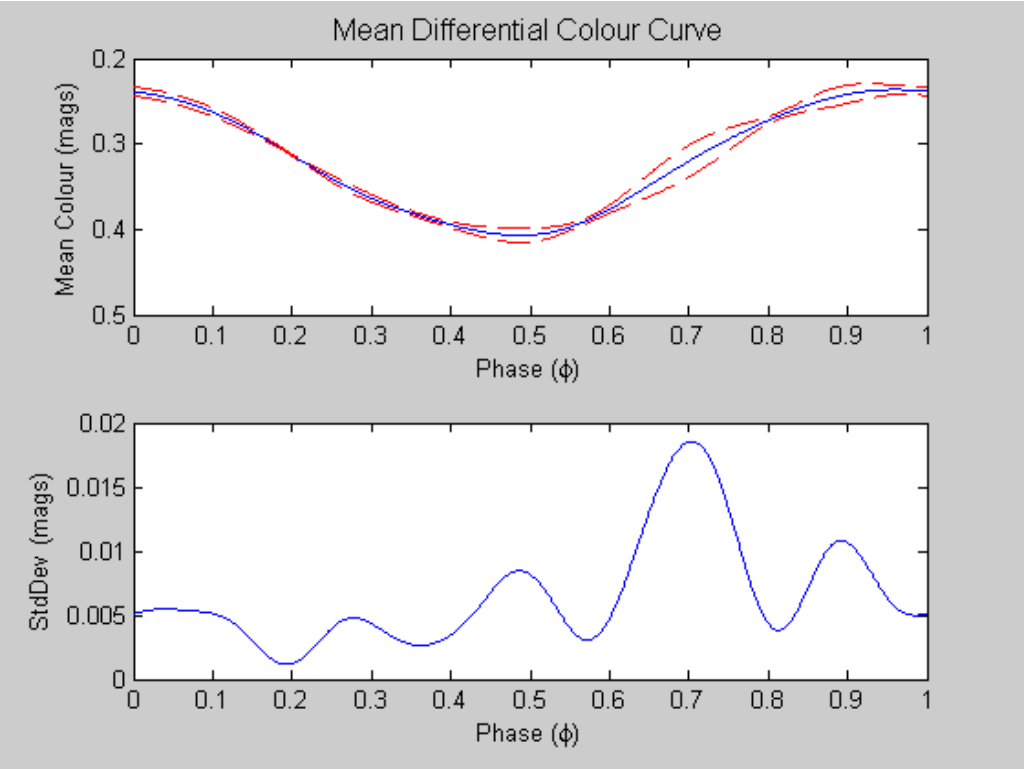

Figure 3-12: Mean colour index curve. The colour index curves scale very well to each other. Regions of poor coverage at 0.5 and 0.8 phase have expectedly larger error.

Coefficient	Mean Colour	Error Curve
a_0	0.3189	0.0066
a_1	-0.0828	-0.0005
b_1	0.0204	-0.0041
a_2	0.0025	-0.0009
b_2	0.0002	0.0006
a_3	-0.0012	0.0015
b_3	-0.0024	0.0010
a_4	0.0011	0.0006
b_4	0.0009	-0.0020
a_5		-0.0028
b_5		0.0007
a_6		-0.0001
b_6		0.0006
a_7		0.0003
b_7		0.0003
a_8		0.0004
b_8		0.0001

Table 3-7: The mean colour index curve for SZ Tauri.[30]

[30] . The mean colour index curve is *exactly* represented by a 4th order Fourier polynomial. The dispersion function requires an 8'th order fit to adequately represent it.

Both Figure 3-11 and Figure 3-12 show that the colour index maximizes before the light. The epoch for the mean colour index is

$$epoch_{MeanColour} = HJD\ 2,453,316.3932 \pm {}^{-0.0056}_{0.0037}, \tag{3.18}$$

0.1234 days or 0.0392 phase before the V passband, which is actually earlier than *any* of the passbands[31]. This connects to the previous discussions on passband epoch lagging in a very relevant way. That the passbands have generally the same profile in their variation in light but lag each other by some small amount, it automatically requires that the colour index between them will maximize at a different time than either of them, either before or after depending on the direction of the subtraction. If generally B-V is reflective of effective temperature and through it the effective surface brightness, one must indeed expect the colour index to maximize at a time earlier than the light *because* the surface area maximizes *after* the light. Epoch lagging is then an expected and fundamental prerequisite, but see Chapter 5 for a complete discussion.

Moffett & Barnes (1980) have good standardized Johnson BVRI data of SZ Tau taken between April 1977 and December 1979. The two corresponding passbands to the MLO data (i.e. B & V) show an extremely good match, aside from linear offsets to shift the differential MLO data to the standard system. The comparisons are shown in the next three figures below. Barnes et. al. (1997) have further BVRIJHK photometry of SZ Tau from later epochs, but these data turn out to suffer from an error in the determination of the epoch, so that the data are shifted by approximately 0.1 phase. This is due to a large gap in

---

[31] The error on the epoch of the mean colour index was determined by re-phasing all data to the limits of the error in the period (epoched using the corresponding V epoch), forming new mean colour index curves at those limits, and then finding the minimum of the curves. In both cases, the epoch of the mean colour index moves slightly earlier in phase.

their photometry of 0.2 phase in width at the maximum of the light curves, which led to a poor determination of the time of maximum light - the problem is not noticed in their paper however. When shifted in phase it matches with what is shown below.

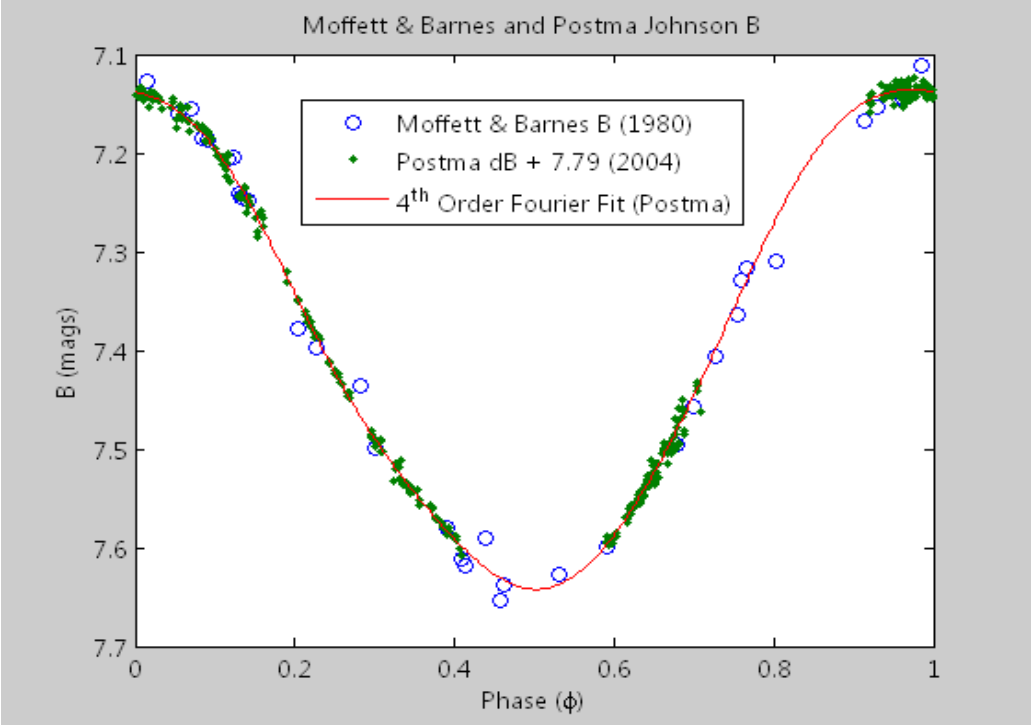

Figure 3-13: Moffett & Barnes vs. Postma Johnson B light curve.

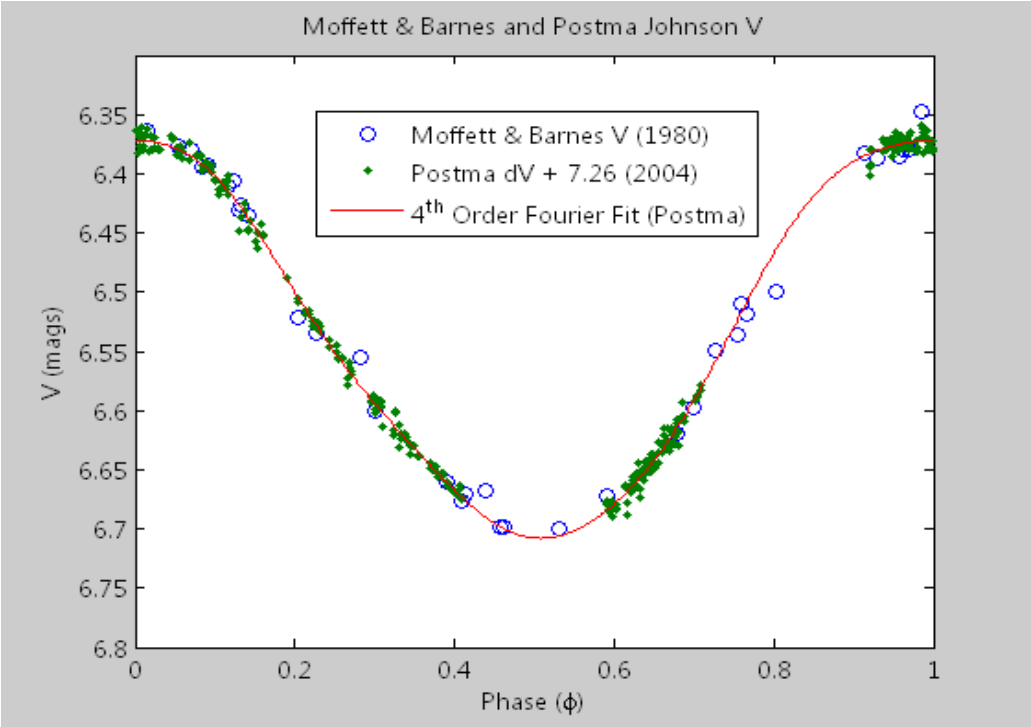

Figure 3-14: Moffett & Barnes vs. Postma Johnson V light curve.

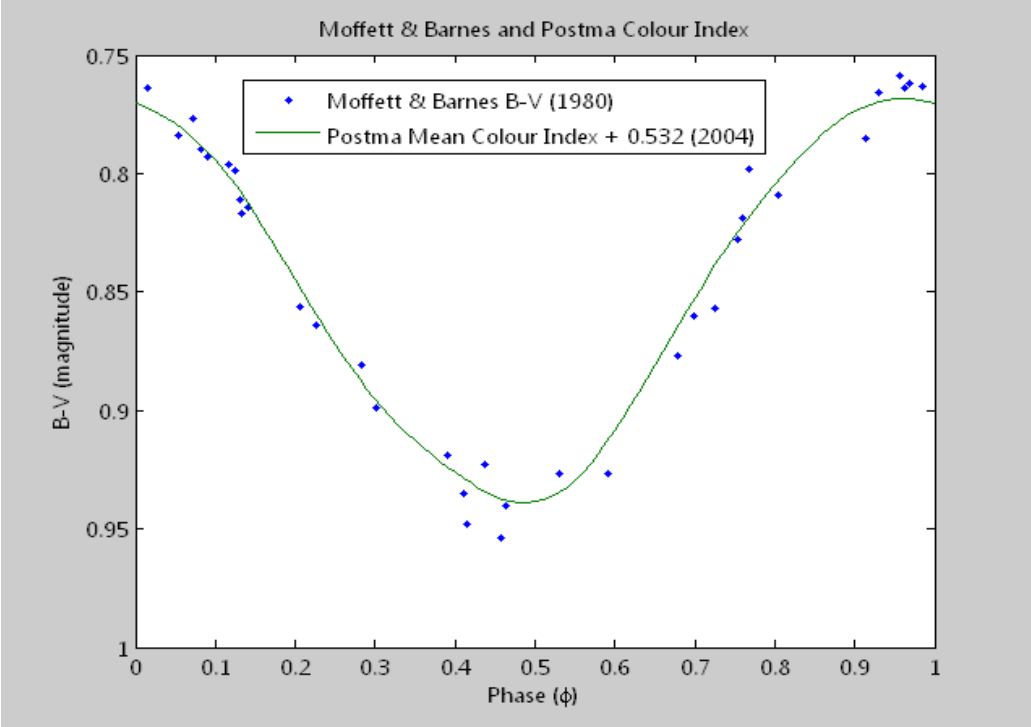

Figure 3-15: Moffett & Barnes vs. Postma Johnson B-V light curve. The colour excess has not been applied.

Gray (1992) gives a polynomial to convert from B-V magnitude to effective temperature

$$\log(T_{eff}) = 3.988 - 0.881(B-V)_0 + 2.142((B-V)_0)^2 - 3.614((B-V)_0)^3 + 3.2637((B-V)_0)^4 - 1.4727((B-V)_0)^5 + 0.26((B-V)_0)^6 \quad (3.19)$$

Applying Turner's (1992) careful determination of $E_{B-V} = 0.29$ for the colour excess, equation (3.19) results in the temperature curve in Figure 3-16 below, and gives a mean effective temperature of 6021 K. SZ Tau's average luminosity[32] of $\log \frac{L}{L_{Sun}} = 3.33$ classifies it as a class Ib supergiant, and so its spectral type varies between about F6 at the hottest to F9 at the coolest, averaging F7.5. Sanewal & Rautela (1989) report a temperature variation which is offset several hundred degrees higher than that reported here, based on comparison of their data to the model atmospheres given by Kurucz (1979). However, they used a colour excess of $E_{B-V} = 0.31$ and so this accounts for most of the difference.

[32] Calculated using the average Balona radius determined later in this work, and the mean of the temperature curve in Figure 3-16. $L = 4\pi\sigma T^4 R^2$.

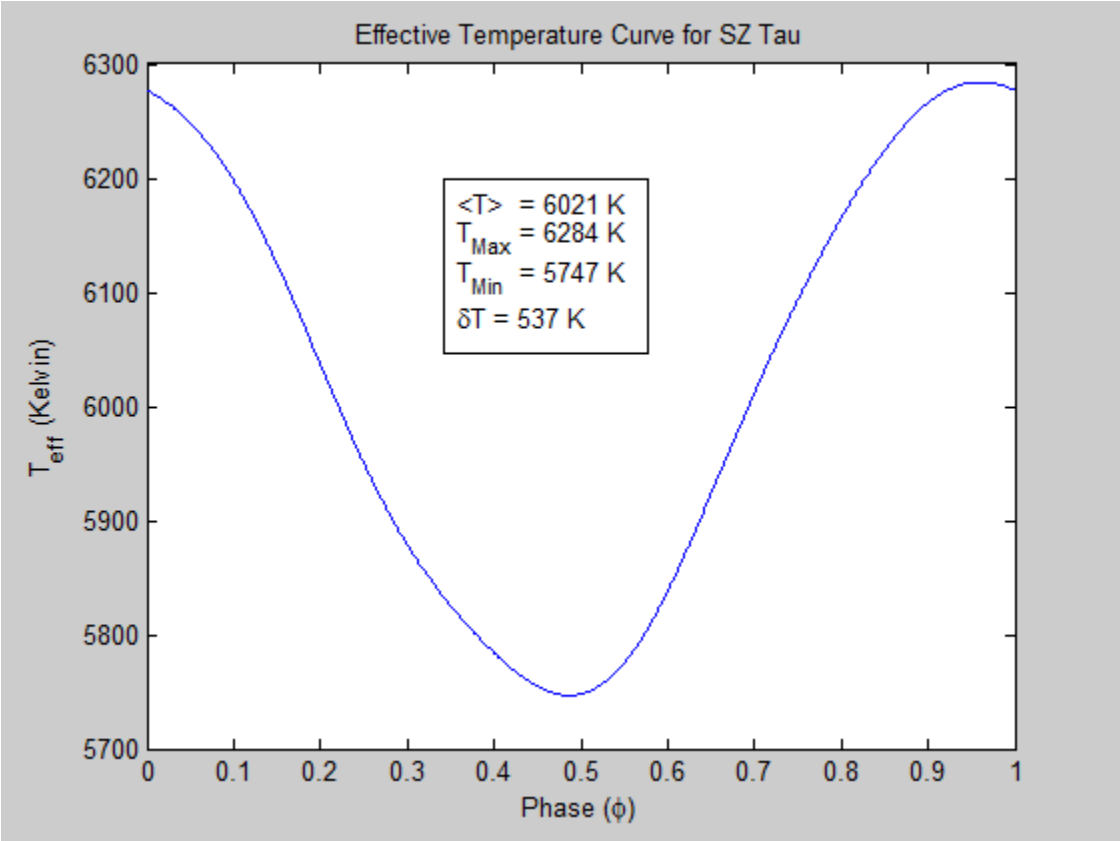

Figure 3-16: Effective temperature curve for SZ Tau.

3.2 Spectroscopic Reduction and Radial Velocities

3.2.1 Spectra from the Dominion Astrophysical Observatory

Moderate resolution spectroscopy was obtained for SZ Tauri during a two-week observing run at the DAO[33] from October 02 through October 15, 2003. The Plaskett[34] 72" (1.85m) f/18 Cassegrain mounted spectrograph was used with a SITe-2[35] CCD detector. The SITe-2 is a thinned, UV coated 532x1752 15 micron pixel CCD chip. It has a readout noise of approximately 12 e^-/pixel, a gain of 1 e^-/ADU[36], and a quantum efficiency (QE) of 35% at 4000Å. The spectrograph was used in configuration 21121B, referring to use of the 21" focal length camera and a 1200 L/mm grating used in the first order with a peak blaze efficiency on the blue side of the visible spectrum. The reciprocal linear dispersion is nominally 15 Å/mm. No image slicer was used at the spectrograph entrance slit, which was set to 9 thousands of an inch or 1.4 arc-seconds on the sky.

Only ten data points were obtained for this star during the observing run because inclement weather ruined many nights of observation. The data were distributed at only three points in phase occurring at φ = 0.2, 0.65 and 0.85. Therefore, for the purposes of this study, archival radial velocity data have been used. The reduction procedures for the spectra

---

[33] Dominion Astrophysical Observatory, Victoria, B.C.
[34] Named after John S. Plaskett, founder of the Victoria location DAO, 1913.
[35] SITe is a CCD manufacturing company, a descendent company from Tektronix
[36] ADU: analogue to digital unit

and the extraction of the radial velocities will still be discussed presently, however. The ten points that were obtained fit well with the older published data (see Chapter 3.2.3). A graphical user interface (GUI) software program written by the author called CCDRED[37] was used to reduce the CCD data; it can reduce both spectroscopic and photometric image data.

The first step in reducing a CCD image is to create a master "bias" frame[38] for subtraction from all images. A bias is a zero second[39] exposure for calibrating the chip's electrical charge offset which the CCD acquires as it initializes for an exposure. The offset presents a zero-point background, typically $1/60^{th}$ the dynamic range of the chip, and which must be subtracted from each real data frame. In high quality and especially modern CCDs the bias is usually quite uniform across the field, and in this case one can use the global mean or median value of the entire bias matrix for subtraction from the image data frames. This should increase the signal to noise ratio (SNR) in the final image because it avoids introducing the read noise from the bias image into the reduced one - subtracting the entire bias frame from the image frame would increase the noise level in the reduced image through quadrature addition of the read noises from the two frames. If the temperature is stable, and failing any hardware troubles, the global median of the bias will remain constant.

Older CCD chips usually suffer from broad scale non-uniformity in the bias structure. This necessitates the collection of around a dozen, or even several dozens, of bias frames every night of observation. The bias level and its structure are quite sensitive to

---

[37] See footnote 23.
[38] The terms "frame", "image", "matrix" and "data" are used interchangeably.
[39] Commonly, CCD control software allows one to enter zero as an exposure time, but the hardware actually uses the fastest "blink" time that it can, which is of order 10ms. The shutter is closed for the exposure.

temperature variations, so that even through the course of a night of observations the bias level can vary significantly if the CCD chip is not properly cooled and insulated. In some cases, taking samples of bias throughout the night is warranted, depending on the nightly temperature fluctuations and the cooling method of the CCD hardware. Standard thermoelectric Peltier coolers cool only relative to the ambient temperature of the surrounding air, and they do not cool efficiently much further than 35 Celsius below ambient. At this relatively high temperature the bias (and the dark current…see following) is extremely sensitive to thermal variations. Cryogenic cooling with liquid nitrogen (LN_2) is far superior, if the telescope and its corresponding hardware configuration allow it. LN_2 will hold the chip at a constant temperature independent of external thermal variations, and this temperature is so low that the bias level can be kept fully constant (and the dark current close to zero). Nitrogen exists naturally in its liquid state near -180^0 C, so usually a small heating element is placed against or near the CCD chip to raise it to a temperature of around -125^0 C, in order to ensure optimal quantum efficiency of the photoelectric material.

Figure 3-17 below shows the bias structure of the SITe-2 CCD from the DAO. The uniform strip on the right side of the image is the overscan area, which does not represent any real portion of the CCD chip. It is the result of the analogue to digital unit converter (ADC) reading off imaginary pixels at dimensions larger than the actual chip, and it can be used for comparison to the bias level of the CCD[40]. In high quality CCD's the difference between the overscan area and the bias will be zero, indicating proper functioning and low noise of the chip. In addition to the obvious difference of the bias level from the overscan

[40] Not all CCD chip hardware is capable of this functionality.

as seen in Figure 3-17, there is also a broad scale variation in intensity across the field. The pixel-to-pixel granulation is the random noise from the readout of the chip (i.e., the read noise), and was found to have a value of about 5 counts or 0.2% of the mean. The larger scale, left-to-right gradient variation is about 15 counts or 0.6%. The image is expanded in the vertical direction, and also note that the vertical direction has only 140 pixel rows; this is due to on-chip binning of the pixel columns by a factor of 4.

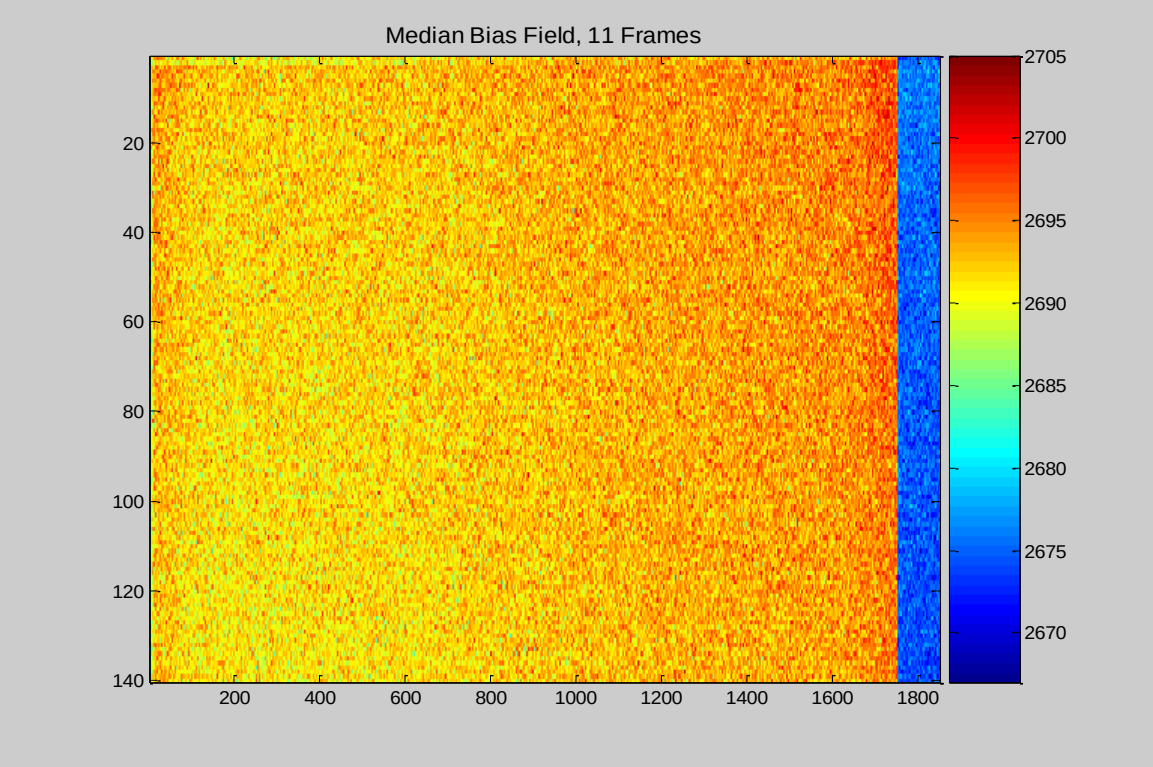

Figure 3-17: A significant large scale variation is seen in this bias.

Because the large scale variation is constant in time (at constant temperature), one can improve the signal to noise ratio in the reduced image by using a smoothed 2 dimensional fit to the bias surface for subtraction from real image data. Subtraction of the raw median bias from an image will incorporate that bias' random read noise into the frame,

because the image data already contain their own random read noise and so the two noise contributions would add in the usual way. Subtraction of a smooth surface function is the equivalent of using the global median from a structure-less bias, and so introduces no additional read noise into the reduced image. If the bias structure proves too unwieldy for fitting, the raw bias frame must be used admitting a small loss in the signal to noise ratio.

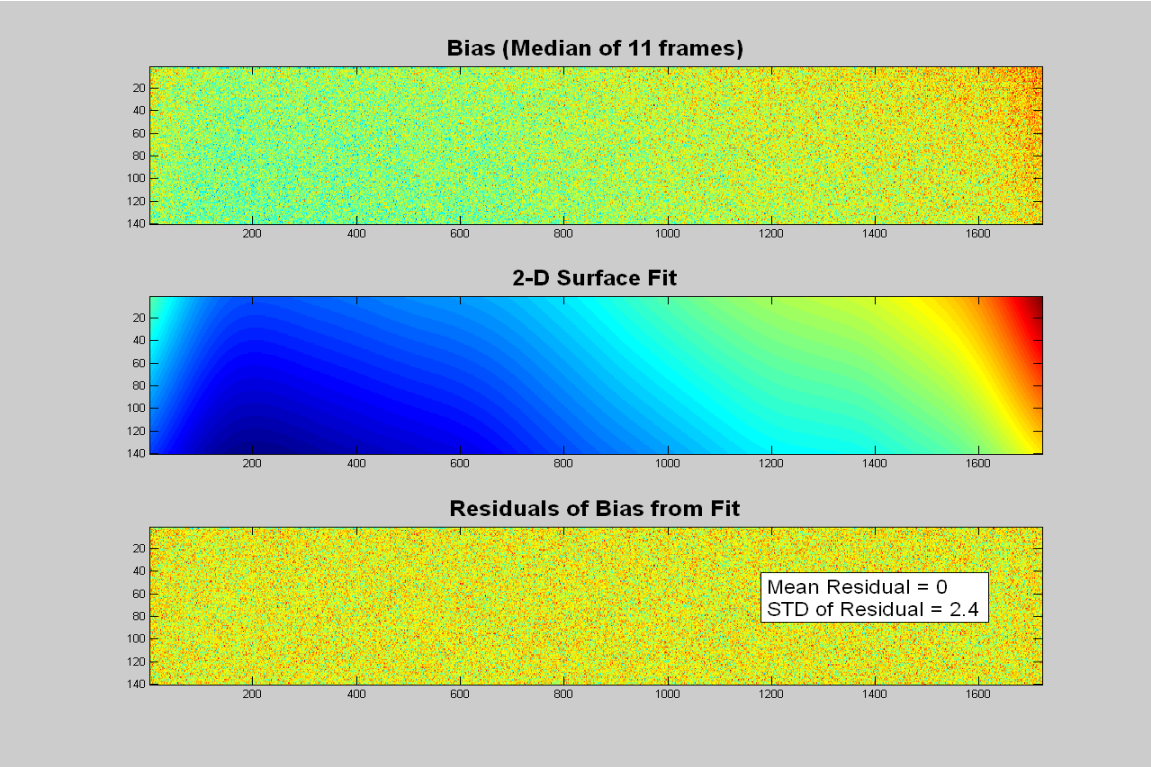

Figure 3-18: A two-dimensional surface fit can be used to model the large scale bias variation when such a variation is smooth and continuous. The overscan has been clipped from the data matrix.

Figure 3-18 shows a two-dimensional surface fit and its residuals to the median bias frame from the DAO. The residuals plot in the bottom frame show a purely uniform, random variation. The standard deviation of the residuals of 2.4 counts would be the level

of random noise introduced into each pixel of the data frame if the median bias was subtracted instead of the surface fit.

Another background offset which must be subtracted from the data is the "dark current", sometimes called "thermal" frames, indicative of their sensitivity to temperature. At most temperatures the photoconductive material of the CCD will spontaneously emit thermal electrons into the CCD pixels, and this presents a further zero-point offset in the background. Cryogenic cooling can keep the rate of thermal emission down to a mere one or two counts per hour of continuous exposure. Thermoelectric Peltier cooling, which is much warmer than LN_2, can see dark currents of one hundred counts per minute or more. Because the cooling was of the former type at the DAO, dark frames were not taken during this observing run. However, the reduction procedure for the dark frames follows essentially that of the bias frames. Each set (of say 11 images) of dark frames must be taken with the shutter for the CCD camera closed and for the same exposure time(s) as the image data, and most importantly also at the same temperature. It is theoretically possible to take only one set of dark images at a long exposure time, and then simply scale the dark data by the ratio of image exposure time to dark exposure time. However, the author has observed that the thermal level does not always scale linearly with exposure time, and recommends to take sets of dark frames at each exposure time of the data images. If the bias and darks are being processed separately (see discussion in next paragraph), then the bias must be subtracted from the dark before the dark is subtracted from the image because each data frame, no matter its purpose or how it was taken, contains the bias.

It is a matter of contention whether or not it is necessary to perform the bias subtraction distinctly from the dark and image data at all, because a dark image is simply

$D_{image}(x,y) = D_{current}(x,y) + B(x,y)$, where $B(x,y)$ is the bias. Because the bias level and its variations exist in every single frame and so are already represented within the dark and science-image data, it should be sufficient to subtract the dark frame only from the science-image. This would avoid multiple introductions of the read noise into the processed data. If the dark frames can also be modeled with a smooth surface fit, then the only random read noise in the reduced data will be that already inherent to the science-image.

The full subtractive offset corrections to an image $I(x,y)$ are thus

$$I_{offset\ corrected}(x,y) = (I_{raw}(x,y) - B(x,y)) - (D_{image}(x,y) - B(x,y)). \tag{3.20}$$

Quadrature addition of noise is then

$$\delta I^2{}_{offset\ corrected}(x,y) = \delta I^2{}_{raw}(x,y) + 2\delta B^2(x,y) + \delta D^2{}_{image}(x,y). \tag{3.21}$$

However, equation (3.20) quite simply reduces to

$$I_{offset\ corrected}(x,y) = I_{raw}(x,y) - D_{image}(x,y) \tag{3.22}$$

and the noise is then

$$\delta I^2{}_{offset\ corrected}(x,y) = \delta I^2{}_{raw}(x,y) + \delta D^2{}_{image}(x,y) \tag{3.23}$$

but only if the bias has *not* been subtracted separately from the raw dark and raw image data. If the dark frame has been modeled with a smooth function, then its contribution in (3.23) is zero. If no dark frames were taken because LN_2 cooling was used and exposure times short, the bias must then still be subtracted. For our session at the DAO, we assumed that the dark current was negligible and so used the bias only for background offset correction[41].

---

[41] The author admits this is a very convenient assumption: batches of bias frames are much faster to record, and this affects mental reasoning at 6 o'clock in the morning.

The final correction which must be applied to the data images involves what is called a "flat field". It is an image which records the sensitivity modulations of the optical train of the telescope and detector. The need for this is two-fold: first, every individual pixel on the CCD chip does not have the exact same quantum efficiency (QE) as the others; second, dust and "smudges" on the telescopic optics can modulate the intensity of light falling across the CCD imaging field. The latter problem is significant mainly for photometric imaging; in spectroscopy, any information regarding telescopic dust and smudging on the optics is integrated at the focus of the spectrograph entrance slit, and this makes the formation of the flat field image much more simple. One merely shines a polychromatic source from a properly selected, spectrum-less incandescent light bulb onto the entrance slit and then images the continuous spectrum. Flat fielding in photometry is usually more complex, requiring imaging of the twilight sky or the imaging of a large white screen attached to the inside of the telescope dome, evenly illuminated with a polychromatic light source. These are usually called "sky flats", and "dome flats", respectively. In both cases a major difficulty is found in attaining a truly uniform illumination across the imaging field. Twilight sky can have gradients across the image with distance from the sun, moon, or horizon, while dome flats are simply difficult to uniformly illuminate. In all cases, flat field images should be exposed to approximately 50% of the dynamic range of the sensor in order to ensure a high signal to noise ratio without approaching the saturation level of the CCD chip.

The flat field correction is not by subtraction, but by division. Given a uniform source the field sensitivity modulations will produce different count rates in different areas of the chip, even though all the rates should have been equal. The read noise in a flat field is negligible compared to its signal, so that the pixel-to-pixel variations are actually due to the

quantum efficiency variations of the pixels; these must be corrected from the image and therefore a smooth function should not be fit through the flat field.

Let the image source function, i.e. the function that describes the spatial field distribution of the light just before it enters the telescope[42], be defined as *S(x,y)*. Let the detector response function which modulates the light according to the sensitivity variations inherent to the optical train and detector be *R(x,y)*. An image *I(x,y)* can then be expressed[43] as

$$I(x,y) = S(x,y) \cdot R(x,y) \tag{3.24}$$

In practice we record *I(x,y)* but we want *S(x,y)*, so we must therefore divide out *R(x,y)*.

A flat field image can then be expressed via the above equations as

$$F(x,y) = f(x,y) \cdot R(x,y),$$

where *f(x,y)* is the flat field illumination source. However, *f(x,y)* is a *uniform* illumination source so that $f(x,y) = f_0$, and thus the flat field image is

$$F(x,y) = f_0 \cdot R(x,y). \tag{3.25}$$

If equation (3.25) is normalized[44] by dividing by its mean (or possibly median) value we have

$$F_n(x,y) = \frac{R(x,y)}{\sum_{\forall(x,y)} R(x,y)/N}, \tag{3.26}$$

where *N* is the number of pixel elements. Dividing (3.24) by (3.26) then leaves

---

[42] This would be the case for photometry. For spectroscopy, it is the distribution in light just after leaving the grating.

[43] Assuming the background offsets have already been applied.

[44] "Normalizing" means to force a value or average of values to be equal to 1.

$$\frac{I(x,y)}{F_n(x,y)} = \frac{S(x,y)\cdot R(x,y)}{R(x,y)/\left(\sum_{\forall(x,y)} R(x,y)/N\right)}. \tag{3.27}$$

Because *R(x,y)* appears in both the numerator and denominator on the right side of (3.27) its modulating effects are cancelled out, leaving only the original source *S(x,y)*. And because the denominator as a whole has been normalized, the total flux on the right hand side is preserved. The uniformity of the flat field $f(x,y) = f_0$ is clearly paramount in order to be able to properly correct for the sensitivity variations of *R(x,y)* across the field of the CCD chip. In practice, the flat field image is reduced by offset correcting through equation (3.20) or (3.22) and then dividing by its mean (or median) as in (3.26)

Figure 3-19 shows a median flat field from a batch of 11 images from the DAO. The granulation in the plots are due to the random variations of pixel-to-pixel quantum efficiencies. The dispersion axis of the spectrograph is in the horizontal direction of the image. Because CCD quantum efficiency varies with wavelength the broad horizontal variation in the flat field is expected, particularly because such a large range in wavelength (400Å) was imaged. The vertical variation was not expected, but could be due to improper alignment or illumination of the spectrograph entrance slit by the flat field source. The vertical artifact visible at the last quarter of the top image is due to an unresponsive or 'dead' pixel column.

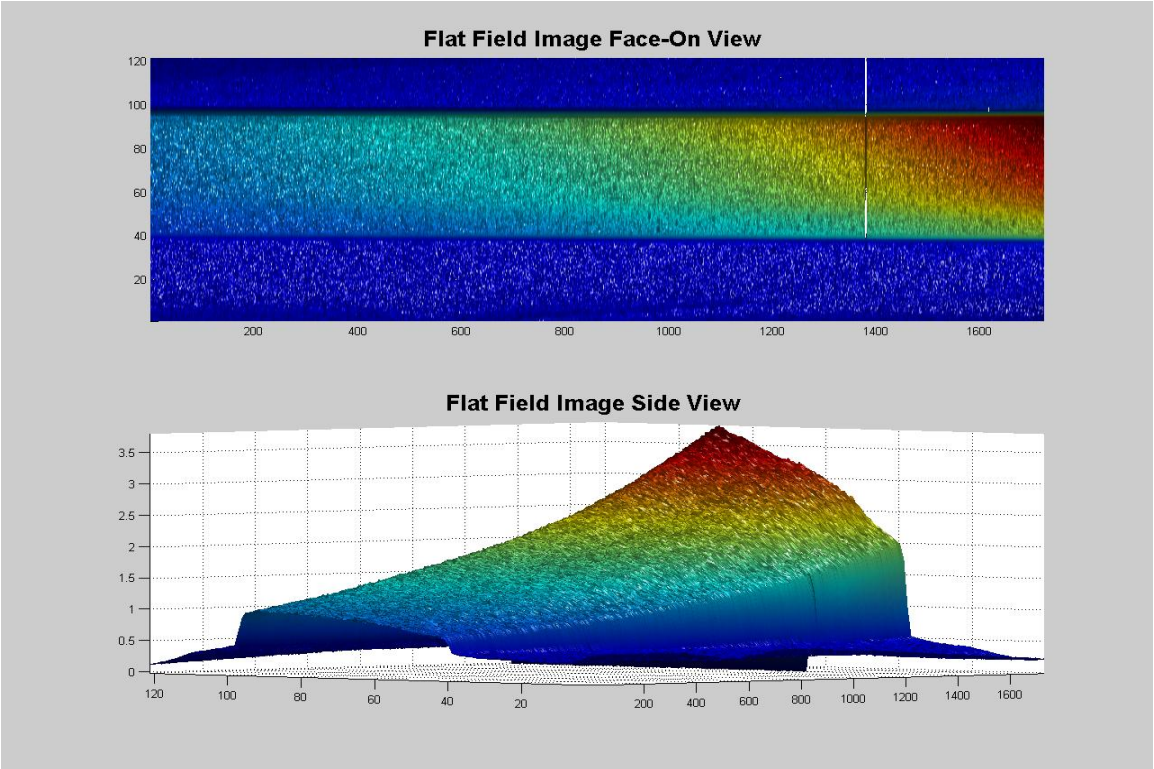

Figure 3-19: Median of eleven flat field images. The field has been normalized.

We can now fully express a raw image as

$$I(x,y) = S(x,y) \cdot R(x,y) + D(x,y) + B(x,y), \tag{3.28}$$

where *S(x,y)* is a real image from the sky[45] and *R(x,y)* is as above, *D(x,y)* is the dark current and *B(x,y)* the bias offset. Solving simply for the science data *S(x,y)* one has for the reduced data

$$S(x,y) = \frac{I(x,y) - D(x,y) - B(x,y)}{R(x,y)}. \tag{3.29}$$

The numerator is offset-corrected according to the principles discussed before equation (3.20) and the denominator is the offset-corrected normalized flat field from equation (3.26).

[45] Or grating.

Figure 3-20 shows an image of the raw spectrum of SZ Tau. The image has been clipped to the same dimensions as that of the surface fitted bias and the flat frame, and those corrections have been applied to it in kind. Note that the region of the chip where the spectrum falls is in a very narrow horizontal band; this is the star light dispersed from the grating and its height is due to the seeing disk of the star projected through the spectrograph optics and onto the chip. The speckles are due to cosmic ray events and spurious hot pixels.

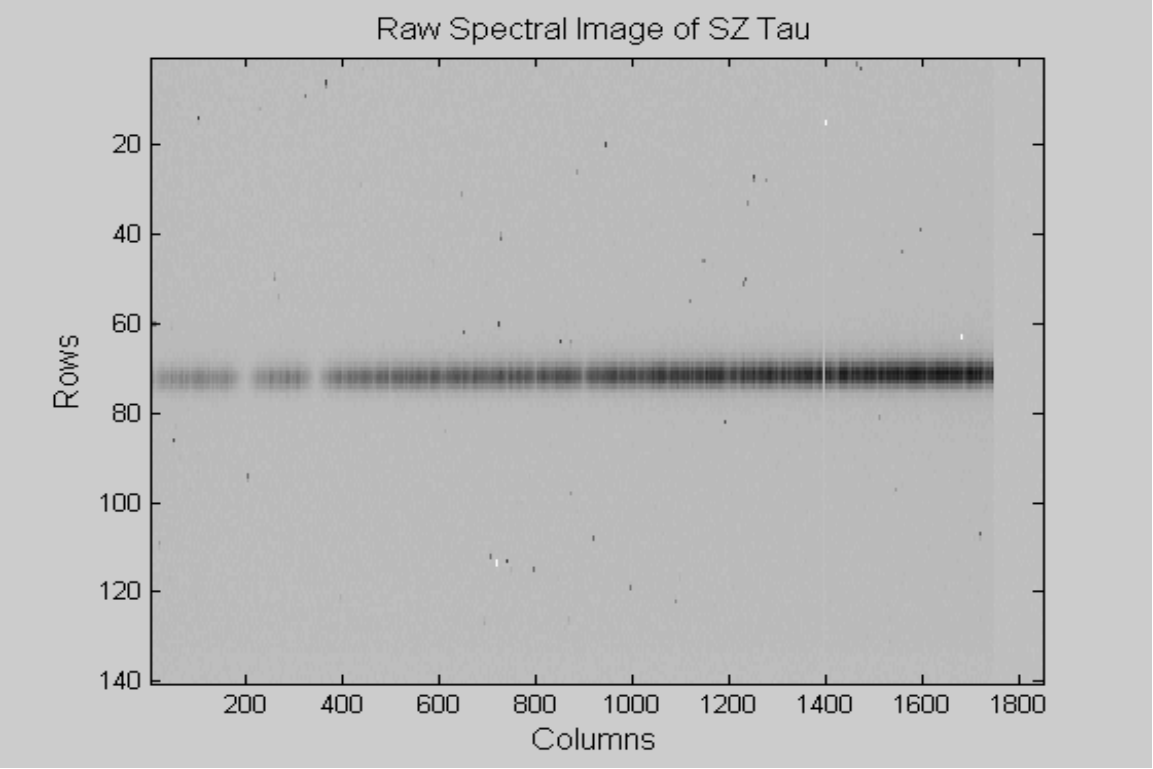

Figure 3-20: Pre-reduced CCD image of the spectrum of SZ Tau.

Obviously, the regions in the image above and below the spectrum where no useable data are found must be clipped from the data matrix. In spectroscopy mode CCDRED accomplishes this by overlay-plotting all of the pixel columns from the image onto the same axis, as seen in Figure 3-21. The user then identifies the relevant portion of the data with the

mouse. An alternative automated routine could be developed which identifies all data rows[46] above a user defined SNR, but this simple method has not yet been implemented.

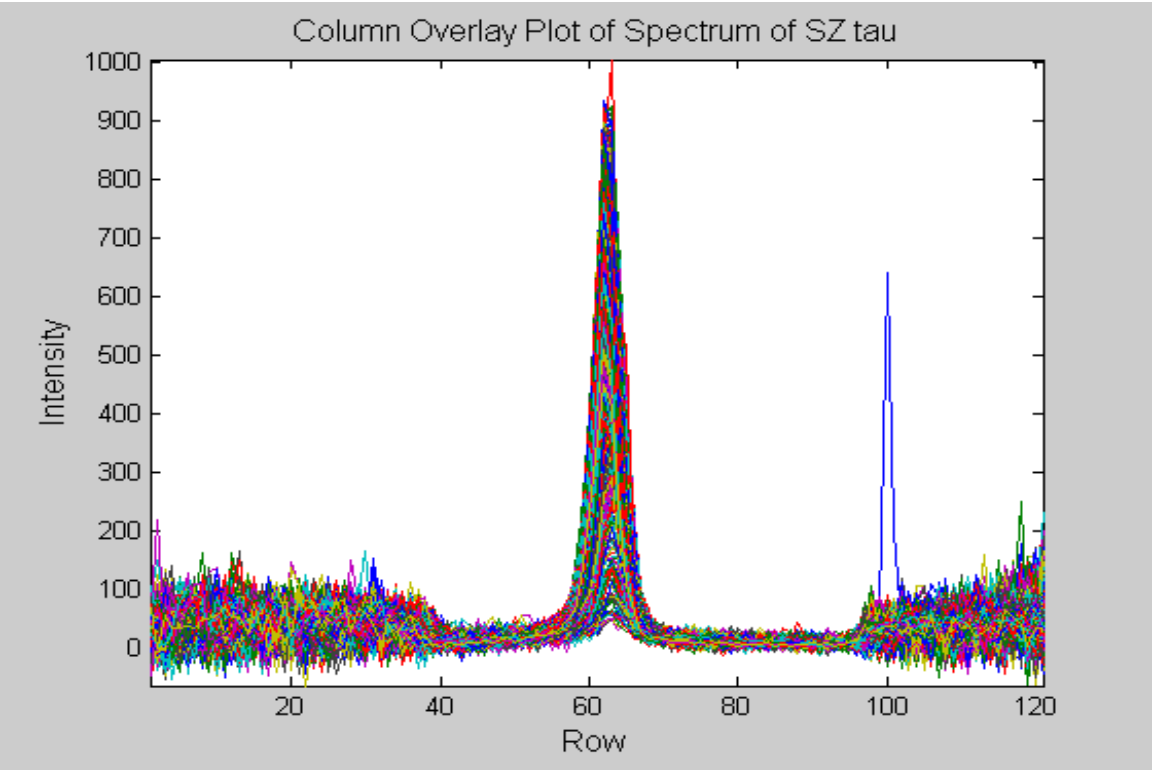

Figure 3-21: The pixel columns from Figure 3-20 are plotted one over the other in this column overlay plot. The spike at row 100 is due to a hot pixel or cosmic ray event, and is extraneous to the spectral data. The "fuzzy" wings are due to the low SNR of the flat field in that area.

If the data regions with no signal are relatively uniform in both intensity and noise level (which would be difficult to argue for Figure 3-21), the average level could perhaps be employed as a background estimate for the combined effects of sky and internally scattered light in the spectrograph, and that value could be subtracted from the data as well. This would be important when precisely measuring spectral line depths or integrated absorption.

---

[46] "Rows" in the sense of Figure 3-20.

In Figure 3-22 the extraneous data regions have been clipped from the image, leaving only the spectrum. The spectral data lying in the rows at the extremities of the pixel row plot (top panel) correspond to the spectral profiles of low intensity in the pixel column plot (bottom panel), and vice-versa. One ultimately wishes to reduce the two dimensional image into a one-dimensional spectrum, so the eight rows of spectral data which are left after clipping should be averaged together to form the single line spectrum. However, it is clear that each row of data has a different average signal to noise ratio. Therefore, if each spectral row is weighted by its average SNR, their weighted mean will give an optimized result for the single line spectral profile.

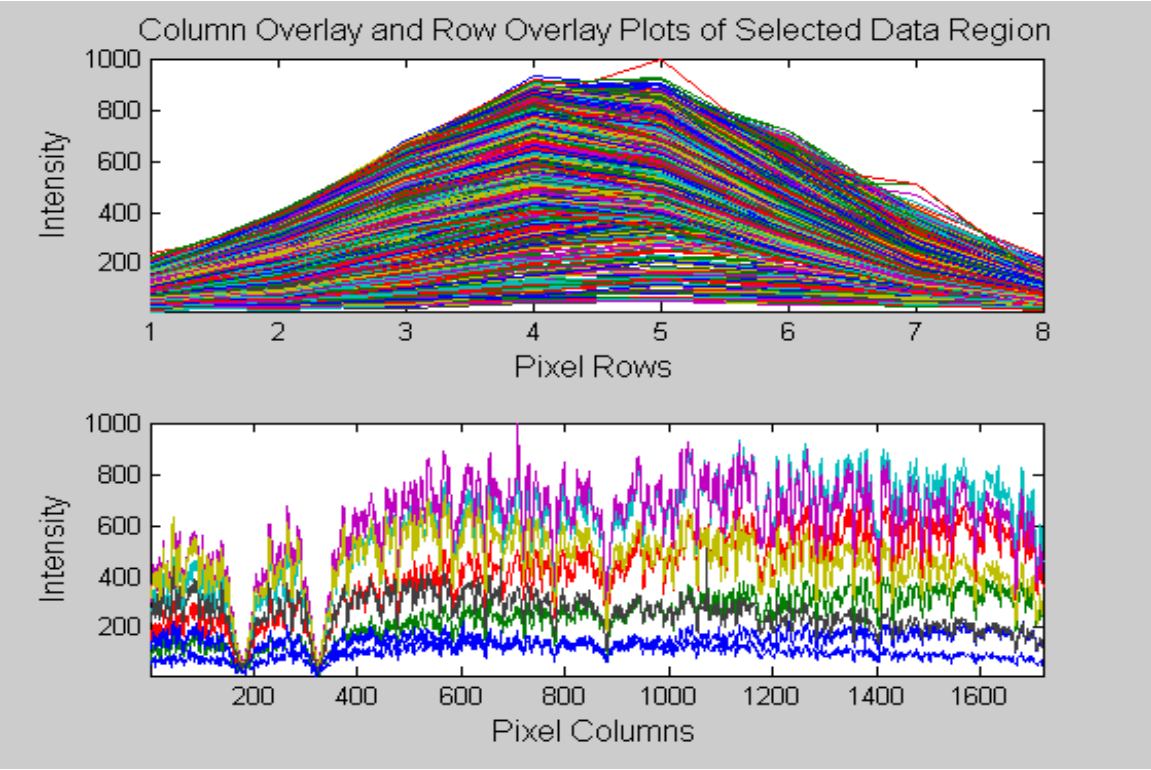

Figure 3-22: Eight rows of data are left after clipping the extraneous portions from the plot in Figure 3-21.

Looking closely at the bottom panel in Figure 3-22 it is apparent that not every row of spectral data mimics the other's large scale variations, i.e., those variations occurring over a much larger scale than the average scale of variation due to spectral absorption features. The cause of these variations are most likely due to the un-evenly illuminated flat field image as noted above. Because in general it is not known which spectral row will best reflect the actual large scale variation due to the stellar flux profile, it can be assumed that the one with the highest average SNR does. Low order polynomials can then be fitted through each spectral row, and their ratios to the fit through the highest SNR row can be used to de-skew the coarse variations. After each row is de-skewed and weighted the average spectral profile is computed, and this is shown in Figure 3-23.

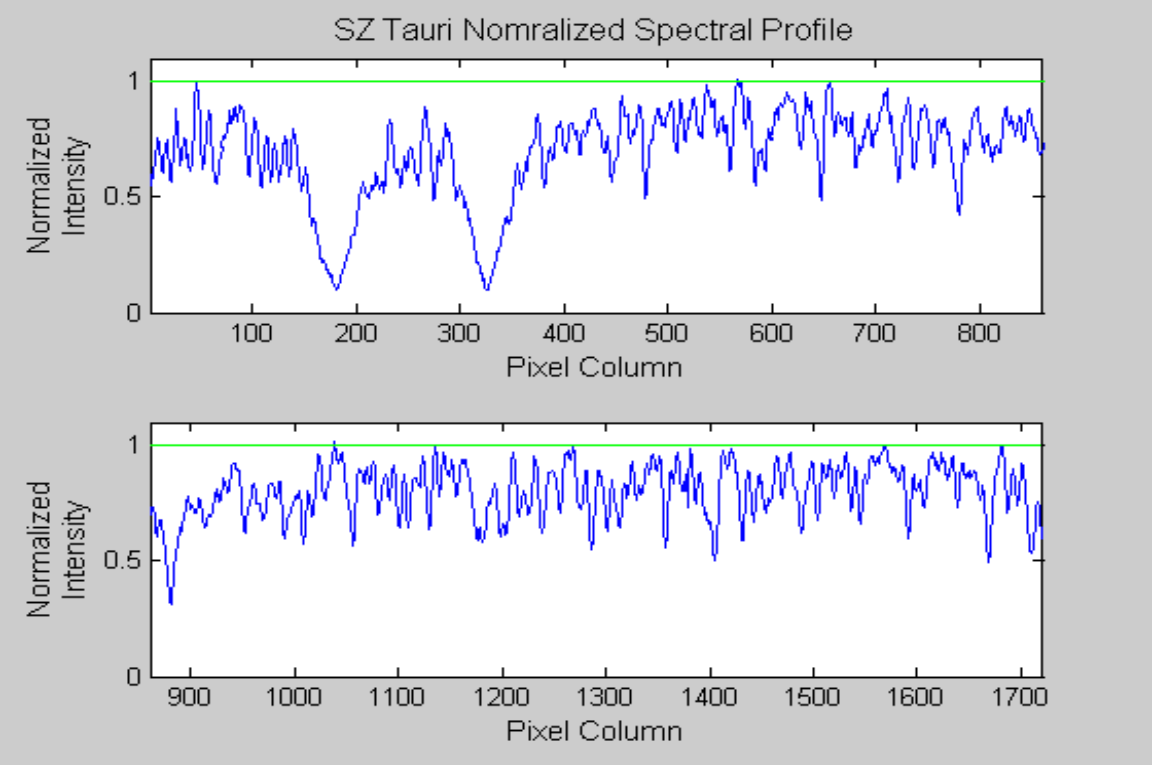

Figure 3-23: Fully reduced spectral profile for SZ Tau. The spectrum has been normalized to continuum points and has been divided between the upper and lower panels.

CCDRED can be used to normalize a spectral profile through either manual user input or an automated routine. In manual normalization the user selects continuum points by lining up the vertical mouse cross-hair in the horizontal position of the continuum point, and then pressing the left mouse button. Once at least two points are selected, a cubic spline is fitted through the selection points so that the user can visually determine whether or not the spline satisfactorily imitates the general trend of the continuum emission. If an erroneous point is selected which causes the spline to deviate too wildly from a smooth trend, the right mouse button can be clicked which will deselect the last point. In this mode the user also has the option to overlay a sequence of fully reduced spectra and ensure that each spectra is normalized to the exact same continuum points, granted that there be little Doppler shifting between individual spectra within the sequence. The automated routine, on the other hand, divides the spectrum into a (still user specified) number of bins, and then selects the second or third highest maximum value[47] within each bin as the continuum point for the bin. Again, a cubic spline is used to fit the points. The automated routine will not ensure that the same continuum points are used for each bin, and it can also have difficulty when there are very wide absorption features such that the bin width is too small to contain a continuum point, as can easily happen in the calcium H and K absorption line region seen in Figure 3-23. Spectra with wider spacing (and hence more continua) between lines are normalized quite well with the automated routine, and it also takes less time to perform. In either case, after the cubic spline is formed, the spectrum is divided by it and this normalizes the points in the continua to unity. And if necessary, the process can be iterated.

---

[47] The second or third highest value is used instead of the maximum value, since the maximum point will in general be due to a noise fluctuation.

The spectral dispersion can in principle be determined through measurements of the pixel positions of the stellar absorption features in Figure 3-23. However, comparison lamps were taken for calibration of the radial velocity measurements and so these have been used instead. Iron-Argon (FeAr) emission lamps were taken in pairs bracketing each stellar exposure in order to calibrate the spectrograph flexure as the telescope tracked an object across the sky (this will be discussed in the next section). Figure 3-24 shows the emission profile of the FeAr emission lamp after reduction by CCDRED, and Figure 3-25 shows the spectral dispersion.

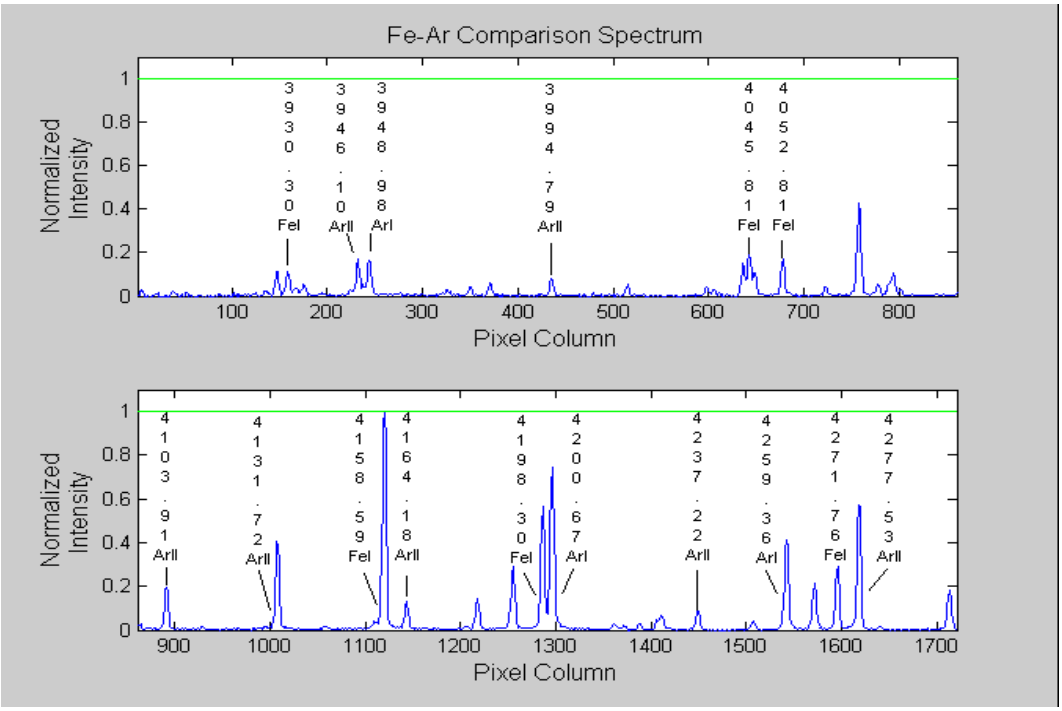

Figure 3-24: Fe-Ar spectrum. The spectral dispersion can be calibrated though measurements of the Fe-Ar emission lines. Line identifications are in Angstroms.

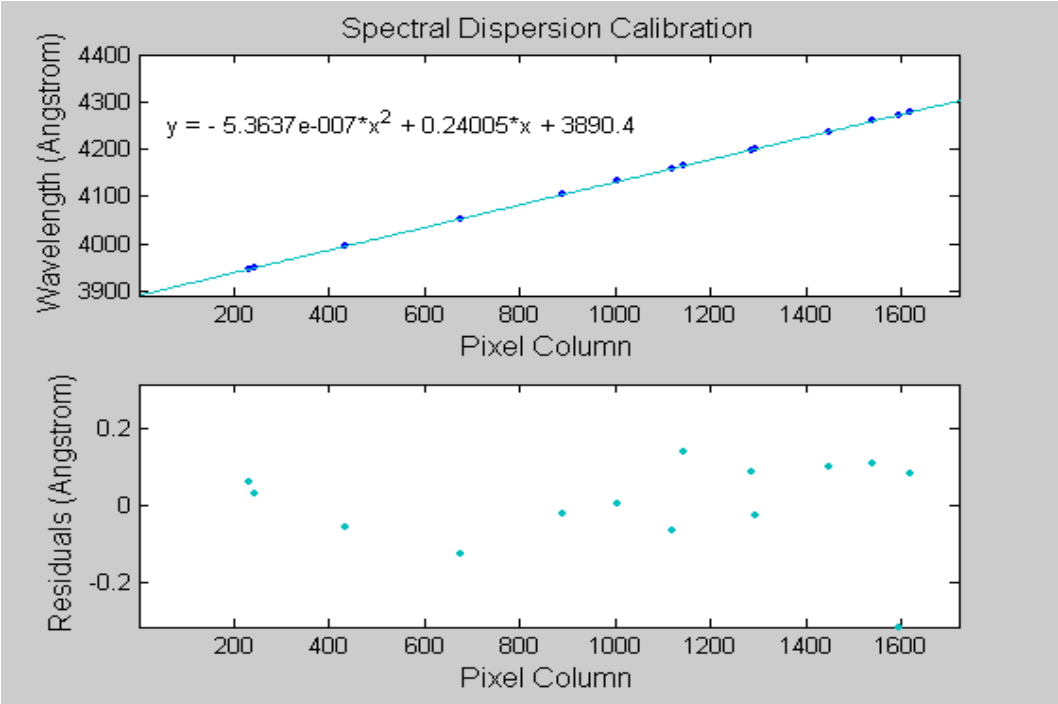

Figure 3-25: Quadratic fit through the pixel positions of fourteen identified emission lines.

The equation in the top panel of Figure 3-25 gives the distribution of wavelength with pixel column position across the chip; the spectral dispersion (in Å/pixel) is the rate of change of this equation. Although the coefficient of the second order term is quite small, including the term amounts to an angstrom of difference between the edges of the chip as compared to using only the linear terms. The mean spectral dispersion - the spectral dispersion at the centre of the chip - with the difference of the spectral dispersion at the extremities of the chip as its deviation is then

$$D = 0.23913 \pm 0.00092\ \text{Å/pixel} = 17.502 \pm 0.067\ \text{km/s/pixel}. \qquad (3.30)^{48}$$

Because the pulsational radial velocity variation of SZ Tau is known to have an amplitude in the range of 20 km/s, a maximum Doppler shift just under 1 pixel (or 0.24 Å)

[48] Wavelength can be converted to velocity through equation (3.31) for Doppler shift, discussed in the next section.

is expected. Therefore, a given spectral line's sampling dispersion will have a maximum variation on the order of $1x10^{-6}$ Å or 7 cm/s, an altogether negligible concern. This will allow the use of very simple cross-correlation techniques in determining the spectral Doppler shifts. Also, if it can be assumed that cross correlation techniques can register Doppler variations on the order of a tenth of a pixel, then an accuracy of 1km/s can be expected in the determination of the radial velocities.

3.2.2 Procedures in Radial Velocity Variability Detection and Analysis

Radial velocities are measured via the Doppler variation of spectral lines, which manifest themselves through positional changes in the location of spectral absorption features on the CCD image. Doppler shifts arise when an object emitting (or reflecting) light is not in a radially stationary position relative to the observer measuring the light. This occurs via any of several processes, including the binary orbit of two stellar companions, pulsation of the photospheric layer of a stellar surface, or the recessional velocity of distant galaxies, among many others. In the last case the Doppler shift is more or less constant, whereas for the former two the shift is of a variational nature. In the case of variable stars it is due to the periodic radial expansion and contraction of the photosphere.

If the spectral dispersion of the data is known (as discussed in Chapter 3.2.1), then the wavelength Doppler shift $\Delta\lambda$ is related to the velocity v of the source by

$$\frac{\Delta\lambda}{\lambda} = \frac{v}{c}, \tag{3.31}$$

where λ is the rest wavelength of the spectral line and c is the speed of light in vacuum.

The first spectral Doppler shifts were measured through line-positioning techniques on photographic plates. In this case a binocular microscope (or perhaps even by eye and ruler) would be used to measure the centroid of a spectral line on the plate, and a sequence of these measurements on a batch of spectral data would yield the relative variational Doppler shifts. The positions of identified spectral features could then be compared to

those from a test source situated in the laboratory, allowing absolute calibration of the radial velocities with respect to the observer. Measurement of the positional shifts of multiple lines on each plate would allow for the formation of a mean value and an associated error of measurement through its standard deviation. Now automated, techniques such as this are used fruitfully in the digital era. Other methods have become widespread with the advent of high-speed computing, such as the cross-correlational method which is used and discussed presently.

For discreet functions, such as those pertaining to digital spectra of an integer number of elements, the cross-correlation can be expressed as

$$X(m) = \begin{cases} \sum_{n=0}^{N-m-1} x_{n+m} y_n^* & m \geq 0 \\ X^*(-m) & m < 0 \end{cases}, \tag{3.32}$$

where * indicates the complex conjugate (but because both 'x' and 'y' are real the complex conjugates can be ignored). Equation (3.32) does not lend itself well to interpretation. However, cross-correlation is also called the sliding dot-product, and this is because the functional effect is to "slide" the sequence *x* over the sequence *y* in integer steps, where the dot-product of corresponding elements (i.e. elements that lie on top of one another) is the value for the correlation at that particular lag. The "lag" refers to the difference of the positions of elements within the first sequence relative to the corresponding elements in the second sequence. For example, at zero lag the elemental indices of both sequences are aligned, and the full dot-product of the two sequences then gives the correlational value. At lag = 1, element 2 in the 1st sequence corresponds with element 1 in the 2nd sequence, element 3 in the 1st to element 2 in the 2nd, and so on. In the first case, element 1 in the first

sequence and element N (where N is the length of the sequences, assumed equal) in the second do not contribute to the dot-product because they have no corresponding elements in the other sequence. The correlation lags then extend to ± (N-1) on either side of zero, so that the correlation sequence contains 2(N-1)+1 = 2N-1 elements[49].

Figure 3-26 shows the cross-correlation between two FeAr (iron-argon) emission spectra taken approximately 3.5 hours apart. Before the cross-correlation was performed each spectrum was subtracted by its mean value, and was also multiplied by a cosine-bell apodizing function in order to suppress sinc function ringing in the correlation peak wings. Near zero lag, where the corresponding emission lines from each spectrum line-up with one another, an absolute maximum in the cross-correlation occurs. The secondary maxima in the top panel of the figure are due to the correlation of unrelated emission lines as one spectrum is slid over the other. The 41 lags surrounding the maximum lend themselves well to fitting with a Gaussian function, as displayed in the bottom panel of Figure 3-26, and this can be used to determine if there was any spectral shifting between the two spectra. If there was zero shift between the two spectra, or if a spectrum was correlated to itself[50], the maximum of the correlation sequence would occur at exactly zero lag. A shift in the line positions between the two spectra will reflect itself in a shift of the correlation maximum, i.e. the center of the Gaussian, from zero lag.

---

[49] The addition of 1 is for the value of the correlation at lag = 0.
[50] Self-correlation is commonly referred to as auto-correlation.

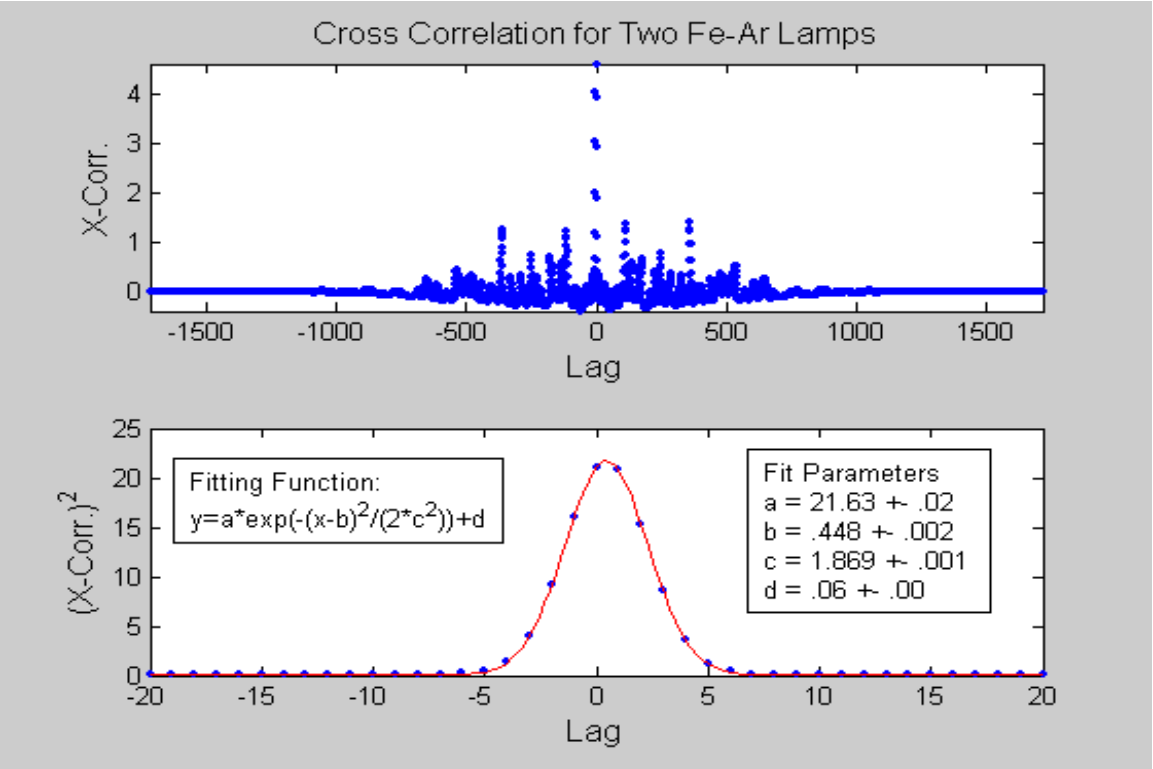

Figure 3-26: Correlation sequence of two Fe-Ar reference spectra. The top panel shows the correlation sequence over the entire range of the data, while the bottom panel is centered on the maximum peak and has been fitted with a Gaussian.

The fit parameters in the bottom panel of Figure 3-26 show a pixel shift of $dp = 0.448 \pm .002$ *pixels* or $dv = 7.84 \pm 0.03$ *km*/s. However, because the correlation was between two calibrating FeAr emission spectra, this shift is *not* due to a Doppler shift of the spectrum. Because the FeAr emission lamps are attached to the spectrograph, their shifts actually reflect the instrumental effect of a varying spectrographic geometry.

Miniscule variations of the optical path arise in almost any type of spectrograph, and great effort can be expended in reducing their magnitude. Floor mounted spectrographs, such as those in the Coude configuration, suffer the least variation because they are mounted firmly to the ground. But even nightly temperature variations can still produce spectral shifting on the order of one hundred meters per second due to the thermal expansion and

contraction of the spectrographic components[51]. Telescope-mounted spectrographs suffer from a variable gravitational torque[52] as the telescope tracks an object across the sky, and this can lead to spectral shifting of several km/s, as shown below in Figure 3-27. Because the real stellar Doppler variations are expected to have an amplitude near 20 km/s, these pseudo-Doppler shifts of the spectrograph are not insignificant and must be corrected. This can be done by fitting any type of reasonable equation to the FeAr reference lamp shifts as a function of time. In Figure 3-27, a single reference lamp was taken between each stellar exposure as the telescope tracked a star across the sky over a period of about 3 hours. Note the continuity of the curve indicative of a smoothly varying gravitational geometry. However, if the telescope were moved significantly off-target and then moved back into position, one could not be certain that the shifts would resettle into their previous trend. Also, if the same target is observed two nights in a row, it is still not certain that the spectrographic shifting during the two nights will mimic each other. Multiple exposures of the reference lamps should also be taken between the stellar exposures instead of just one, because they are usually bright and therefore impinge very little on the duty cycle. This would allow for true characterization of the internal consistency of this method of flexure calibration.

---

[51] This statement follows from spectroscopic work the author performed at the University of Western Ontario's Elginfield Observatory, which houses a Coude spectrograph of resolving power 100,000.
[52] This is also referred to as 'flexure'.

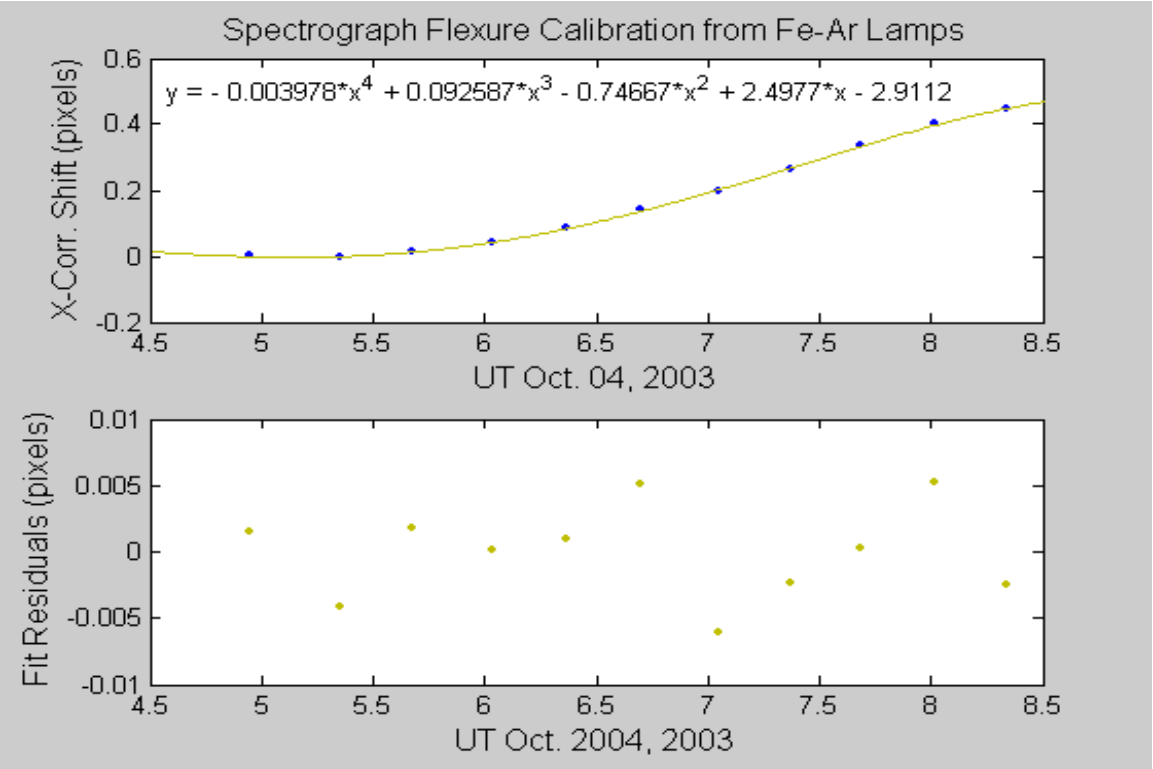

Figure 3-27: Spectrographic flexure as measured through the flexure-induced Doppler shifting of FeAr reference lamps.

The cross-correlational stellar spectral shifts will be a superposition of the spectrograph flexure-induced spectral shifts, Doppler shifts due to the orbital and rotational motions of the earth, and the real spectral Doppler shifts due to the star's intrinsic variable motion. To produce a sequence of radial velocity measurements over time, a single reference stellar spectrum and calibrating FeAr lamp (usually the first pair, or perhaps the pair with the highest SNR stellar spectrum) must be used for all the spectral cross-correlations in the sequence, and these provide an arbitrary zero point reference for the variations. A curve for each continuous set of FeAr shifts is made, and each of them is interpolated to the time of mid-exposure for each corresponding stellar spectrum. These interpolated values are then subtracted from the stellar Doppler shifts in order to correct the

pseudo shifts of the spectrographic flexure. An additional correction arises for long stellar exposures with FeAr lamps spaced widely apart, given that there may be a significant difference between the FeAr reference spectrum zero-point and its interpolated shift at mid-exposure of the reference stellar spectrum. There should be no correction between these two shifts, so the difference between the interpolated zero-point of the FeAr reference spectra and the zero-point stellar shift should be subtracted from the FeAr shift set as well, in order to force that difference to be zero.

Finally, the Doppler variations due to the radial velocity variations of the earth with respect to the direction in the sky of the target object must be corrected. These variations arise from both the rotational and orbital velocities, so that when the object is on the meridian the rotational radial velocity is zero (and maximum at HA = $\pm 6^h$), and so that when the object is in opposition to the sun the orbital radial velocity is zero (and maximum when in quadrature with the sun). Standard algorithms[53] can be used to determine the radial velocities along the line of sight to the object, and these in turn are subtracted from the Doppler shifts found above.

[53] See Appendix A: Heliocentric Julian Day and Radial Velocity Corrections, for a Matlab script.

3.2.3 Fourier Representation for the Radial Velocity and Radial Displacement Curve & Comparison to Published Data

With the results from the section on photometry for the epoch and period of the stellar oscillation, the radial velocity variations were phased according to their heliocentric Julian date at mid-exposure. A visual analysis was carried out in order to determine the correct order for the Fourier fit, using the lowest possible one so as not to inadvertently induce non-physical high frequency variations in the curve.

For the sparse number of spectra that were taken at the DAO a first order sinusoidal term plus an offset sufficiently modeled the data, as shown below in Figure 3-28.

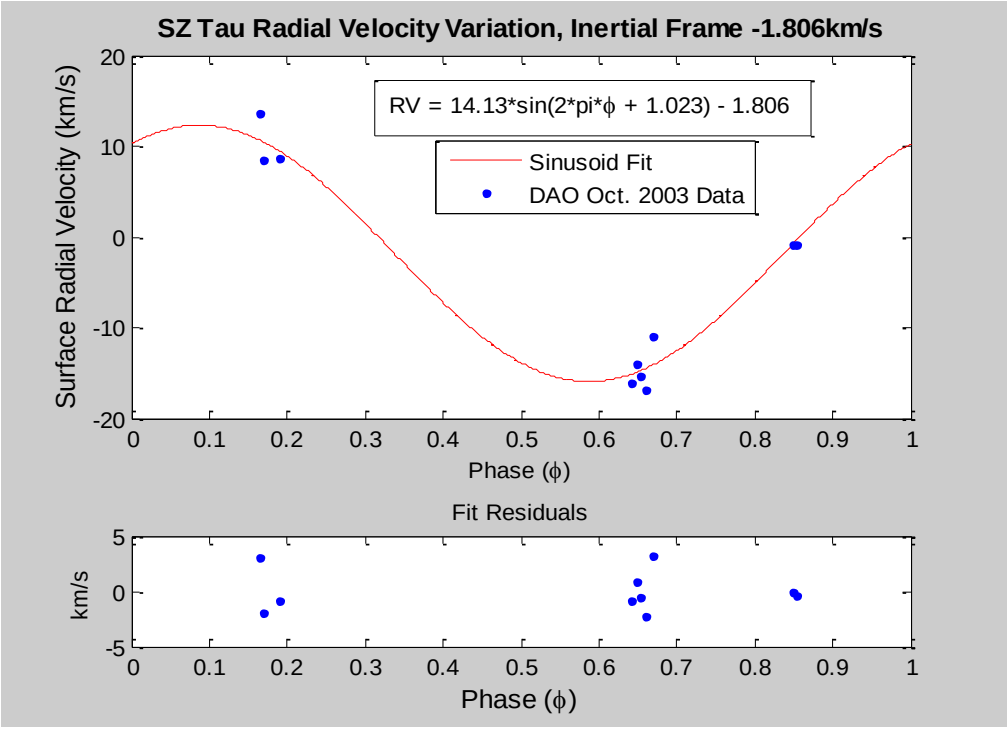

Figure 3-28: Radial velocities from the DAO, Oct. 2003. The data and their fit have been zeroed out to the mean and are oriented in the stellar inertial frame.

As these data alone are insufficient for the analysis in the Baade-Wesselink and Balona methods, published values were used. The author would like to note that precise radial velocity data are extremely hard to come by, even for a bright Cepheid which one would expect to have been studied extensively in the past. Most of the sources found (Barnes 1987; Bersier et al. 1994b; Gieren 1985; Haynes 1913; Kiss & Vinko 2000; Schmidt 1974; Wilson et al. 1989) were of insufficient precision for current use. It is difficult to obtain good spectra, more so when they must be properly calibrated with reference to standard stars[54] and/or emission lamps for radial velocities. It is additionally difficult to obtain good spectra with only one or two meter class telescopes (the type that are easy to receive observing time on), as the limiting magnitude for these are quite bright and integration times quite long. Long integration times are inconsequential to the SN ratio of the data if the CCD chip is adequately cooled (with LN_2 for example), however for short period stars one must avoid the spectral blurring intrinsic to observing a non-stationary spectrum over too large a fraction of the pulsational cycle. For most longer-period Cepheids a typical 2-hour integration would amount to an inconsequential fraction of the period, but for SZ Tau such an integration would occupy approximately 0.5 km/s in intrinsic Doppler shift of the spectrum. Additional blurring comes from the change in line-of-sight velocity towards the object due to the rotation of the Earth, which can also amount to approximately 0.2 km/s if the integration was centered on the meridian and the object near the celestial equator. These are all issues to consider when designing an observing plan.

---

[54] Following the discussion in Chapter 3.2.2, it should be noted that if one is only using stellar reference spectra for the radial velocity calibrations, it is not possible to account or correct for the underlying spectrographic variations due to the different gravitational pointing geometries between the target and reference stars. The use of standard stars is only sufficient only when it is known that the spectrographic variations are small enough to be ignored.

The data of Bersier et al. (1994b) were the best available for SZ Tauri: they have the largest number of data points spanning the pulsation cycle, and the lowest amount of scatter in the curve. Their data were epoched and phased to those values listed in the paper, and the results are shown below in Figure 3-29. Gieren (1985) also has reasonably precise data, and they agree perfectly with Bersier et al.'s. There is also generally good agreement between the DAO data and that shown here, although the DAO data do have significantly larger scatter. As is the common practice, the Bersier data were listed in the observational frame and so it was necessary to reframe them for use in the present analysis. The author prefers to place the frame of the radial velocity variations in that of the observed star for general publication, because it is the absolute expansion and contraction of the star which concerns us most, not the motion of the star toward and away from us.

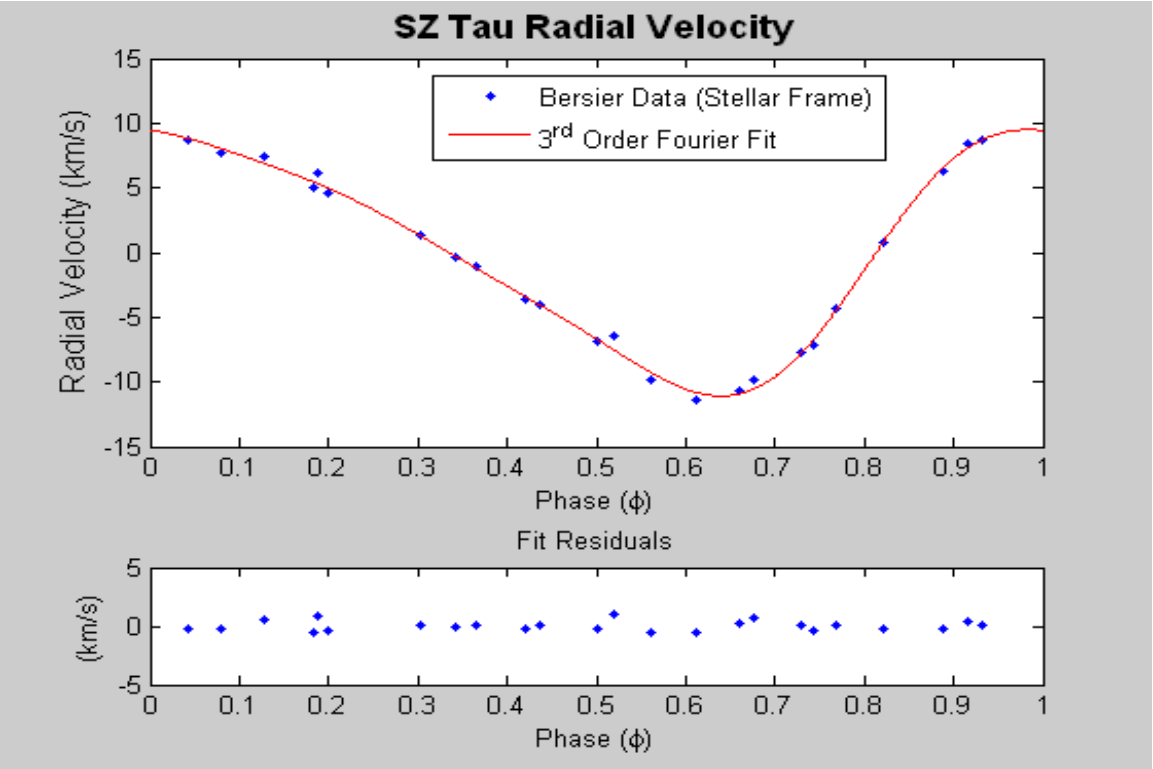

Figure 3-29: Radial velocity data from Bersier et al., 1992.

A third order Fourier fit modeled the data well and takes the form below in equation (3.33); the coefficients follow in Table 3-8. The angular frequency ω is 2pi because the data have already been phased, and φ is of course the phase.

$$RV(\varphi) = a_0 + a_1\cos(\omega\varphi) + b_1\sin(\omega\varphi) + a_2\cos(2\omega\varphi) + b_2\sin(2\omega\varphi) + a_3\cos(3\omega\varphi) + b_3\sin(3\omega\varphi) \quad (3.33)$$

Coefficient	Value (km/s)
a_0	0 (0.6017)
a_1	8.473
b_1	4.274
a_2	1.396
b_2	-2.010
a_3	-0.4276
b_3	-0.4625

Table 3-8: Coefficients for the 3rd Order Fourier Radial Velocity Fit

Note the entry for the coefficient 'a_0' in the above table: When a Fourier fit is performed on any set of data, the first term in the fit is simply the data's mean value. This value can be due to any sort of bias offset, but in the case of *fully calibrated* stellar radial velocity measurements, it is the systemic line-of-sight radial velocity of the star. So the bracketed value for "a_0" is thus from the fit of the data. However, in the mean inertial frame of the star there must be no net radial velocity residual, so that over a pulsational cycle the star returns to its previous radius and there is no overall increase or decrease in the star's mean volume[55]. Therefore, when integrating the radial velocity curve such as to obtain the corresponding radial displacement, the value for "a_0" must be set to zero. Also, integrating for the stellar radial displacement is the reason why the radial velocity data must be framed in that of the star, and not in that of the observer.

[55] On time scales very much smaller than those of stellar evolution.

Bersier, et al. (1994b) state that the CORAVEL radial velocity data require a zero point correction:

$$RV_{absolute} \simeq RV_{CORAVEL} + 0.4\ km/s, \tag{3.34}$$

so that the systemic mean radial velocity of SZ Tau is

$$< RV > = 0.6017 + 0.4 = 1.017\ km/s. \tag{3.35}$$

Here we used the value of "a_0" in regards to our frame of reference, and so took its positive value from that of Table 3-8.

Although the Bersier data originate from a different epoch, it is not expected that gross variations in the shape of the radial velocity curve have occurred between the date of their observation and that of the MLO photometry. While minor variations in the period have been reported[56] for SZ Tauri, the sinusoidal nature and amplitude (Platais & Mandushev 1993) of its phased light curves have remained constant. It ought to follow that the radial velocity curve has remained constant in phase as well. Certainly the best circumstance would be having simultaneously observed photometric and spectroscopic data. Not having contemporaneous radial velocity data is likely the principal source of error in the work presented here, although that is impossible to quantify.

The stellar-frame Fourier fit of equation (3.33) and Table 3-8 can easily be integrated for the determination of the stellar radial displacement, and this is shown below in Figure 3-30. If the integration is performed numerically, it is necessary to subtract the mean value from the result so that the displacement correctly brackets zero. The equation can obviously be integrated analytically and in this case the curve will correctly bracket zero displacement.

---

[56] However, these are somewhat dubious given the author's evaluation in Chapter 1.2.

It is important to have the displacement curve correctly zeroed as this corresponds to the mean radius of the star, which we aim to determine. Note as a simple general observation that the star's outward expansion is less than that of its inward contraction, and hence spends more time larger than its mean radius than it does smaller. With the radius determined in Chapter 4, the radial variation amounts to approximately two percent of the mean stellar radius.

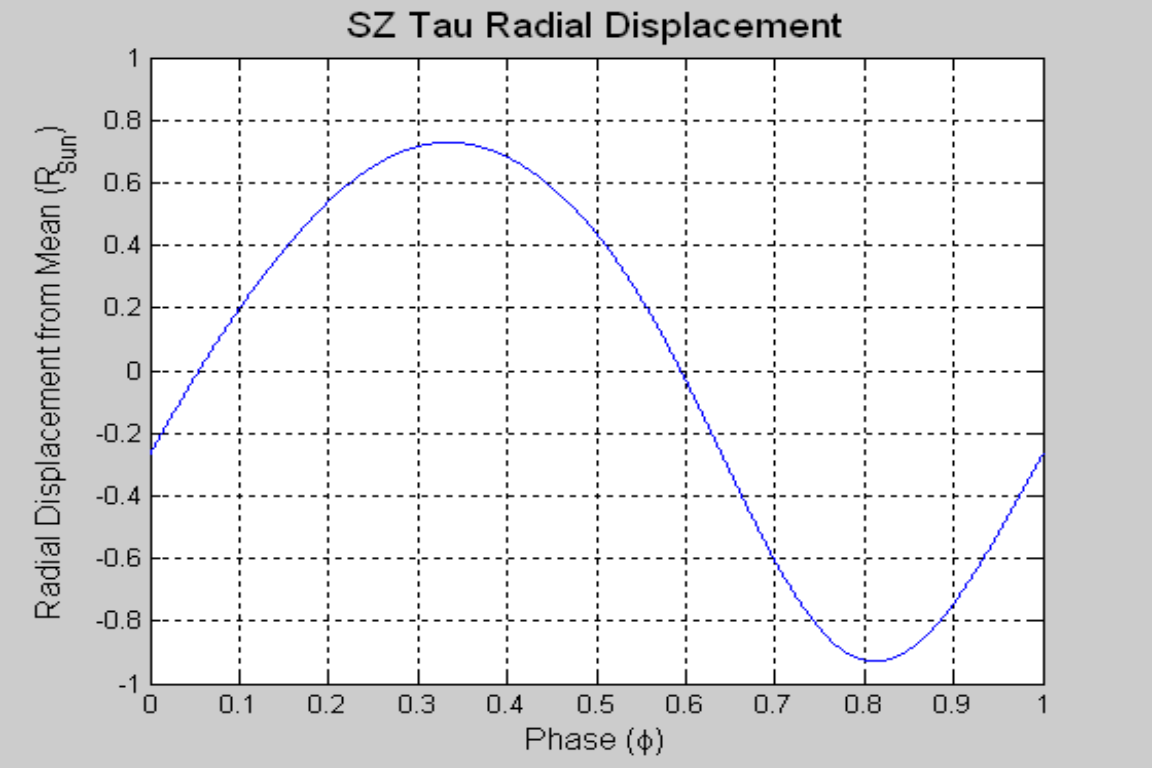

Figure 3-30: Integrated radial velocity curve. The displacement curve has been zeroed to its mean and the projection factor has been applied.

A projection correction must be applied to the integrated velocity curve in order to obtain a more physically accurate model of the stellar displacement. In most cases the radial velocity data ultimately come from some form of spectral line positioning technique.

However, spectral lines are stellar-disk integrated phenomena, and so the observed radial velocity is the sum of all vector components: those pointing directly toward the observer at the centre of the disk, components pointing at right angles to the observer at the edge of the stellar disk, and all components in between. In the first-order approximation, the projection factor is the disk-integrated product of projection annuli weighted with model limb darkening intensity values. For this work, we used the relation from Gieren et al. (1989)

$$p = 1.39 - 0.03 \log P \tag{3.36}$$

where 'p' is the projection factor and 'P' is the period (in days) of the Cepheid in question. For SZ Tau's period of $P = 3.1488$ *days*, the projection is factor is $p = 1.375$.

Sabbey et al. (1995) explore the behaviour of the shape of spectral lines over the pulsation cycle. They report the need for a phase-dependent *p*-factor due to line symmetry variations changing systematically between the expansion and contraction phases, ultimately due to changes in the atmospheric depth of the line formation over the cycle. Gray (2007) used spectral-line modeling to fit observed spectra in a successful attempt to determine directly the radial velocity variations of the surface of a star, instead of converting from an observed radial velocity to a pulsational one through the *p*-factor. His method can easily be turned around such as to directly calibrate the *p*-factor as a function of phase and period, although he did not have a statistical sample with which to do so – the work was more of a proof of concept based on a small sample of representative Cepheids.

Figure 3-31 below shows the relevant observational data curves required for the Baade-Wesselink and Balona analyses. If we recall equation (2.8)

$$m(\varphi) = A \cdot CI(\varphi) + B - 5\log(R_0 + \delta R(\varphi)),$$

we see that if a star did not vary in radius the logarithm term could be absorbed into the constant, and the magnitude would then scale directly with the colour index. But because the colour index is representative of the stellar effective temperature, one would not expect colour index variations without changes in radius due to simple thermodynamics. If the radial displacement $\delta R(\varphi)$ is non-zero and not in phase with the temperature variation, the magnitude and colour curves will no longer directly scale to each other. The radial displacement term will then act as a perturbing or correcting effect, the degree of which depends on R_0, which then combines with the colour curve to produce the light curve. This can be seen directly in the figure below. Note that the displacement curve lags the light curve by about 0.34 phase, while the colour index lags it by about -0.04 phase.

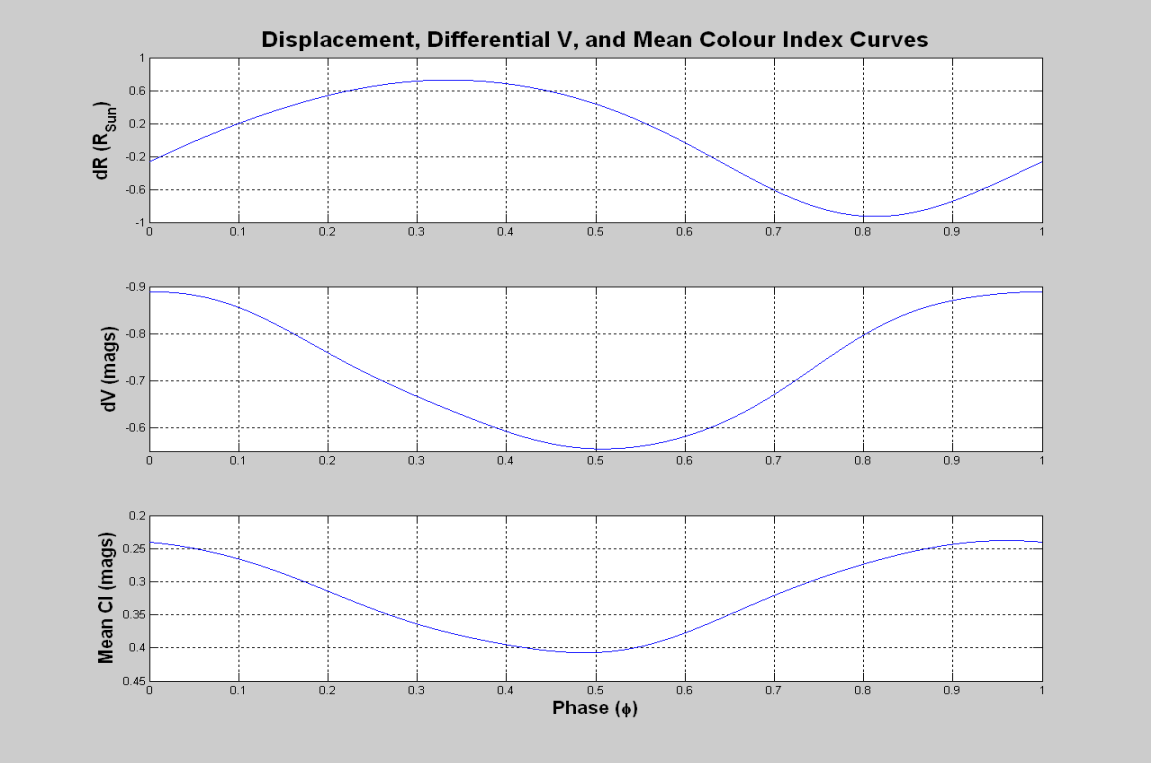

Figure 3-31: Displacement, Differential V, and Mean Colour Index curves.

Chapter 4: Results

4.1 Baade-Wesselink Analysis

The basic methodology of the Baade-Wesselink method was introduced and discussed in Chapter 2.1; here it is applied to the data of SZ Tau discussed in the previous sections.

A graphical user interface (GUI) software program, called BaadeWesselink.m, was written in MATLAB to facilitate the analysis. A screenshot is presented below in Figure 4-1.

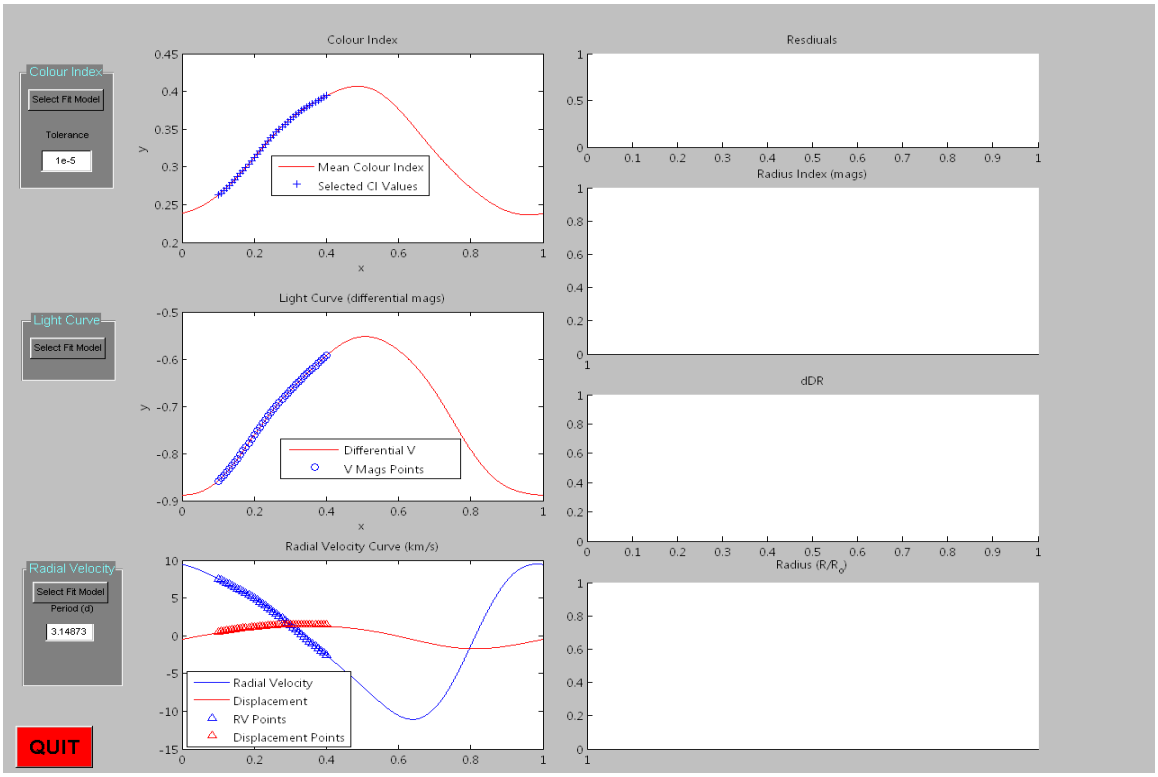

Figure 4-1: Screenshot of Matlab GUI BaadeWesselink.m.

Upon entering the program the GUI prompts the user to open the relevant files for the analysis. Following the derivation of the method in Chapter 2.1, the required input data are the differential magnitude curve, the radial displacement curve, and the colour index curve. The colour index curve used in the analysis is the one from Figure 3-12, i.e. the mean colour index of the 4 adjacent-filter combinations of the five UBVRI passbands. Because only the phases of equal colour index are needed in the solution, the colour index curve does not need to be fully standardized. Using the mean colour index curve allows for unique solutions to the radius in each of the five passbands, which will be the averages of the results if each colour index and passband combination were used individually (as is commonly done; for example see Milone, et al. (1999)).

After loading the files, one is prompted to select the region of the colour index curve to be used for determining the points of equal value on the alternate branch of the curve. This can be selected manually or default to the range $\varphi = 0.1$ to $\varphi = 0.4$ as shown in Figure 4-1. It is best to use the steepest part of the index curve for these points as their phases are necessarily more well defined there, due to the slope of the curve being highest in that region. It is also necessary that the selected points be not too near each other on either side of the curve, because the difference in magnitude at phase points close together necessarily goes to zero and results in an indeterminate solution. This is a problem the Balona solution avoids, as we will see in the next section. An arbitrary number of forty points is evenly spaced throughout the range, and each is used in the subsequent solution. Because the number of points which is used in the solution is arbitrary, it is possible only to determine a mean radius from the set of solutions, and no realistic estimate can be made of the error on the mean because this arbitrarily scales to zero as the number of points increases to infinity.

At *each* solution however, it is possible to calculate an individual error through standard differential techniques, such as those described in Melissinos (1966).

The final task is to select the search region on the alternate side of the colour index curve for the determination of the forty corresponding phases of equal colour index. The user graphically identifies the region of the curve in which to find values of equal colour index, so in the case above selecting from $\varphi = 0.5$ to $\varphi = 0.95$ would be appropriate. Because the colour index curve is usually a noninvertible function, such as a truncated Fourier series, it is necessary to iterate within the region $0.5 \le \varphi \le 0.95$ to find the corresponding colour value and its phase within some specified tolerance. Typically a tolerance of $\pm 10^{-6}\ phase$ (or $10^{-6}\, xP = 0.27\,\mathrm{sec}$) was used, which is much smaller than the associated photometric errors translated into the time coordinate via the slope of the index curve. For example, the slope on the left branch used for the initial point selection is roughly

$$\frac{0.4 - 0.25}{0.45 - 0.05} = 0.375\ mags / phase\,.$$

The average error of the mean colour index curve from Figure 3-12 is 0.006 mags. The average error translated from the photometry into the time dimension is then

$$\frac{0.006\ mags}{0.375\ mags / phase} = 0.016\ phase\,.$$

This is much greater than the tolerance value, and almost 2% of the phase[57]. This simple analysis also shows that the solution of the Baade-Wesselink method breaks down for point pairs near the minima and maxima, where the slope of the index curve nears zero.

For each of the forty points on the ascending-branch in Figure 4-1, the alternate region is searched for an equal value to within the specified phase tolerance. The algorithm begins by calculating the value of the index curve at the midpoint phase of the search range. If the calculated value is greater than the comparison value, the phase point steps ahead by half of the search range. This time the calculated value will be too low, so the step is divided by 2 and the phase point moves back by thence a quarter of the search range. If the new calculated value is once again too high, the step is halved another time and the phase point jumps forward by an eighth of the search range. This process is repeated until the step size becomes less than the tolerance value, when the corresponding phase of equal colour index is recorded, and the Baade-Wesselink solution is calculated. The iteration then exits and is repeated for the remaining points from the left side of the index curve. Figure 4-2 below shows the result, continuing from Figure 4-1.

---

[57] Two percent of the phase is a non-trivial translation of the error, and 0.006mags in photometric colour index dispersion is reasonable for ground based work.

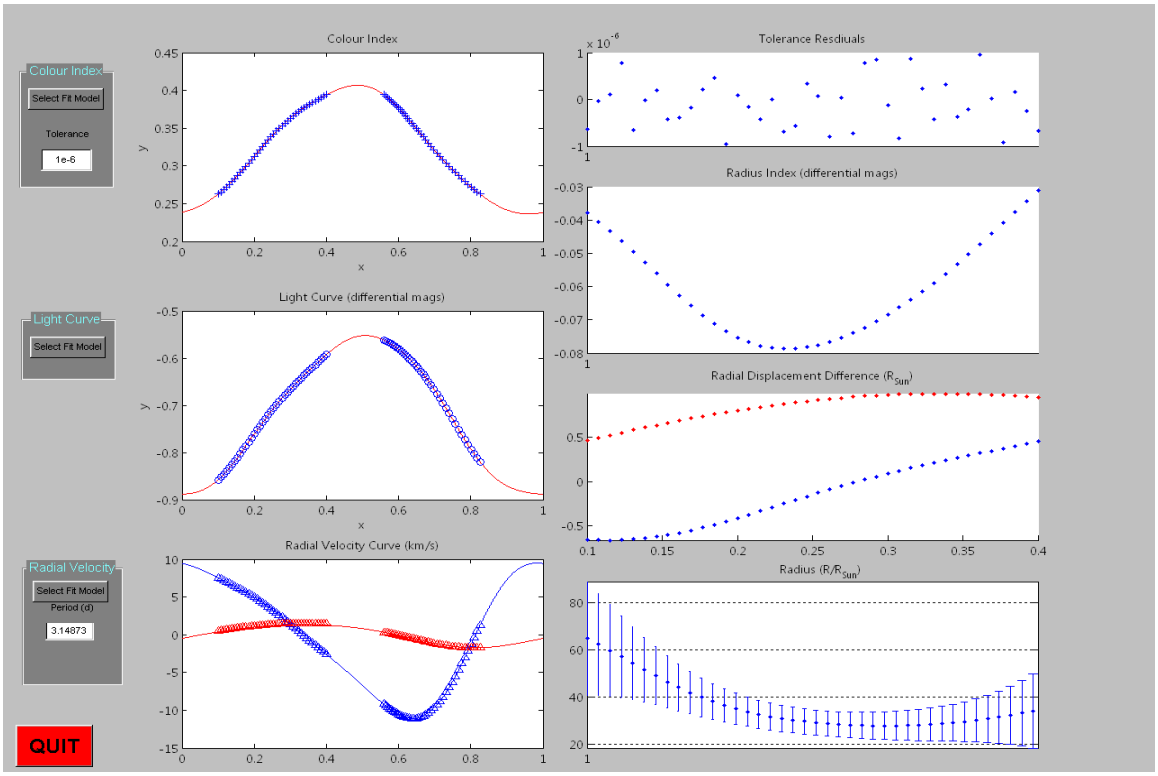

Figure 4-2: BaadeWesselink.m after the sequence of iterations.

The top plot on the right hand side of Figure 4-2 shows the step size reached at the last iteration and these are all, of course, less than plus or minus the tolerance value. The middle-plot on the left in the above figure shows that at phases of equal colour index, the magnitudes are not the same and differ by the amount shown in the 2nd plot in the right hand column. This is due to the radius of the star not being the same at these phases, differing by the amount shown in the 3rd plot on the right column. Recalling the Baade-Wesselink solution

$$R_0 = \frac{\delta R(\varphi_2) - 10^{-.2MI_{2,1}}\,\delta R(\varphi_1)}{10^{-.2MI_{2,1}} - 1}, \tag{4.1}$$

$\delta R(\varphi_1)$ and $\delta R(\varphi_2)$ are the radial displacements at the respective phases of equal colour index (3rd plot, right column), and $MI_{2,1}$ is the difference in magnitude (labeled 'Radius Index'

in the figure) of the light curve between the phases φ_2 and φ_1. The distribution of solutions for R_0 (in solar radii) at each of the forty phase pairs of equal color index is shown in the bottom plot of the right hand column. The results for the five UBVRI passbands are shown in the next figure.

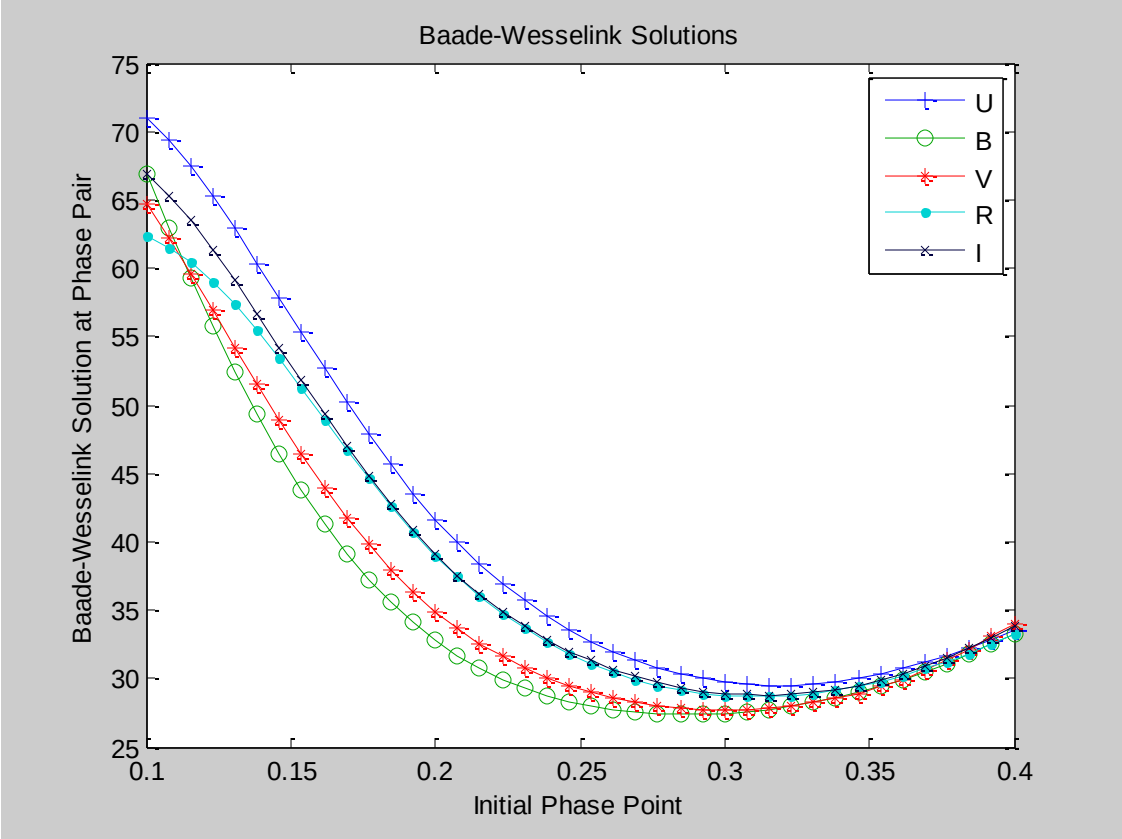

Figure 4-3: The distribution of Baade-Wesselink solutions for the UBVRI passbands.

It is immediately apparent that the Baade-Wesselink solution can produce a very wide range of solutions for the mean radius, depending on which phases are used. Other authors have utilized large numbers of combinations of indices with passbands such as to dampen the statistical errors for a better estimate on the passband-averaged mean solution

(as done for example in Milone, et al. (1999)). Nevertheless, it is discomforting to see such a large variation in the solution for the radius - one would expect to see a flatter distribution of solutions with phase. Certainly, narrowing the phase range for the solutions will hide the large range of variations in the solutions. The reassuring observation is that all passbands follow the same general trend, and this may indicate that the problem is systemic to the data. A problem previously mentioned in this work is that the radial velocity data used were archival. However, redeterminations of Gieren's 1985 and Bersier et al.'s 1994 data using epochs from photometric data close in time to their observations, and using the average period from Table 1-2, show no changes in shape or in phase. The effect of a mismatch in phasing between the light and RV curves, which would be the most obvious (and simple) problem, has nevertheless been investigated. The radial velocity data were shifted in phase by plus and minus 0.1*phase*, and the resultant distributions of solutions were compared to the solutions with no change in the phasing. The results for the V passband are shown below in Figure 4-4.

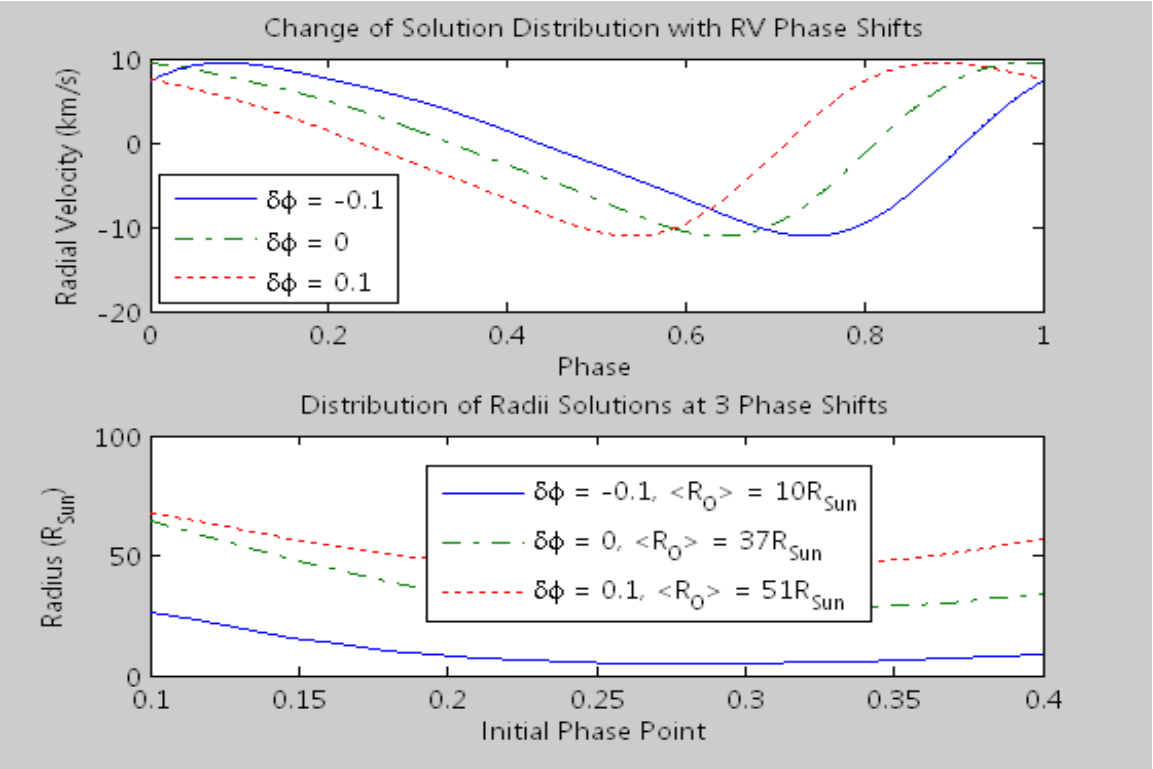

Figure 4-4: Radius solutions and RV curve phase shifts.

A rough linear fit to the mean of the three solution curves indicates sensitivity, valid only around the range of RV phase shifts $-0.1 < \Delta\varphi < 0.1$, of 2 solar radii per percent of phase mismatch between the radial velocity and photometric curves. Sensitivity such as this is expected, and indicates the significance of the limiting 2% error in phase-point selection accuracy of the colour index data discussed earlier, implying a fundamental accuracy limit of 4 solar radii in any single solution. Of course, the added uncertainty in the radial velocity and single-passband data only serve to push the accuracy to lower (i.e., higher solar radii) limits than this.

Ultimately, it is apparent that small phase mismatches between the photometric and radial velocity data only raise or lower the mean value of the solution, while the general shape of the solution distribution remains relatively constant and scales roughly linearly with

the phase mismatch. In other words, the distribution of solutions was not flattened out and the worrisome large range of solutions was not corrected through this level of adjustment of the phase matching between the two types of data. Curiously, a phase shift in the RV data of -0.7 *phase* (or +0.3 *phase*) *did* produce a relatively flat solution distribution of approximately half the value, but there is clearly no way to justify such a shift given that the phases of the radial velocity data re-determined by the author were found to agree effectively exactly with what had been originally published.

Phase mismatches between the passband and colour index curves might possibly be a problem, although these are formed from the same data and so the sign of the phase discrepancy would be ambiguous. Also, this again would only raise or lower the mean value of the solution and would simply have a different level of sensitivity than that above for the RV curve phase shifts. In the discussion of the Balona method ahead, we will see why this is and why it can be expected to be so. Shifting the phase of the mean colour index curve by ±0.01 phase indicated a sensitivity of 16 solar radii per percent of phase mismatch between the colour index and light curves. This indicates how tremendously important it is to properly separate the surface flux contribution from the luminosity curve of a Cepheid.

It must be concluded that in order to change the *shape* of the solution distribution we must have a change in the pulsational shape, and not (just) the phase match, of one or several of the three input data curves (these being the radial velocity, passband, and colour index). The radial velocity curve may be the most suspect, given the comparison of the author's DAO data to that of Bersier, et al. (1994b) shown in Figure 4-5 below. However, the DAO data are too sparse to make any definitive statements. On the other hand, the differential UBVRI passband data presented in this work match extremely well with other

published data (as in Figure 3-13 on pg. 70), and the colour index curves are formed *out* of the passband data, and the mean colour index used in this analysis also matches quite well with other published data (as in Figure 3-15). In exploring the solution distributions using the four colour index curves individually, the shape of the solution distributions follow that of using the mean index curve only, and indeed for an individual passband the mean of the four unique colour index curve solutions is the same as that of using the mean index curve in the solution for that passband alone. Using *non*-adjacent passbands for individual colour index curves (for example, B-I) does not change the general shape of the solution distribution either. So at this point we have relative confidence in the colour index curves and their mean. The mean Baade-Wesselink radius in each of the UBVRI passbands and the passband-averaged result are tabulated below in Table 4-1, and plotted in Figure 4-6.

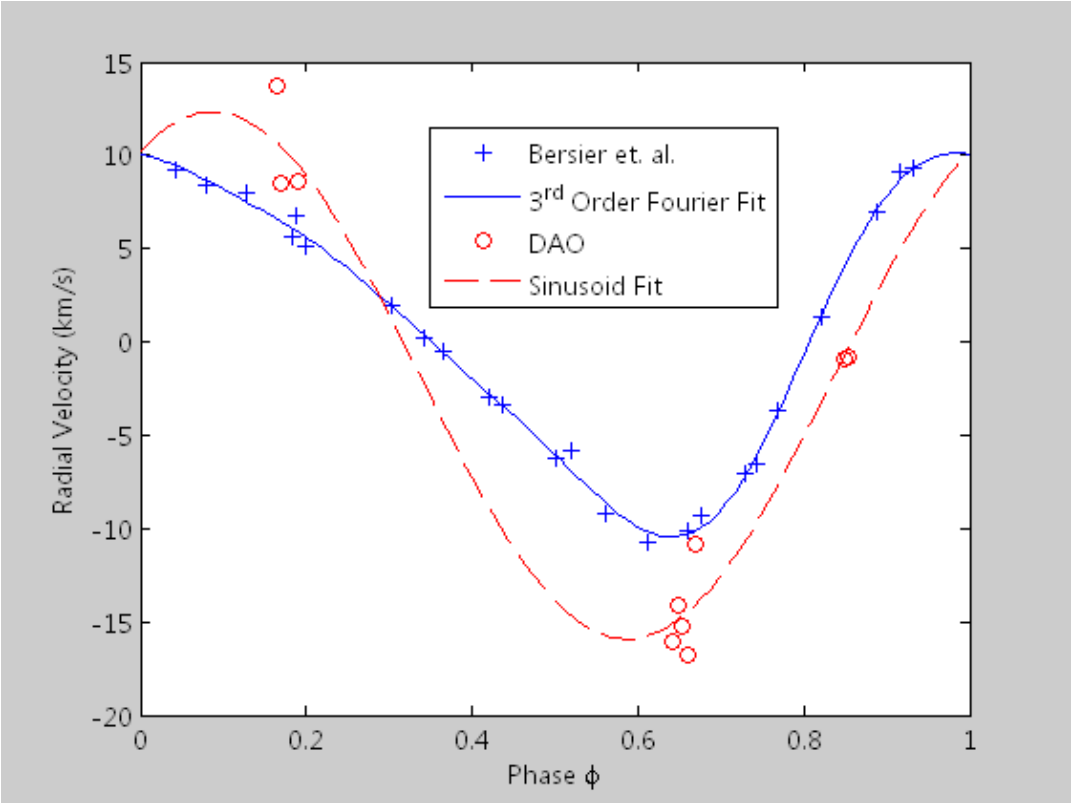

Figure 4-5: DAO and Bersier et al. radial velocity curves.

Filter	Radius (R_{Sun})	Stdv[58] (R_{Sun})
U	40.7	13.2
B	35.4	10.8
V	36.4	10.8
R	38.3	11.1
I	38.9	12.0
Mean	*37.9 ± 2.1*	-

Table 4-1: Baade-Wesselink Radii

[58] As mentioned in the text, the Baade-Wesselink method does not allow for meaningful error estimates in each of the passbands. However, one can still meaningfully take the standard deviation of the passband means as the error on the passband-averaged mean.

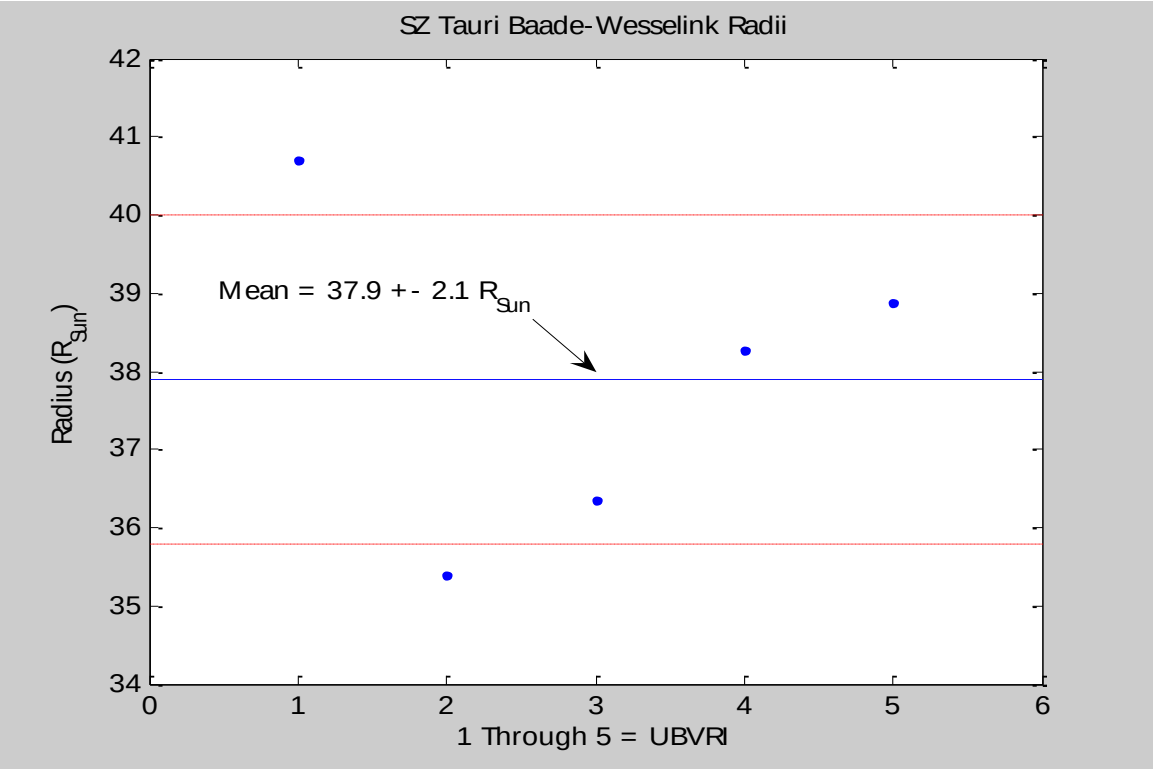

Figure 4-6: Baade-Wesselink radii. The trend of radius with passband correlates almost perfectly with the epoch lag distribution from Chapter 3.1.2.

4.2 Balona Analysis

Recall equation (2.8) from the introductory discussion of the Balona method in Chapter 2.2:

$$m(\varphi) = A \cdot CI(\varphi) + B - 5\log(R_0 + \delta R(\varphi)) . \tag{4.2}$$

Here, $m(\varphi)$ is the light curve in one of the UBVRI passbands, $CI(\varphi)$ is the mean colour index and $\delta R(\varphi)$ is the radial displacement. The parameters A and B are simple linear scaling factors, while R_0 is the mean radius of the solution - the parameter we are most interested in. The equation can be solved for the parameters numerically through nonlinear least squares data fitting with the Matlab function "*fminunc*", which determines the unconstrained[59] parameters of a given functional resulting in a least-squares minimum of the input data about the fitting curve. In practice we have a truncated Fourier series for each of the three input data curves as functions of phase, so for the input data required in *fminunc* we simply compute the Fourier curves at one thousand evenly distributed points between zero and one phase, and *fminunc* then reduces the deviance of these points from each other through manipulation of the relevant parameters within the given functional topography of equation (4.2).

It is quite informative to consider the particular role each term and each parameter in equation (4.2) fulfills. The term $m(\varphi)$ appears by itself and its role is obvious, although we

[59] There is another function for constrained parameter fitting as well, but there is no need to constrain the parameters to any range in this case, as the solution converges quickly. The algorithm uses a "quasi-Newton" iteration method as discussed in the Matlab help pages.

see on the right hand side that it arises out of the product between temperature (or surface brightness as represented by the colour index, i.e. $A*CI(\varphi)+B$) and surface area (i.e. $5log(R_0+\delta R(\varphi))$). If the star did not vary in radius (i.e., $\delta R(\varphi) = 0$) we would have that the magnitude scaled linearly with temperature, the surface area term being absorbed into the constant B in order to simply shift the colour curve up or down to match the ordinate of $m(\varphi)$. Of course in practice such a situation would never exist[60], but imagining this aids the interpretation. In Figure 4-7 it can be seen that the colour index and light curves *do* nearly scale linearly with one another, but it is obvious that a horizontal shifting in phase is needed in order to bring the curves into line with one another.

[60] Because we are speaking of curves, this would imply a variation in temperature. A variation in temperature would be associated with a variation in radius due to simple thermodynamics.

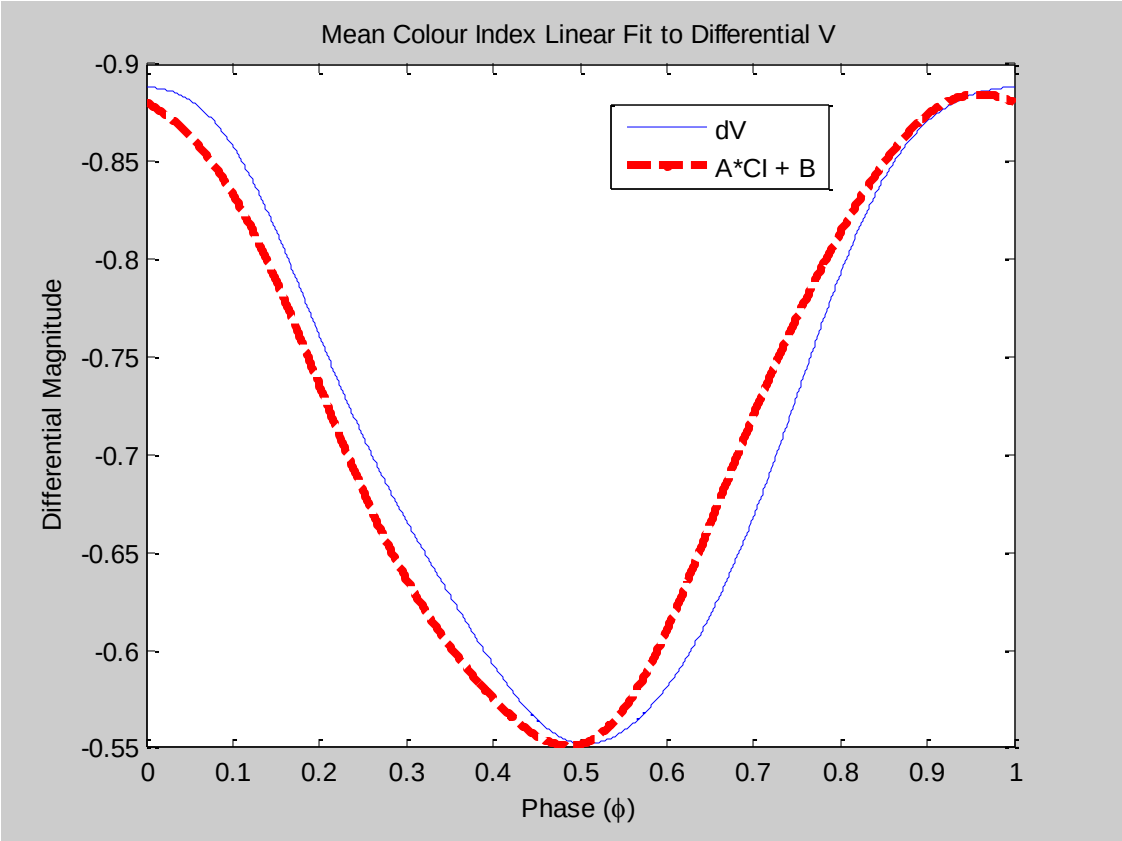

Figure 4-7: A linear fit of the colour index curve to the light curve.

Now with the surface area term a function of phase it no longer solely has an effect in simply shifting the right side of the equation vertically up or down. Essentially, one could think of $5log(R_0+\delta R(\varphi))$ as being a series of constants which depend on phase and which have a non-linear effect on the right side of equation (4.2). It is a subtle point to consider that this no longer has a role in uniform vertical shifting of the right side of the equation, but rather skews the linear colour index fit to ultimately produce a shift of the linear fit in the horizontal coordinate. If one recalls Figure 3-31 it is easy to visualize the interaction of the three input curves with one another; the plot is reproduced here.

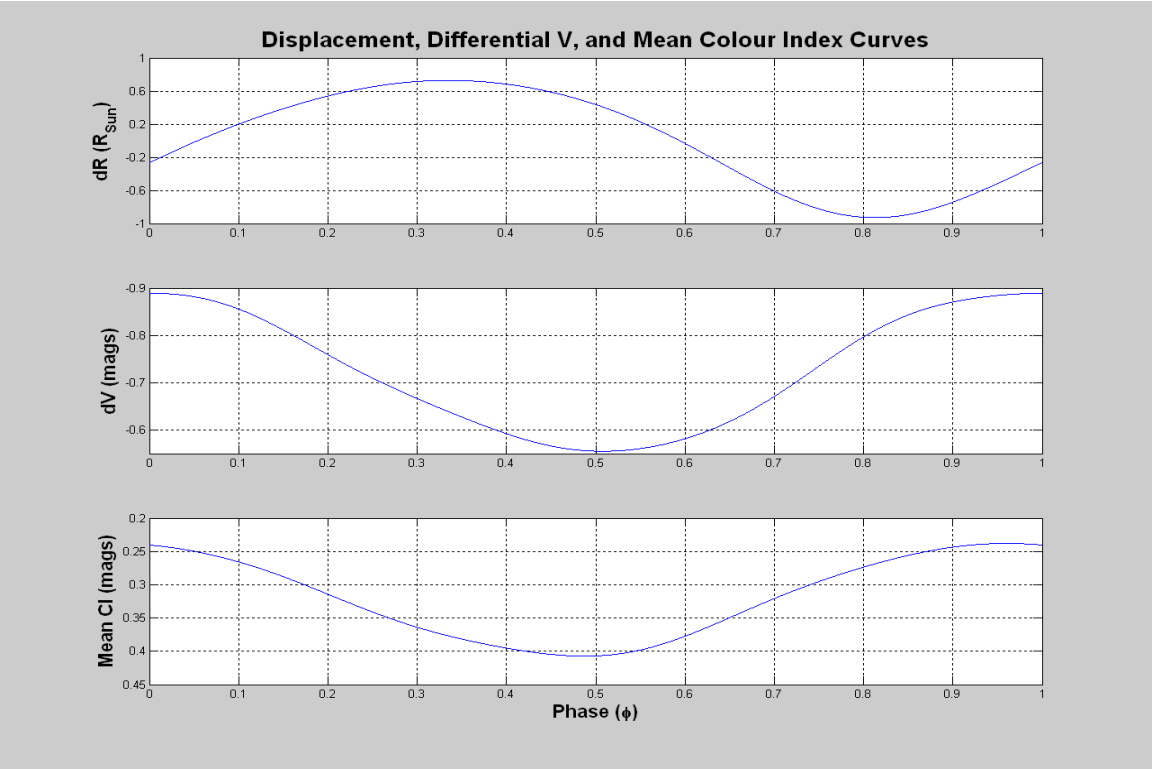

Figure 4-8: The light curve is clearly most dependent upon the colour index, with the radial displacement having a lower order perturbing effect.

The important insight is that it is the value of R_0 in the surface area term which determines the amount of horizontal skew afforded by it. For large R_0 the entire term will more closely mimic that of a simple constant, because the variation of $\delta R(\varphi)$ superimposed onto R_0 will be only a small percentage (especially after the logarithm is taken of it). For smaller R_0 the variation of $\delta R(\varphi)$ will have a greater skewing effect. In this way one can understand how the colour index and radial terms are linearly independent of one another, and also how exactly the radial term affects the solution such as to allow an estimate to be made of it in the fitting process. Essentially, the colour index *must* lead the light curve because the radial displacement lags it - they combine to produce the light curve with a maximum in between.

Note that the lag of the displacement curve is significantly more, and of the opposite sign, than the lag of the colour index curve relative to the light curve. This can be expected on two respective counts. First, the luminosity of a star is generally dependant on temperature to the fourth power, while on radius to only the second. So for changes in each of the dependencies of relatively similar percentages, it is the change in temperature which will have the dominant effect, and this is why the colour index and light curves so closely mimic each other as seen in Figure 4-7. The radial displacement has a lower order effect, and this is why it lags the light curve much more significantly than the colour index. Secondly, borrowing from the "squeeze theorem" of differential calculus, a curve which is itself the product of two curves will have its maximum at a point somewhere in between the maximum of its constituent curves, and so we necessarily have that the time of maximum brightness occurs between the times of maximum temperature and maximum radius. In general it occurs closer to the time of maximum temperature because that is the dominant factor. These simple facts *impose* the need for passband epoch lagging if indeed a colour index is representative of effective temperature and surface brightness, because it is the lag between passband curves which give rise to an index curve the maximum of which occurs at a time before either of the passbands. For stellar pulsation, with the added effect of a radial displacement curve and accounting for the squeeze theorem, this maximum must always occur before *any* of the passbands reach their maxima. And if each passband has its own time of maximum brightness, then following the discussion regarding Figure 4-7, we must unavoidably conclude that each passband will result in a different radius in the solution. At each passband, different amounts of skew will be needed from the radius term in order to converge the fitting routine, and these will manifest as different values of R_0. There is no

reason to assume that these are not the physically real geometric properties of the star. Indeed, the Baade-Wesselink analysis in the previous section did show a correspondence between passband and radius, and presently we will see the same for the Balona analysis.

A representative Balona fit is shown in the next figure. The input data were the same as in Figure 4-8. A Matlab program called "Balona.m" was written to perform the fit automatically, with the user supplying the relevant data in the input arguments of the program. The program also displays a live video of the fitting process as the Matlab subroutine (i.e. "fminunc") explores the parameter space of the fitting equation - it rather looks like a couple of tangled up worms wriggling their way around until they find a comfortable resting position as near to each other as possible.

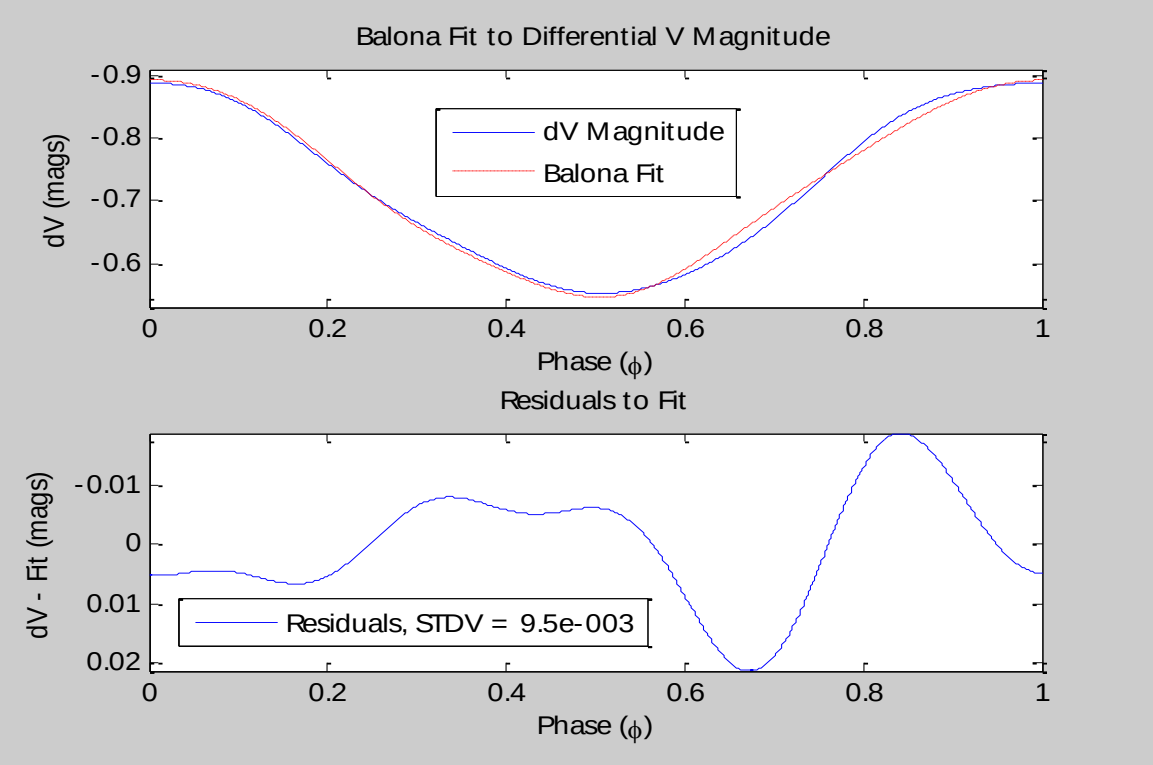

Figure 4-9: Balona fit of the mean colour index and radial displacement curves to the light curve.

In the above figure we see an increased deviation of the fit after about 0.5 phase. This is likely due to that region suffering from phase gaps in the photometric data, leading to a poor constraint and estimate for the colour index and passband curves in that area. The standard deviation of the residuals in the figure is typical of those for the other passbands, the mean deviation falling to within the fit tolerance (10^{-10} arbitrarily) specified when calling *fminunc*.

The Balona method uses the entire data set, unlike the Baade-Wesselink method where the solution points are restricted to an arbitrary number within a "safe" range of the possible solution space. Similarly however, although it is possible to calculate analytically the statistical errors on the fit parameters for each solution, because we are fitting Fourier curves of 1000 points the calculated errors still qualify as being arbitrary. Using 100 or 10,000 points give more and less error respectively, as any random statistical error always scales inversely with the square root of the number of data points; therefore, these errors are internal to the solution only. The Balona radius in each of the UBVRI passbands and the passband-averaged result are tabulated below in Table 4-2, and plotted in Figure 4-10. There is an obvious correlation between the Baade-Wesselink passband solutions (Figure 4-6) and the Balona solutions below, and this is discussed in the following section.

Filter	Radius (R_{Sun})	Stdv[61] (R_{Sun})
U	45.6	0.001
B	39.9	0.002
V	40.8	0.003
R	42.6	0.001
I	43.5	0.002
Mean	*42.5 ± 2.3*	-

Table 4-2: Balona Radii

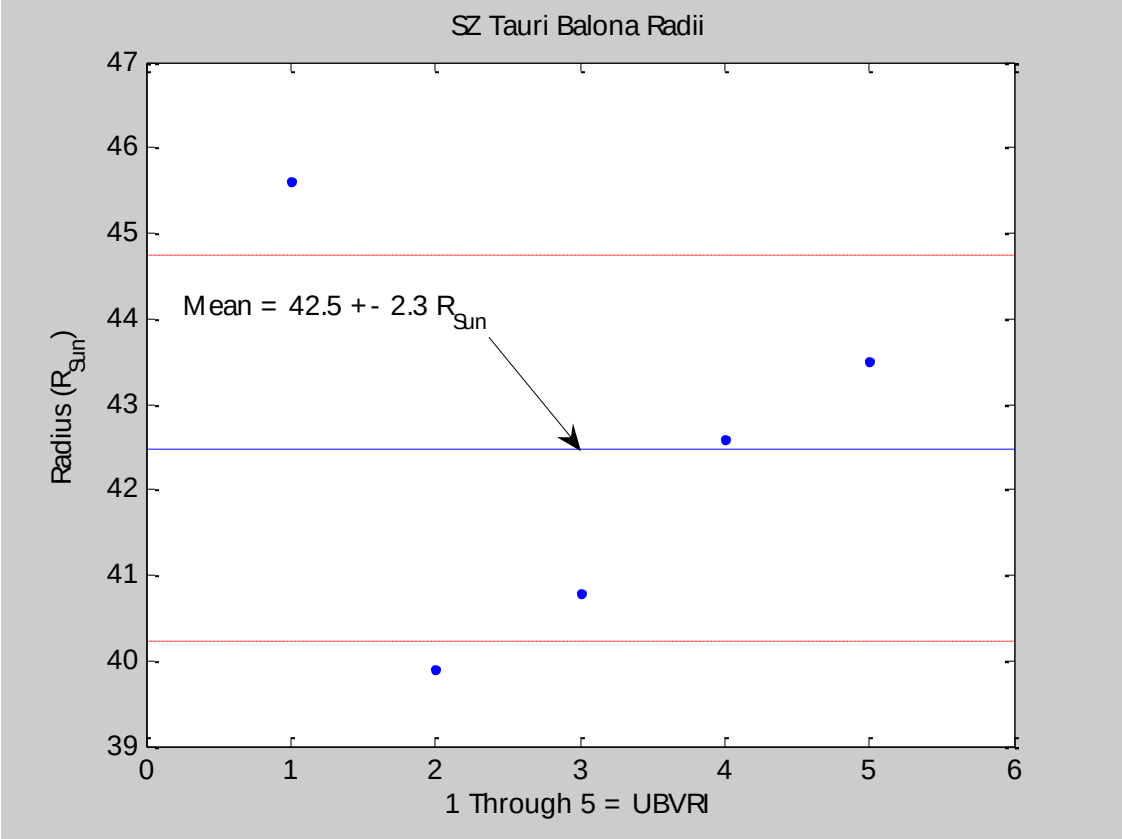

Figure 4-10: Balona radii.

[61] The errors on the 5 passband radius parameters are internal to the solution only.

4.3 Discussion of Results

The correlation between the two methods of solution is shown in the next figure. The Balona solutions are approximately seven percent larger than the Baade-Wesselink ones and have an offset of 1.4 solar radii, so that at 42.5 R_{Sun} the difference between the mean of the two solutions is 4.6 R_{Sun}, or close to ten percent.

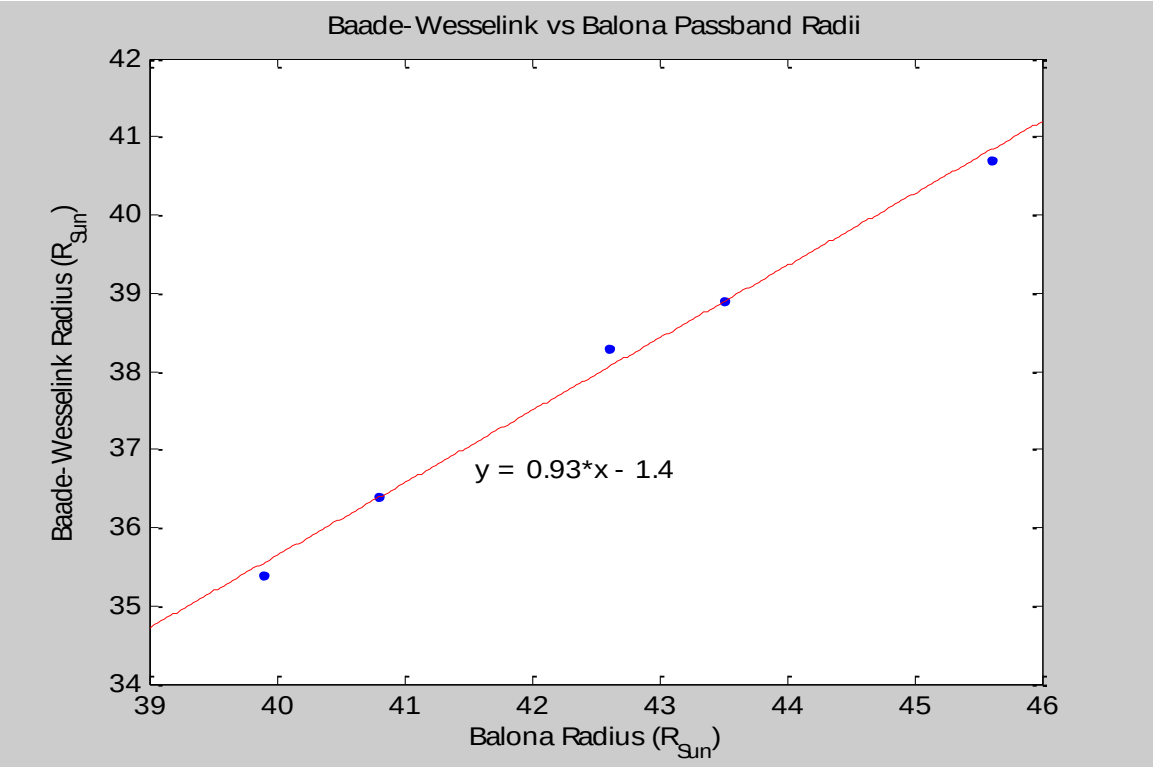

Figure 4-11: Baade-Wesselink vs. Balona radii.

It is not at all surprising that the two solution distributions mimic each other so well over the passbands, although there is a clear systematic difference between them. Following the development of the solutions in Chapter 2.2 it was clear that they were derived from the

same starting point (equation (2.2)), and indeed one can easily derive the Baade-Wesselink solution from the equation for the Balona method as a special case[62]. Recalling the Balona equation (4.2) (and (2.8)),

$$m(\varphi) = A \cdot CI(\varphi) + B - 5\log(R_0 + \delta R(\varphi)), \tag{4.3}$$

one simply needs to subtract this equation from itself at phases φ_1 and φ_2 where the respective colour indexes are equal, leaving only a difference in magnitude on the left and a logarithmic difference in radius on the right, all other terms cancelling. It is then quite a simple matter to solve for R_0, and this results in the Baade-Wesselink solution of equation (2.6). The two solutions are fundamentally identical – they are simply different treatments of the application of the method. The systematic difference that does exist between the two solutions can easily be attributed to the clear systematic difference between either's practical calculation; as we have seen, the Baade-Wesselink method requires the neglect of certain ranges of legitimate data, where equal colour indexes occur at too near of phase and at phases too near zero slope in the colour index, while the Balona method has no such restriction.

In any case, the Baade-Wesselink and Balona methods agree in their passband averaged mean radius to essentially the one sigma level, the upper one sigma limit of the BW solution being 40 R_{Sun} while the lower limit of the Balona solution is 40.2 R_{Sun}. In making this comparison, however, we realize that the Baade-Wesselink method is simply an alternative approximation to the more comprehensive Balona solution, and that fundamentally we are not extracting or comparing any unique information between the two

---

[62] Historically the Baade-Wesselink method was developed first.

solutions. Nevertheless, the mean and first moment of the Baade-Wesselink and Balona solutions is $R = 40.2 \pm 3.3\ R_{Sun}$, but we will use the Balona results for the radius found in this work, i.e., from Table 4-2:

$$\langle R \rangle_{SZ\ Tau} = 42.5 \pm 2.3\ R_{Sun}. \tag{4.4}$$

Eleven previous solutions for the radius are listed below in Table 4-3. The Balona solutions generally report larger radii than the others, however there is quite good agreement between solutions in most cases.

Reference	**Radius (R_{Sun})**	**Method**
Burki (1985)	36	Wesselink[63]
Gieren (1985)	34.2 ± 3	Barnes-Evans[64]
Sanewal & Rautela (1989)	37.8 ± 1.2	Baade-Wesselink[65]
Laney & Stobie (1995)	38.6 ± 1.2	Balona[65]
Gieren, et al. (1997)	V & V-R: 35.9 ± 2.8 K & K-J: 45.6 ± 4.0 V & V-K: 27.7 ± 0.5	Barnes-Evans[64]
Krockenberger et al. (1997)	$36.3 \pm {}^{8.3}_{5.8}$	Baade-Wesselink[65]
Ripepi et al. (1997)	44.8	CORS/Barnes-Evans[66]
Sachkov (1997)	43 ± 6	Balona[65]
Turner & Burke (2002)	34.8 ± 1.4	Baade-Wesselink[65]
Barnes, et al. (2003)	39.6 ± 6	Bayesian Barnes-Evans[66]
Postma (this work)	42.5 ± 2.3	Balona[65]
Average	38.2 ± 4.9	-

Table 4-3: Radius determinations for SZ Tau.

The radius determined in this work matches within experimental error the average of the other 11 values, and helps confirms the findings by Sachkov (1997) that the radius of a (low-amplitude) Cepheid can be used to determine its pulsation mode. Sachkov (*ibid.*) established two relations for the period-radius relationship, based on the segregation found

[63] As described in Burki & Benz Burki, G., & Benz, W. 1982, Astronomy and Astrophysics, 115, 30.
[64] Also known as the Surface Brightness Method.
[65] As described in this work.
[66] As described in referenced publication.

in his study of radius vs. period for 13 DCEPS Cepheids; the segregation could be explained if stars of the two groups pulsated in either the fundamental or the first-overtone mode, given that overtone pulsators will have a swollen radius for a given period. This study would then imply that not all DCEPS are overtone pulsators.

Using the mean temperature determined in Chapter 3.1.3, which was found to match well with that determined by Sanewal & Rautela (1989), and the radius from equation (4.4), the average luminosity of SZ Tau was computed to be

$$L_{SZ\ Tau} = 2138 \pm 235\ L_{Sun}$$
$$or \qquad (4.5)$$
$$\log \frac{L_{SZ\ Tau}}{L_{Sun}} = 3.33 \pm 0.05$$

SZ Tau is, expectedly, a class Ib supergiant with a mean spectral type of F7.5.

Chapter 5: Final Comments and Future Work

The passband epoch lagging phenomenon discovered in the data of this work was an unexpected result. Phase-lags of temperature to light, radius to light, and temperature to radius have been noted by various authors (Baker & Kippenhahn 1962; Berdnikov & Pastukhova 1995; Fernie & Hube 1967; Gieren 1982, 1985; Kukarkin 1975; Madore & Fernie 1980; Merengo, Karovska, & Sasselov 2004; Moffett 1989; Rosseland 1949; Ruoppo et al. 2004; Scarfe 1976; Simon 1984; Szabo, Buchler, & Bartee 2007). However, *passband* epoch lagging appears to have been largely over-looked, even over the century or so of filtered-light curve observation of Cepheid variables. Very high quality photometry and advanced reduction methods are required in order to see the phenomenon at all, and not a large percentage of published data may have been sufficiently precise.

Conceptual reasoning and explanations for epoch lagging have been discussed in previous Chapters, and now modeling the light and radius curve variations using simple co-sinusoidal oscillations lends confirmatory rationale. Let the effective temperature of a Cepheid, with the maximum of the temperature curve defining zero phase, be

$$T(\varphi) = T_0 + \delta T(\varphi) \tag{5.1}$$

and let the radius be

$$R(\varphi) = R_0 + \delta R(\varphi - \eta) \tag{5.2}$$

where φ is the phase (ranging between 0 and 1) and η is the lag of the radial maximum to that of the temperature (about 0.37 phase for SZ Tau). For each of the

$J_i = \{U;\ B;\ V;\ R;\ I\}$ Johnson passbands, we can approximate the stellar luminosity $L_i(\varphi)$ with Planck's black-body law such that

$$L_i(\varphi) = 4\pi R(\varphi)^2 \int_0^\infty \frac{2hc^2}{\lambda^5} \frac{1}{e^{\frac{hc}{\lambda kT(\varphi)}} - 1} \bullet J_i(\lambda)\ d\lambda \tag{5.3}$$

where $J_i(\lambda)$ is the transmission profile of the i'th passband (Moro & Munari 2000). On the magnitude scale we have

$$m_i(\varphi) = -2.5\log_{10}(L_i(\varphi)) + c_i \tag{5.4}$$

where c_i is a zero-point constant, which for the purposes here can be assumed equal to zero. Using sample physical values of SZ Tau for equations (5.1) and (5.2), we can approximate a general pulsation as

$$T(\varphi) = 6015 + \frac{537}{2} * \cos(2\pi\varphi) \tag{5.5}$$

and

$$R(\varphi) = (42.5 + \frac{1.8}{2}\cos(2\pi(\varphi - 0.37)))R_{Sun}. \tag{5.6}$$

First, it should be obvious that a constant surface area, thermally-varying object will produce light curves which are in complete phase with one another. This will likewise occur when a radial variation is added which is in phase with the temperature variation, i.e. when η is equal to zero. Colour index curves formed from these curves will also be in the same phase and will maximize at the same time as the light curves. However, if a radial variation is introduced which is *not* in phase with the temperature variation (as in equation (5.6), i.e. $\eta \neq 0$), the resulting light curves will show an epoch lag for the simple fact that the passband flux curves have unique amplitudes, and these combine uniquely with the radial variation to

produce luminosity curves each with (sequentially) unique times of maximum, as can be seen in Figure 5-1 below.

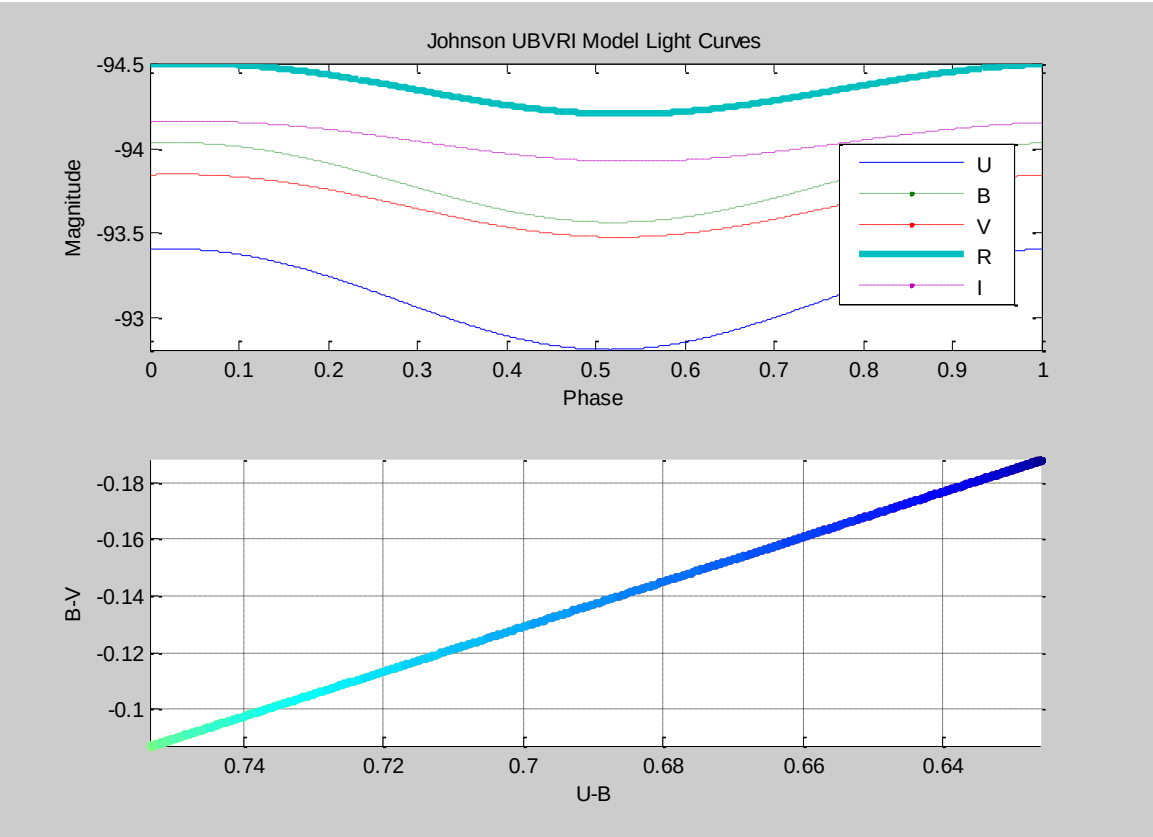

Figure 5-1: Johnson UBVRI light curve and colour-colour plot.

Not all the known properties of a Cepheid light curve are reproduced with this preliminary model, however. First, all the colour indices formed from this model maximize at the exact same time, i.e., at phase zero. Though the various colour indices from Chapter 3 were found to have different times of maximum, this may not be argued as a general property of Cepheids because it hasn't really been studied before. But second, and this is related to the first point, there is no colour-colour looping in the colour-colour plot of Figure 5-1. All this is simply because the radial term of equation (5.3), when inserted into

equation (5.4), gets subtracted out when forming the colour index because it has no passband dependence. However, colour-colour looping *is* a general property of Cepheid light curves (Diethelm 1983; Gieren 1982; Onnembo et al. 1985). So equation (5.6) can then be modified so that

$$R_i(\varphi) = (< R_i > + \frac{1.8}{2}\cos(2\pi(\varphi - 0.37)))R_{Sun} \tag{5.7}$$

where $<R_i>$ is the mean radius of the *i*'th passband. Computing new model light curves with passband-radius values taken from Table 4-2 results in Figure 5-2 below. In addition to each passband maximizing at a (sequentially) unique time the colour-colour plot now shows an open loop, indicating that the colour indices are no longer maximizing at the same time and so are no longer in phase with each-other. This highlights a potentially severe problem because proper separation of the temperature contribution from the light curve is so important when computing radii with either the Baade-Wesselink or Balona methods, and so puts into question which colour index is the appropriate one to use. This is ultimately why this author used the *mean* colour index curve in his solutions for the radii. In Gray (1994), Gray & Brown (2001), and Gray & Johanson (1991), it is shown that line-depth ratios of temperature-sensitive to temperature-insensitive lines can provide a precise index (order ~1K) on stellar effective-temperature variations. For a *given* star, line-depth ratio variations are completely independent of metallicity changes (because there are none), surface gravity variations (because line-broadening effects are divided out in the ratio), and most importantly the surface area, which *does* change and which as we have just seen *does* affect the standard colour indices. In addition to Gray (2007), where high-resolution spectroscopy was used to directly compute the radial velocity variations without the need of the '*p*'-factor, one

may produce an original observational methodology for separating the temperature and radial effects from the light curve, and ultimately for determining the radius using either the Baade-Wesselink or Balona approach.

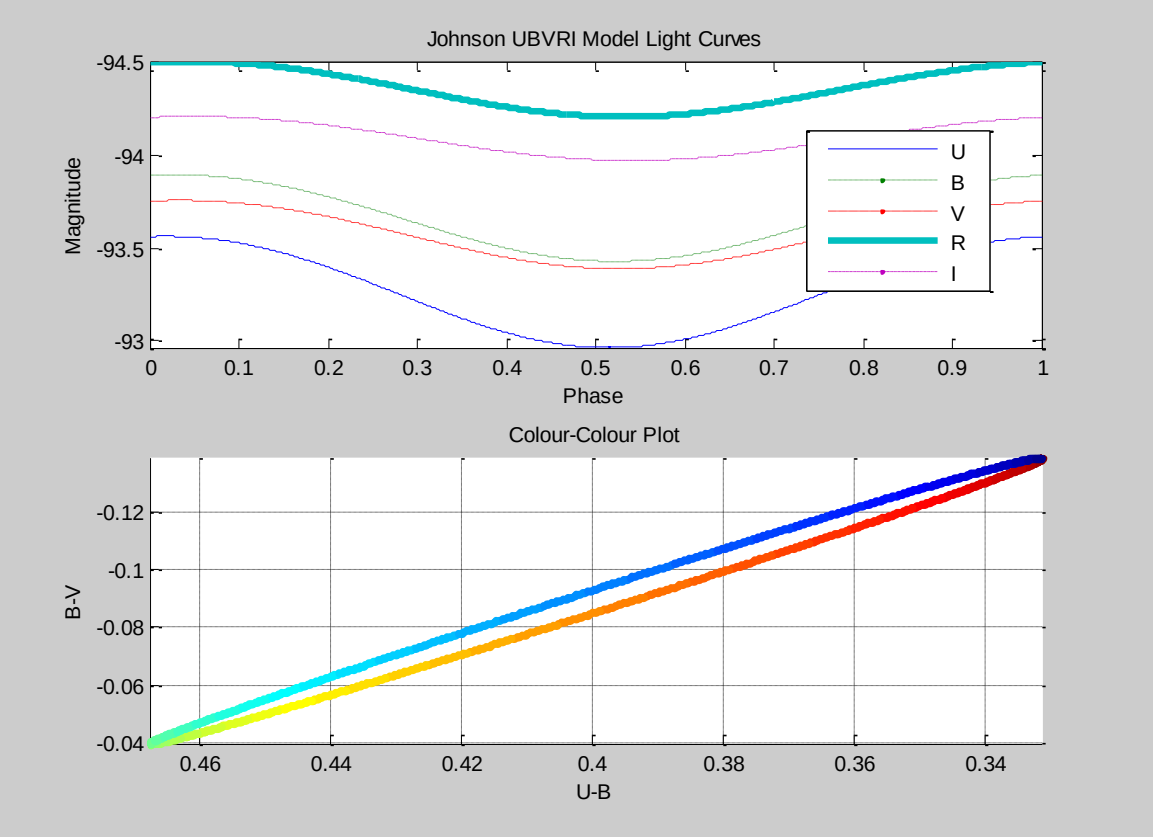

Figure 5-2: The colour-colour plot now shows an open loop, which is a general feature of Cepheid pulsation.

To completely reproduce all the qualitative properties of SZ Tau's variation, we must consider that the *U* passband shows a larger radius than any of the others, not quite fitting into the general sequential trend. In Table 3-5 we also saw that the *U* passband epoch occurred slightly later than the *B* passband, again not fitting the general sequential trend. The physical explanation for this may come from the Balmer discontinuity pushing the formation of the continuum around 3650 Å (the center of the Johnson *U* passband) to much

higher levels in the photosphere because of the very strong absorption on the short-wavelength side of that filter (Gray 1992, pp 160-163). We may thus consider that different passbands, being formed at distinct layers within the photosphere, may also have unique amplitudes of variation so that

$$R_i(\varphi) = (< R_i > + \frac{\delta R_i}{2} \cos(2\pi(\varphi - 0.37)))R_{Sun} \qquad (5.8).$$

If we make the supposition that higher passband radii undergo larger amplitudes of variation, so that $\delta R_i = \{2.2;\ 1.4;\ 1.6;\ 1.8;\ 2.0\}$, we qualitatively reproduce the observed properties of SZ Tau's oscillation: the colour-colour loop opens up significantly more, the passbands and colour indices have unique times of maximum, and the *U* passband maximizes after the *B* passband. This is shown in Figure 5-3 below – the phase-times of maximum for the UBVRI passbands are 0.023, 0.02, 0.029, 0.04. and 0.56, respectively.

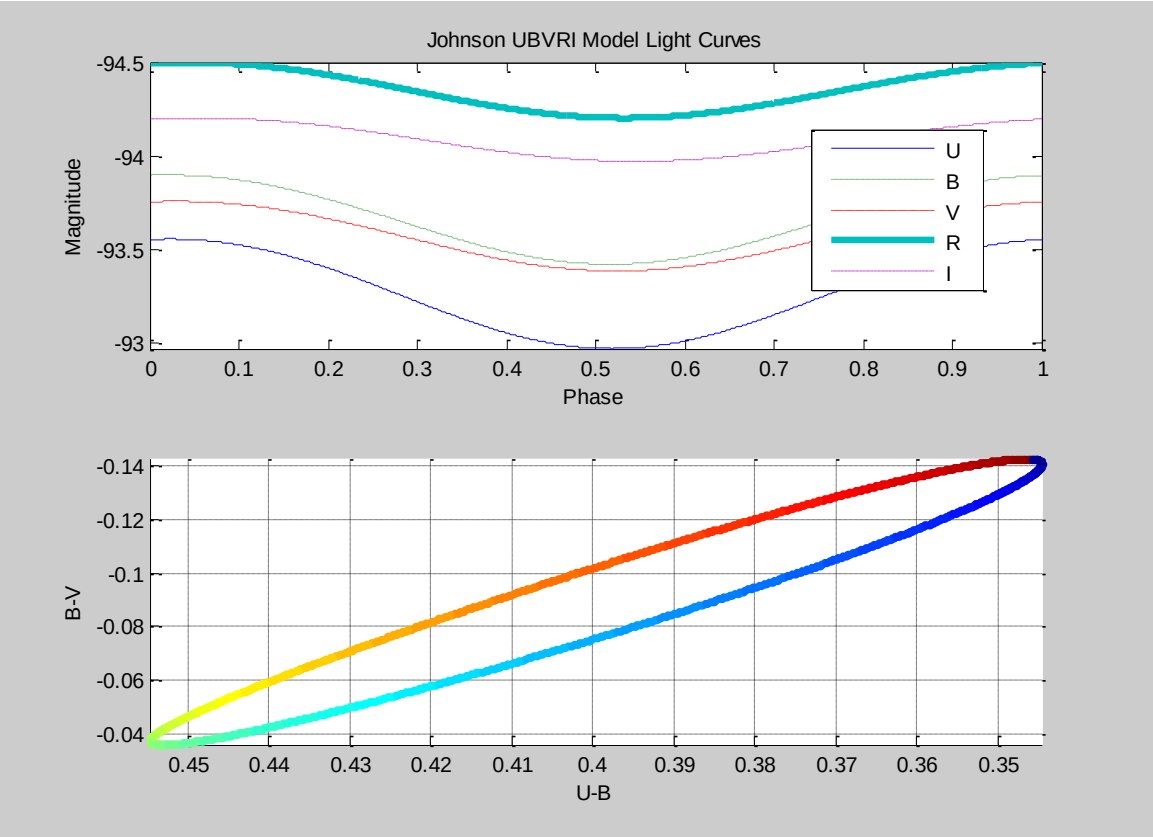

Figure 5-3: If each passband-layer of the photosphere has a unique amplitude of radial excursion, all known properties of SZ Tau's pulsation can be reproduced.

If we let the blackbody surface flux contribution of equation (5.3) be generally $f(\lambda, T(\varphi))$, we can write

$$F_i(T(\varphi)) = \int_0^{\infty} f(\lambda, T(\varphi)) \bullet J_i(\lambda) d\lambda \qquad (5.9).$$

This more general form would allow spectral-type phase-interpolated Kurucz (1979) stellar model atmospheres to be used for the surface flux contribution, and would more properly simulate the behaviour of the various stellar absorption feature variations as the Cepheid moves through spectral-types in the course of its pulsation. We can then model a light curve generally as

$$\begin{aligned} m_i(\varphi) &= -2.5\log_{10}(F_i(T(\varphi))) - 2.5\log_{10}(4\pi R_i(\varphi)^2) + c_i \\ &= -2.5\log_{10}(F_i(T_0 + \delta T(\varphi))) - 5\log_{10}(< R_i > + \delta R_i(\varphi - \eta_i)) + c_i \end{aligned} \tag{5.10}$$

once again letting the phase of maximum surface flux define the epoch, for simplicity. Because the driving force of the pulsation comes from a layer far below the photosphere, the pulsation will sequentially pass through each passband-layer as it propagates to the stellar surface, and so the phase-lag of radius to temperature should be passband dependent as well, i.e., $\eta = \eta_i$. Note that equation (5.9) (i.e., the first term in equation 5.10), as essentially a function of spectral type, is the linear colour index approximation of the Balona solution, i.e.

$$-2.5\log_{10}(F_i(T_0 + \delta T(\varphi))) \simeq A \cdot CI + B \tag{5.11}.$$

One may additionally consider that $f(\lambda, T(\varphi))$ will be dependent on the depth of formation as well, so that the spectral flux distribution in each passband is $f(\lambda, T_i(\varphi), R_i(\varphi))$. In the most general terms, the time of maximum light for each passband can be determined by

$$\begin{aligned} \frac{dm_i(\varphi)}{d\varphi} = 0 &= 2\frac{d\ln(R(\varphi))}{d\varphi} + \frac{d\ln(F_i(T(\varphi)))}{d\varphi} \\ 0 = \frac{2\, v_i(\varphi - \eta_i)}{< R_i > + \delta R(\varphi - \eta_i)} &+ \frac{d\ln(\int_0^\infty f(\lambda, T_i(\varphi), R_i(\varphi)) \bullet J_i(\lambda) d\lambda}{d\varphi} \end{aligned} \tag{5.12}$$

where $v_i(\varphi - \eta_i)$ is the radial velocity curve specific to each passband. Equation (5.12) can be solved numerically, and the passband dependencies of the various parameters are indicative of non-commensurate times of maxima for each passband-layer of the photosphere.

Epoch lagging gives the astronomer a method with which to peer into the third dimension of the stellar photosphere and provides for a more complete understanding of the structure of supergiant atmospheres. It also highlights several limiting factors in the current

methodology of determining Cepheid radii and ultimately the precision in the period-luminosity relationship. Separation of the surface flux contribution from the light curves directly, and significantly, affects the solution for the radius in the Baade-Wesselink and Balona methods. This has been under-appreciated to the point that some authors have mistakenly recommended that infra-red passbands should be used for the colour-index, reasoning those passbands are more sensitive to radial variations as opposed to temperature ones. Though this may be true, it convolutes the fundamental desire to use colour indices to represent the surface flux contribution and its variations. The best colour index to form would be one in which *one* passband is *highly* sensitive to temperature, with the other one being much less so; for example, U-I. But even if a truly accurate surface flux index can be formed when subtracting two passbands, one still has the result that each passband will show a different radius because each passband has a unique phase lag to that of the temperature, ultimately because each passband originates at a unique depth in the stellar photosphere. In this work, we have seen a variation of roughly 5 solar radii in the solutions between the U and I passbands, an "error" of roughly 10%. Whether or not this is physically accurate may be questioned, but ignoring passband epoch lagging does nothing to improve the current limit of ±10% in the period-luminosity relationship. Because there has been no standardization within astronomy of which passbands and which colour indices are to be used when solving for the radius, one can easily conjecture that the current limit in precision is at least partially due to the epoch lagging phenomenon and the physical properties of stellar photospheric structure it represents.

There are many observational programs which could be undertaken in order to further explore some of the phenomena discovered and theorized in this work. High time

resolution photometry over *entire* cycles, where the time between sequential observations is less than $1/100^{th}$ of the cycle, would be valuable for exploring the possibility of period variations between passbands on short time scales - this is not possible with the vast majority of existing data because most programs only observe at a frequency of less than one data-point per cycle. Such data, if sufficiently precise, would also allow accurate determinations of the phase lags between passbands and any variations therein. If a program were undertaken with a large number of Cepheids, one could also explore possible general correlations between epoch lag and radius, furthering our understanding of stellar atmospheric structure. High resolution spectroscopic observing programs would also be extremely beneficial. Modern techniques for determining temperature variations and pulsation velocities could be utilized for more accurate separation of those effects from the photometric light curves. Spectral line bisectors could be utilized for determining the amount of and variation in velocity spans between higher and lower layers of the photosphere during different phases in the pulsation, and these could be correlated with the passband epochs. Similarly, radial velocity profiles from long and short wavelength regions of the spectrum could be used for exploring passband-dependant pulsational displacement curves. Narrow-band and spectrophotometric work could also help to delineate the behaviour of the epoch lag with wavelength. And observation of Cepheids in eclipsing binary systems in various passbands could be used for directly determining the radius specific to each passband.

A deeper understanding of stellar photospheric structure, at least in regards to Cepheid pulsation, is clearly possible. And with the proper data with which to accomplish it,

would clearly improve (at least) the period-luminosity relationship. This is left to a future work.

REFERENCES

Alcock, C., et al. 1995, The Astronomical Journal, 109, 1654
Antonello, E., Poretti, E., & Reduzzi, L. 1990. in Astronomical Society of the Pacific Conference Series, Confrontation between Stellar Pulsation and Evolution, eds. C. Cacciari, & G. Clementini (Bologna, Italy), 616
Baade, W. 1926, Astronomische Nachrichten, 228, 359
Baker, N. 1966, Stellar Evolution (New York: Plenum Press)
Baker, N., & Kippenhahn, R. 1962, Zeitschrift fur Astrophysik, 54, 114
Balona, L. A. 1977, Monthly Notices of the Royal Astronomical Society, 178, 231
Barnes, T. G., Fernley, J. A., Frueh, M. L., Navas, J. G., Moffett, T. J., & Skillen, I. 1997, Publications of the Astronomical Society of the Pacific, 109, 645
Barnes, T. G., III; Moffett, Thomas J.; Slovak, Mark H. 1987, Astrophysical Journal Supplement Series 65, 307
Barnes, T. G., Jefferys, W. H., Berger, J. O., Mueller, P., Orr, K., & Rodriguez, R. 2003, The Astrophysical Journal, 592, 539
Becker, W., & Strohmeier, W. 1940, Zeitschrift fur Astrophysik, 19, 249
Belopolsky, A. 1894, Astronomische Nachrichten, 136, 281
Berdnikov, L. N., Ignatova, V. V., Pastukhova, E. N., & Turner, D. G. 1997, Astronomy Letters, 23, 177
Berdnikov, L. N., & Pastukhova, E. N. 1995, Astronomy Letters, 21, 369
Bersier, D., Burki, G., & Burnet, M. 1994a, Astronomy and Astrophysics Supplement Series, 108, 9
Bersier, D., Burki, G., Mayor, M., & Duquennoy, A. 1994b, Astronomy & Astrophysics Supplement Series, 108, 25
Bohm-Vitense, E. 1958, Zeitschrift fur Astrophysik, 46, 108
Bottlinger, K. F. 1928, Astronomische Nachrichten, 232, 3
Brunt, D. 1913, The Observatory, 36, 59
Burki, G. 1985. in IAU Colloquium 82 - Cepheids: Theory and Observations, Radius Determinations for Nine Short Period Cepheids, ed. B. F. Madore (Cambridge University Press), 34
Burki, G., & Benz, W. 1982, Astronomy and Astrophysics, 115, 30
Caccin, R., Onnembo, A., Russo, G., & Sollazzo, C. 1981, Astronomy and Astrophysics, 97, 104
Collmann, W. 1930, Astronomische Nachrichten, 238, 389
Cox, J. P. 1963, The Astrophysical Journal, 138, 487
---. 1980, Theory of Stellar Pulsation (Princeton: Princeton University Press)
---. 1985. in IAU Colloquium 82 - Cepheids: Theory and Observations, Theory of Cepheid Pulsation: Excitation Mechanisms, ed. B. F. Madore (Cambridge University Press)
Cox, J. P., Cox, A. N., Olsen, K. H., King, D. S., & Eilers, D. D. 1966, The Astrophysical Journal, 144, 1038
Diethelm, R. 1983, Astronomy and Astrophysics, 124, 108

Dupree, R. G. 1977, The Astrophysical Journal, 211, 509
Eddington, A. S. 1917, The Observatory, 40, 290
---. 1918, Monthly Notices of the Royal Astronomical Society, 79, 2
---. 1941a, Monthly Notices of the Royal Astronomical Society, 101, 177
---. 1941b, Monthly Notices of the Royal Astronomical Society, 101, 182
---. 1942, Monthly Notices of the Royal Astronomical Society, 102, 154
Efremov, Y. N. 1968, Peremen. Zvez., 16, 365
Eggen, O. J. 1950, Astrophysical Journal, 111, 65
---. 1951, Astrophysical Journal, 113, 367
Epstein, I. 1950, The Astrophysical Journal, 112, 6
Evans, N. R. 1985. in IAU Colloquium 82 - Cepheids: Theory and Observations, A Search for Cepheid Binaries using the CaII H and K Lines, ed. B. F. Madore (Cambridge University Press), 79
Fernie, J. D. 1985. in IAU Colloquium 82 - Cepheids: Theory and Observations, Historical Preface, ed. B. F. Madore (Cambridge University Press)
Fernie, J. D., & Hube, J. O. 1967, Publications of the Astronomical Society of the Pacific, 79, 467
Gautschy, A. 1987, Vistas in Astronomy, 30, 197
Gieren, W. P. 1982, Astrophysical Journal Supplement Series, 49, 1
---. 1985, Astronomy and Astrophysics, 148, 138
Gieren, W. P., Barnes, T. G., III, & Moffett, T. J. 1989, Astrophysical Journal, 342, 467
Gieren, W. P., Fouque, P., & Gomez, M. I. 1997, Astrophysical Journal, 488, 74
Goodricke, J. 1786, Philosophical Transactions of the Royal Society of London, 76, 48
Gray, D. F. 1992, The Observation and Analysis of Stellar Photospheres (Second Edition ed.: Cambridge University Press)
---. 1994, Publications of the Astronomical Society of the Pacific, 106, 1248
---. 2007, Publications of the Astronomical Society of the Pacific, 119, 398
Gray, D. F., & Brown, K. 2001, Publications of the Astronomical Society of the Pacific, 113, 723
Gray, D. F., & Johanson, H. L. 1991, Publications of the Astronomical Society of the Pacific, 103, 439
Hardie, R. H. 1962, in Stars and Stellar Systems, ed. W. A. Hiltner (Chicago: The University of Chicago Press), 178
Haynes, E. S. 1913, Lick Observatory Bulletin, 8, 85
Khopolov, P. N., et al. 1985, General Catalogue of Variable Stars (4 ed.; Moscow)
Kiss, L. L., & Vinko, J. 2000, Monthly Notices of the Royal Astronomical Society, 304, 420
Krockenberger, M., Sasselov, D. D., & Noyes, R. W. 1997, The Astrophysical Journal, 479, 875
Kukarkin, B. V. 1975, in IPST Astrophysics Library (Keter Publishing House Jerusalem Ltd.)
Kurucz, R. L. 1979, Astrophysical Journal Supplement Series, 40, 1
Landolt, A. U. 1983, The Astronomical Journal, 88
Laney, C. D., & Stobie, R. S. 1995, Monthly Notices of the Royal Astronomical Society, 274, 337
Laney, C. D. S., R. S. 1992, Astronomy and Astrophysics Supplement Series 93
Leavitt, H. S., & Pickering, E. C. 1912, Harvard College Observatory Circular, 173, 1

---. 1914, Harvard College Observatory Circular, 186, 1
Madore, B. F., & Fernie, J. D. 1980, Publications of the Astronomical Society of the Pacific, 92, 315
Melissinos, A. 1966, in Experiments in Modern Physics (New York: Academic Press Inc.), 438
Merengo, M., Karovska, M., & Sasselov, D. D. 2004, The Astrophysical Journal, 603, 285
Milone, E. F. 1967, in PhD Thesis (New Haven: Yale University Observatory)
---. 1970, Commission 27 of the IAU Information Bulletin on Variable Stars, 482, 1
Milone, E. F., Wilson, W. J. F., & Volk, K. 1999, The Astronomical Journal, 118, 3016
Moffett, T. J. 1989. in IAU Colloquium 111 - The Use of Pulsating Stars in Fundamental Problems of Astronomy, The Baade-Wesselink Technique, ed. E. G. Schmidt (Cambridge University Press)
Moffett, T. J., & Barnes, T. G. 1980, The Astrophysical Journal Supplement Series, 44, 427
Moro, D., & Munari, U. 2000, Astronomy & Astrophysics Supplement Series, 147, 361
Onnembo, A., Buonaura, B., Caccin, B., Russo, G., & Sollazzo, C. 1985, Astronomy and Astrophysics, 152, 349
Platais, I., & Mandushev, G. 1993, Journal of the American Association of Variable Star Observers, 22, 110
Ripepi, V., Barone, F., Milano, L., & Russo, G. 1997, Astronomy and Astrophysics, 318, 797
Robinson, L. V. 1929, Harvard College Observatory Bulletin, 871
---. 1930a, Harvard College Observatory Bulletin, 876, 18
---. 1930b, Popular Astronomy, 38, 407
Rosseland, S. 1949, in The International Series of Monographs on Physics, eds. R. H. Fowler, P. Kapitza, N. F. Mott, & E. C. Bullard (Oxford University Press)
Ruoppo, A., Ripepi, V., Marconi, M., & Russo, G. 2004, Astronomy and Astrophysics, 422, 253
Sabbey, C. N., Sasselov, D. D., Fieldus, M. S., Lester, J. B., Venn, K. A., & Butler, R. P. 1995, The Astrophysical Journal, 446, 250
Sachkov, M. E. 1997, Commissions 27 & 42 of the IAU Information Bulletin on Variable Stars, 4522
Sanewal, B. B., & Rautela, B. S. 1989, Astrophysics and Space Science, 151, 209
Scarfe, C. D. 1976, The Astrophysical Journal, 209, 141
Schmidt, E. G. 1974, Monthly Notices of the Royal Astronomical Society, 167, 613
Schwarzschild, K. 1910, Astronomische Nachrichten, 185, 133
---. 1911, Astronomische Nachrichten, 189, 345
Shapley, H. 1913, Astronomische Nachrichten, 194, 353
---. 1914, The Astrophysical Journal, 40, 448
---. 1916, The Astrophysical Journal, 44, 273
Simon, N. R. 1984, Astrophysical Journal, 284, 278
Szabados, L. 1977, Communications from the Konkoly Observatory, 7, 5, 1
---. 1985. in IAU Colloquium 82 - Cepheids: Theory and Observations, Duplicity Among the Cepheids in the Northern Hemisphere, ed. B. F. Madore (Cambridge University Press), 75
---. 1991, Communications from the Konkoly Observatory, 11, 3, 123
Szabo, R., Buchler, R., & Bartee, J. 2007, The Astrophysical Journal, 667, 1150

Trammell, S. R. 1987, Journal of the American Association of Variable Star Observers, 16, 104
Turner, D. G. 1992, The Astronomical Journal, 104
Turner, D. G., & Burke, J. F. 2002, The Astronomical Journal, 124, 2931
Turner, D. G., Latif, M. A. S. A., & Berdnikov, L. N. 2006, Publications of the Astronomical Society of the Pacific, 118, 410
van Hoof, A. 1943, Ciel et Terre, 59, 369
Wamsteker, W. 1972, Information Bulletin on Variable Stars, 690
Wesselink, A. F. 1946a, Bulletin of the Astronomical Institutes of the Netherlands, 10, 88
---. 1946b, Bulletin of the Astronomical Institutes of the Netherlands, 10, 91
---. 1946c, Bulletin of the Astronomical Institutes of the Netherlands, 10, 83
---. 1947, Bulletin of the Astronomical Institutes of the Netherlands, 10, 256
Wilson, T. D., Carter, M. W., Barnes, T. G., Citters, v., Wayne, G., & Moffett, T. J. 1989, Astrophysical Journal Supplement Series 69, 951
Young, A. T. 1994, Applied Optics, 33, 1108
Zhevakin, S. A. 1953, Astronomicheskii Zhurnal, 30, 161
---. 1963, Annual Review of Astronomy and Astrophysics, 1, 367

Appendix A: Heliocentric Julian Day and Radial Velocity Corrections

The following is a Matlab m-file script which can be used to convert geocentric Julian Days to heliocentric ones, in order to standardize measurement timings to the common frame of reference of the Sun. It is assumed the user can convert local times of measurement to Julian times, if need be. Also computed is the associated radial velocity correction, used to convert a geocentrically measured radial velocity to a heliocentric one, and the airmass. The code was developed with reference to the 2005 Astronomical Almanac. For those unfamiliar with the Matlab data analysis language, comment lines are indicated by the '%' symbol. The code begins immediately:

```
function result = HJDC(JD,lat,long,ra,dec)

% Usage:  answer = HJDC(JD,lat,long,ra,dec);
% Result is returned in arbitrary "answer" variable as a nx3 row-major matrix, where
% n is number of JD input values.  1st column is Heliocentric Julian Day
% corrections, 2nd column is heliocentric radial velocity corrections, 3rd column is airmass
% Input:
% JD  = full Geocentric Julian Day      day.day
% lat = latitude of observation         deg.deg
% long = west longitude of observation  deg.deg
% RA = right ascension of target        hours.hr
% dec = declination of target           deg.deg

%DEFINITIONS
vrot_eq = 465.1;
% earth equatorial rotational linear velocity in m/s, based on spherical earth using quadratic-
% mean (polar-equatorial) radius; can be improved to take into account non-sphericity and
% geographical elevations, but these are 2nd or 3rd order corrections at best.
au = 1.49597870e11;
% astronomical unit (m)
cs = 173.14463348;
```

```
% speed of light (au/d)

% BEGINNING OF COMPUTATIONS
L = long/15;
% west longitude of observatory in hours
GMST = rem(18.697374558 + 24.06570982441908*(JD - 2451545.0),24);
% Greenwich Mean Sidereal Time at JD
LST = GMST - L;
% Local Sidereal Time at JD and longitude
ha = LST - ra;
%local hour angle of target
ha = ha*pi/12;
lat = lat*pi/180;
ra = ra*pi/12;
dec = dec*pi/180;
alt = asin(sin(lat).*sin(dec)+cos(lat).*cos(dec).*cos(ha));
zt = (pi/2 - alt); zt(zt > pi/2) = NaN;
% true zenith angle, don't care about stuff below horizon

A = ( 1.002432*cos(zt).^2 + 0.148386*cos(zt) + 0.0096467 ) ./ (cos(zt).^3 + ...
0.149864*cos(zt).^2 + 0.0102963*cos(zt) + 0.000303978);
% Airmass of target: Young, A. T. 1994. Air mass and refraction. Applied
% Optics. 33:1108–1110.

n = JD-2451545.0;
% exact decimal day number from J2000.0 UT 12hr
g = rem((357.528 + .9856003.*n).*pi/180,2.*pi);
% mean anomaly, in radians, at day number n
L = rem((280.46 + .9856474.*n).*pi/180,2.*pi);
% mean longitude, in radians, at n
lam = L + 1.915.*pi/180.*sin(g) + .020.*pi/180.*sin(2.*g);
% ecliptic longitude, in radians, at n
eps = 23.439.*pi/180 - .0000004.*pi/180.*n;
% ecliptic obliquity, in radians, at n
R = 1.00014 - 0.01671.*cos(g) - 0.00014.*cos(2.*g);
% distance of earth from sun in au's at JD
X = -R.*cos(lam);
Y = -R.*cos(eps).*sin(lam);
Z = -R.*sin(eps).*sin(lam);
% rectangular coordinates of earth wrt solar system barycenter referred to equinox and
%equator of J2000.0, in au's
Xdot =  .0172.*sin(lam);
Ydot = -.0158.*cos(lam);
Zdot = -.0068.*cos(lam);
% first deriv's of XYZ above, wrt time in days (au/d).  Note:  deriv's of XYZ w d/dt eps ~0
```

```
rv_rot = cos(lat).*cos(dec).*sin(ha).*vrot_eq;
% rv in direction of target due to earth's rotational motion, +ve away, m/s
rv_orb = -Xdot.*cos(ra).*cos(dec) - Ydot.*sin(ra).*cos(dec) - Zdot.*sin(dec);
% rv due to earth's orbital motion, +ve away au/d
rv_orb = rv_orb.*au/86400;      %convert to m/s
RVC = rv_rot + rv_orb;
RVC = round(RVC.*10)/10;  %rounded to 1 decimal place = 0.1 m/s.
% Radial Velocity due to earth's rotation and orbital motion referred to barycenter, in
%direction of target, +ve away.

BJDC= 1/cs.*(X.*cos(ra).*cos(dec) + Y.*sin(ra).*cos(dec) + Z.*sin(dec));
% Barycentric Julian Day Correction.  ADD this to geocentric input JD
% Otherwise known as Heliocentric JD (HJD) but there is ambiguity here.
% Difference between HJD and BJD << BJDC  (~1s/~5min) in almost all cases, so only
% important for very-high precision timing

result = [BJDC(:) RVC(:) A(:)];
```

Appendix B: Listing of the Photometric Data

Elements for the phase calculations: Period = 3.1488d, $Epoch_V$ = HJD 2453316.5166. HJD's below are HJD – 2453316.

HJD U	Phase	dU	HJD B	Phase	dB	HJD V	Phase	dV	HJD R	Phase	dR	HJD I	Phase	dI
0.7207	0.0648	-0.2019	0.7211	0.0649	-0.6228	0.7277	0.0670	-0.8708	0.7218	0.0652	-1.0439	0.7285	0.0673	-1.2281
0.7209	0.0649	-0.1982	0.7212	0.0650	-0.6363	0.7279	0.0671	-0.8859	0.7281	0.0672	-1.0353	0.7287	0.0673	-1.2251
0.7269	0.0668	-0.2016	0.7274	0.0669	-0.6223	0.7598	0.0772	-0.8764	0.7283	0.0672	-1.0328	0.7606	0.0775	-1.2210
0.7271	0.0668	-0.2001	0.7275	0.0670	-0.6121	0.7600	0.0773	-0.8754	0.7602	0.0773	-1.0368	0.7608	0.0775	-1.2222
0.7590	0.0770	-0.1842	0.7594	0.0771	-0.6198	0.7705	0.0806	-0.8746	0.7604	0.0774	-1.0423	0.7713	0.0809	-1.2243
0.7592	0.0770	-0.1850	0.7596	0.0772	-0.6178	0.7707	0.0807	-0.8754	0.7709	0.0808	-1.0254	0.7715	0.0809	-1.2271
0.7698	0.0804	-0.1819	0.7701	0.0805	-0.6165	0.7804	0.0838	-0.8631	0.7711	0.0808	-1.0324	0.7813	0.0840	-1.2006
0.7699	0.0804	-0.1781	0.7703	0.0806	-0.6157	0.7806	0.0838	-0.8674	0.7808	0.0839	-1.0125	0.7814	0.0841	-1.2004
0.7797	0.0835	-0.1735	0.7801	0.0837	-0.6147	0.7949	0.0884	-0.8699	0.7810	0.0840	-1.0100	0.7956	0.0886	-1.2157
0.7942	0.0881	-0.1652	0.7802	0.0837	-0.6176	0.7950	0.0884	-0.8685	0.7952	0.0885	-1.0161	0.7958	0.0887	-1.2153
0.7943	0.0882	-0.1719	0.7945	0.0882	-0.6034	0.8022	0.0907	-0.8692	0.7954	0.0885	-1.0170	0.8029	0.0909	-1.2177
0.8014	0.0904	-0.1711	0.7947	0.0883	-0.6012	0.8024	0.0908	-0.8669	0.8026	0.0908	-1.0283	0.8031	0.0910	-1.2228
0.8015	0.0905	-0.1654	0.8017	0.0905	-0.6111	0.8136	0.0943	-0.8623	0.8028	0.0909	-1.0221	0.8143	0.0945	-1.2126
0.8129	0.0941	-0.1616	0.8019	0.0906	-0.6098	0.8138	0.0944	-0.8642	0.8139	0.0944	-1.0147	0.8144	0.0946	-1.2072
0.8131	0.0941	-0.1629	0.8020	0.0906	-0.6121	0.8205	0.0965	-0.8671	0.8209	0.0966	-1.0169	0.8212	0.0967	-1.2210
0.8198	0.0963	-0.1607	0.8132	0.0942	-0.6007	0.8207	0.0966	-0.8619	0.8211	0.0967	-1.0211	0.8214	0.0968	-1.2189
0.8200	0.0963	-0.1609	0.8134	0.0942	-0.6041	0.8320	0.1001	-0.8541	0.8323	0.1002	-1.0152	0.8326	0.1004	-1.2103

0.8312	0.0999	-0.1610	0.8202	0.0964	-0.6055	0.8321	0.1002	-0.8553	0.8325	0.1003	-1.0168	0.8328	0.1004	-1.2115
0.8314	0.1000	-0.1535	0.8316	0.1000	-0.5946	0.8433	0.1037	-0.8467	0.8436	0.1038	-1.0015	0.8440	0.1040	-1.1909
0.8425	0.1035	-0.1570	0.8318	0.1001	-0.5949	0.8434	0.1038	-0.8428	0.8438	0.1039	-0.9996	0.8441	0.1040	-1.1894
0.8427	0.1036	-0.1465	0.8429	0.1036	-0.5869	0.8615	0.1095	-0.8524	0.8619	0.1096	-1.0059	0.8622	0.1097	-1.1985
0.8606	0.1092	-0.1390	0.8431	0.1037	-0.5877	0.8617	0.1096	-0.8485	0.8620	0.1097	-1.0059	0.8624	0.1098	-1.1979
0.8608	0.1093	-0.1355	0.8610	0.1094	-0.5835	0.8797	0.1153	-0.8536	0.8801	0.1154	-0.9959	0.8690	0.1119	-1.1749
0.8675	0.1114	-0.1199	0.8612	0.1094	-0.5853	0.8799	0.1154	-0.8583	0.8803	0.1155	-0.9902	0.8692	0.1120	-1.1755
0.8677	0.1115	-0.1221	0.8794	0.1152	-0.5869	0.9264	0.1301	-0.8117	0.9266	0.1302	-0.9790	0.8805	0.1156	-1.1894
0.8790	0.1151	-0.1233	0.8796	0.1153	-0.5886	0.9338	0.1325	-0.8237	0.9267	0.1302	-0.9746	0.8807	0.1156	-1.1828
0.8792	0.1151	-0.1243	0.8869	0.1176	-0.5615	0.9340	0.1325	-0.8239	0.9342	0.1326	-0.9864	0.8879	0.1179	-1.1797
0.8865	0.1175	-0.1216	0.8870	0.1176	-0.5602	0.9460	0.1364	-0.8351	0.9343	0.1327	-0.9856	0.8881	0.1180	-1.1873
0.8867	0.1175	-0.1141	0.9259	0.1300	-0.5475	0.9461	0.1364	-0.8288	0.9463	0.1365	-0.9994	0.8883	0.1180	-1.1784
0.9255	0.1299	-0.1006	0.9260	0.1300	-0.5458	0.9648	0.1423	-0.8111	0.9465	0.1365	-0.9990	0.9269	0.1303	-1.1775
0.9257	0.1299	-0.1004	0.9335	0.1324	-0.5480	0.9650	0.1424	-0.8127	0.9531	0.1386	-0.9636	0.9271	0.1304	-1.1804
0.9331	0.1323	-0.0978	0.9336	0.1324	-0.5454	0.9724	0.1448	-0.8197	0.9533	0.1387	-0.9618	0.9345	0.1327	-1.1863
0.9333	0.1323	-0.0983	0.9456	0.1362	-0.5564	0.9726	0.1448	-0.8202	0.9652	0.1424	-0.9786	0.9347	0.1328	-1.1838
0.9453	0.1361	-0.1077	0.9458	0.1363	-0.5533	0.9954	0.1520	-0.8035	0.9653	0.1425	-0.9820	0.9467	0.1366	-1.1981
0.9455	0.1362	-0.0986	0.9524	0.1384	-0.5425	0.9956	0.1521	-0.8101	0.9655	0.1426	-0.9806	0.9468	0.1366	-1.1962
0.9521	0.1383	-0.0913	0.9526	0.1384	-0.5295	1.0021	0.1542	-0.7976	0.9728	0.1449	-0.9903	0.9535	0.1387	-1.1738
0.9522	0.1383	-0.0907	0.9643	0.1422	-0.5423	1.0148	0.1582	-0.8170	0.9729	0.1449	-0.9925	0.9537	0.1388	-1.1713
0.9640	0.1421	-0.0778	0.9645	0.1422	-0.5451	1.0150	0.1583	-0.8170	0.9957	0.1522	-0.9750	0.9657	0.1426	-1.1805
0.9641	0.1421	-0.0832	0.9646	0.1423	-0.5358	1.0222	0.1606	-0.8085	0.9959	0.1522	-0.9766	0.9659	0.1427	-1.1789
0.9718	0.1445	-0.0898	0.9721	0.1446	-0.5377	1.0223	0.1606	-0.8071	1.0025	0.1543	-0.9676	0.9731	0.1450	-1.1930
0.9719	0.1446	-0.0795	0.9722	0.1447	-0.5390	3.7220	0.0179	-0.8790	1.0152	0.1583	-0.9749	0.9733	0.1450	-1.1930
0.9947	0.1518	-0.0678	0.9951	0.1519	-0.5236	3.7279	0.0198	-0.8918	3.7217	0.0179	-1.0255	0.9961	0.1523	-1.1816
0.9949	0.1519	-0.0796	1.0016	0.1540	-0.5264	3.7291	0.0202	-0.8798	3.7277	0.0198	-1.0367	0.9962	0.1523	-1.1799

1.0013	0.1539	-0.0758	1.0018	0.1541	-0.5095	3.7355	0.0222	-0.8802	3.7293	0.0203	-1.0300	1.0028	0.1544	-1.1698
1.0015	0.1540	-0.0754	1.0020	0.1541	-0.5046	3.7405	0.0238	-0.8899	3.7353	0.0222	-1.0281	1.0029	0.1544	-1.1770
1.0141	0.1580	-0.0666	1.0145	0.1581	-0.5319	3.7415	0.0241	-0.8811	3.7403	0.0238	-1.0376	1.0155	0.1584	-1.1821
1.0143	0.1580	-0.0622	1.0146	0.1582	-0.5276	3.7524	0.0276	-0.8819	3.7416	0.0242	-1.0242	1.0157	0.1585	-1.1814
1.0215	0.1603	-0.0529	1.0219	0.1605	-0.5244	3.7533	0.0279	-0.8806	3.7522	0.0276	-1.0311	1.0229	0.1608	-1.1923
1.0217	0.1604	-0.0547	1.0220	0.1605	-0.5163	3.7663	0.0320	-0.8800	3.7535	0.0280	-1.0289	1.0230	0.1608	-1.1971
3.7226	0.0181	-0.2377	3.7222	0.0180	-0.6468	3.8072	0.0450	-0.8916	3.7666	0.0321	-1.0191	3.7215	0.0178	-1.2218
3.7283	0.0200	-0.2404	3.7228	0.0182	-0.6371	3.8073	0.0451	-0.8914	3.8143	0.0473	-1.0467	3.7275	0.0197	-1.2187
3.7287	0.0201	-0.2420	3.7281	0.0199	-0.6528	3.8139	0.0471	-0.8886	3.8144	0.0473	-1.0470	3.7295	0.0203	-1.2102
3.7359	0.0224	-0.2387	3.7289	0.0201	-0.6454	3.8140	0.0472	-0.8908	3.8314	0.0527	-1.0253	3.7351	0.0221	-1.2014
3.7361	0.0224	-0.2177	3.7357	0.0223	-0.6434	3.8310	0.0526	-0.8766	3.8316	0.0528	-1.0354	3.7401	0.0237	-1.2177
3.7409	0.0240	-0.2306	3.7407	0.0239	-0.6505	3.8312	0.0526	-0.8822	3.8407	0.0557	-1.0292	3.7419	0.0243	-1.2088
3.7411	0.0240	-0.2293	3.7413	0.0241	-0.6511	3.8403	0.0555	-0.8813	3.8408	0.0557	-1.0320	3.7520	0.0275	-1.2170
3.7528	0.0277	-0.2288	3.7526	0.0277	-0.6462	3.8405	0.0556	-0.8838	3.8455	0.0572	-1.0340	3.7537	0.0280	-1.2130
3.7530	0.0278	-0.2211	3.7531	0.0278	-0.6443	3.8450	0.0570	-0.8823	3.8496	0.0585	-1.0296	3.7668	0.0322	-1.2105
3.7660	0.0319	-0.2133	3.7662	0.0320	-0.6440	3.8492	0.0584	-0.8789	3.8498	0.0585	-1.0251	3.8318	0.0528	-1.2226
3.7670	0.0323	-0.2181	3.7672	0.0323	-0.6340	3.8494	0.0584	-0.8729	4.0138	0.1106	-1.0055	3.8320	0.0529	-1.2238
3.8064	0.0448	-0.2019	3.8068	0.0449	-0.6359	4.0134	0.1105	-0.8489	4.0139	0.1107	-1.0037	3.8411	0.0558	-1.2151
3.8066	0.0448	-0.2049	3.8070	0.0449	-0.6372	4.0135	0.1106	-0.8487	4.0190	0.1123	-1.0068	3.8412	0.0558	-1.2140
3.8131	0.0469	-0.2000	3.8135	0.0470	-0.6425	4.0186	0.1121	-0.8530	4.0192	0.1123	-1.0085	3.8456	0.0572	-1.2222
3.8132	0.0469	-0.2022	3.8137	0.0471	-0.6451	4.0187	0.1122	-0.8488	4.6875	0.3246	-0.8532	3.8458	0.0573	-1.2257
3.8302	0.0523	-0.2041	3.8306	0.0525	-0.6160	4.0231	0.1136	-0.8495	4.6877	0.3246	-0.8421	4.0141	0.1107	-1.1990
3.8304	0.0524	-0.2033	3.8308	0.0525	-0.6236	4.0233	0.1137	-0.8460	4.6922	0.3261	-0.8424	4.0143	0.1108	-1.1991
3.8395	0.0553	-0.1990	3.8399	0.0554	-0.6303	4.0281	0.1152	-0.8419	4.6923	0.3261	-0.8430	4.0194	0.1124	-1.1988
3.8397	0.0553	-0.1978	3.8401	0.0555	-0.6380	4.6872	0.3245	-0.6397	4.7060	0.3305	-0.8496	4.0196	0.1125	-1.1844
3.8442	0.0568	-0.1933	3.8446	0.0569	-0.6374	4.6873	0.3245	-0.6438	4.7061	0.3305	-0.8382	4.0239	0.1138	-1.2130

3.8444	0.0568	-0.1921	3.8447	0.0569	-0.6336	4.6918	0.3260	-0.6578	4.7108	0.3320	-0.8372	4.0240	0.1139	-1.2129
3.8484	0.0581	-0.1825	3.8488	0.0582	-0.6339	4.6920	0.3260	-0.6594	4.7109	0.3320	-0.8405	4.6879	0.3247	-1.0803
4.0126	0.1103	-0.1533	3.8490	0.0583	-0.6242	4.7051	0.3302	-0.6292	4.7238	0.3361	-0.8446	4.6880	0.3248	-1.0826
4.0178	0.1119	-0.1412	4.0130	0.1104	-0.5778	4.7058	0.3304	-0.6474	4.7310	0.3384	-0.8415	4.6925	0.3262	-1.0752
4.0180	0.1120	-0.1381	4.0132	0.1104	-0.5814	4.7102	0.3318	-0.6408	4.7311	0.3384	-0.8409	4.6927	0.3262	-1.0940
4.0224	0.1134	-0.1467	4.0182	0.1120	-0.5827	4.7106	0.3319	-0.6360	4.7366	0.3402	-0.8385	4.7063	0.3306	-1.0881
4.0226	0.1134	-0.1439	4.0184	0.1121	-0.5839	4.7234	0.3360	-0.6379	4.7488	0.3441	-0.8354	4.7065	0.3306	-1.0869
4.0273	0.1149	-0.1326	4.0228	0.1135	-0.5788	4.7236	0.3361	-0.6394	4.7490	0.3441	-0.8209	4.7111	0.3321	-1.0941
4.0275	0.1150	-0.1222	4.0229	0.1135	-0.5799	4.7306	0.3383	-0.6369	4.7538	0.3457	-0.8399	4.7113	0.3321	-1.0901
4.6865	0.3243	0.2418	4.0277	0.1151	-0.5729	4.7308	0.3383	-0.6402	4.7656	0.3494	-0.8366	4.7315	0.3386	-1.0720
4.6912	0.3258	0.2302	4.0279	0.1151	-0.5669	4.7362	0.3401	-0.6345	4.7657	0.3494	-0.8380	4.7316	0.3386	-1.0726
4.6913	0.3258	0.2391	4.6870	0.3244	-0.2572	4.7364	0.3401	-0.6376	4.7825	0.3548	-0.8260	4.7371	0.3403	-1.0736
4.7044	0.3300	0.2422	4.6915	0.3259	-0.2754	4.7485	0.3440	-0.6224	4.7826	0.3548	-0.8234	4.7373	0.3404	-1.0750
4.7046	0.3300	0.2596	4.6917	0.3259	-0.2701	4.7487	0.3440	-0.6319	4.7893	0.3569	-0.8263	4.7494	0.3442	-1.0650
4.7096	0.3316	0.2427	4.7048	0.3301	-0.2594	4.7534	0.3455	-0.6299	4.7895	0.3570	-0.8213	4.7495	0.3443	-1.0630
4.7097	0.3316	0.2441	4.7099	0.3317	-0.2714	4.7536	0.3456	-0.6299	4.8285	0.3694	-0.8222	4.7543	0.3458	-1.0710
4.7223	0.3356	0.2521	4.7101	0.3317	-0.2780	4.7652	0.3493	-0.6298	4.8286	0.3694	-0.8215	4.7545	0.3459	-1.0747
4.7225	0.3357	0.2439	4.7228	0.3358	-0.2544	4.7654	0.3493	-0.6306	4.8352	0.3715	-0.8162	4.7660	0.3495	-1.0619
4.7296	0.3380	0.2589	4.7300	0.3381	-0.2552	4.7821	0.3546	-0.6212	4.8354	0.3716	-0.8063	4.7662	0.3496	-1.0682
4.7298	0.3380	0.2596	4.7301	0.3381	-0.2540	4.7823	0.3547	-0.6220	4.8557	0.3780	-0.8158	4.7830	0.3549	-1.0633
4.7354	0.3398	0.2637	4.7357	0.3399	-0.2542	4.7890	0.3568	-0.6212	4.8558	0.3780	-0.8172	4.7831	0.3550	-1.0618
4.7355	0.3398	0.2579	4.7359	0.3399	-0.2552	4.7892	0.3569	-0.6208	4.8718	0.3831	-0.8157	4.7900	0.3571	-1.0675
4.7476	0.3437	0.2658	4.7479	0.3438	-0.2516	4.8281	0.3692	-0.6116	4.8720	0.3832	-0.8152	4.7901	0.3572	-1.0691
4.7478	0.3437	0.2706	4.7481	0.3438	-0.2466	4.8283	0.3693	-0.6160	4.8786	0.3853	-0.8102	4.8289	0.3695	-1.0628
4.7525	0.3452	0.2665	4.7528	0.3453	-0.2479	4.8349	0.3714	-0.6099	4.8788	0.3853	-0.8120	4.8291	0.3696	-1.0597
4.7527	0.3453	0.2692	4.7530	0.3454	-0.2452	4.8351	0.3714	-0.6131	4.8937	0.3901	-0.8064	4.8357	0.3717	-1.0564

4.7644	0.3490	0.2632	4.7647	0.3491	-0.2468	4.8485	0.3757	-0.6082	4.8938	0.3901	-0.8065	4.8359	0.3717	-1.0551
4.7645	0.3491	0.2692	4.7649	0.3492	-0.2477	4.8487	0.3758	-0.6126	4.9008	0.3923	-0.7961	4.8494	0.3760	-1.0563
4.7813	0.3544	0.2833	4.7817	0.3545	-0.2493	4.8553	0.3779	-0.6043	4.9010	0.3924	-0.7963	4.8495	0.3760	-1.0535
4.7815	0.3544	0.2718	4.7818	0.3545	-0.2487	4.8555	0.3779	-0.6063	4.9261	0.4004	-0.8126	4.8561	0.3781	-1.0540
4.7882	0.3566	0.2814	4.7885	0.3567	-0.2375	4.8714	0.3830	-0.6046	4.9263	0.4004	-0.8158	4.8563	0.3782	-1.0566
4.7883	0.3566	0.2800	4.7887	0.3567	-0.2332	4.8716	0.3831	-0.6067	4.9331	0.4026	-0.8033	4.8723	0.3833	-1.0523
4.8272	0.3690	0.2988	4.8276	0.3691	-0.2334	4.8783	0.3852	-0.6075	4.9333	0.4026	-0.8058	4.8724	0.3833	-1.0538
4.8274	0.3690	0.2988	4.8278	0.3691	-0.2327	4.8784	0.3852	-0.6076	4.9489	0.4076	-0.8013	4.8791	0.3854	-1.0525
4.8340	0.3711	0.3022	4.8344	0.3712	-0.2304	4.8933	0.3900	-0.5972	4.9490	0.4076	-0.8030	4.8793	0.3855	-1.0523
4.8342	0.3712	0.3095	4.8345	0.3713	-0.2295	4.8935	0.3900	-0.5999	4.9569	0.4101	-0.7916	4.8942	0.3902	-1.0498
4.8476	0.3754	0.3074	4.8479	0.3755	-0.2183	4.9004	0.3922	-0.5986	5.8735	0.7012	-0.8568	4.8943	0.3903	-1.0444
4.8478	0.3755	0.3180	4.8481	0.3756	-0.2210	4.9006	0.3923	-0.5954	5.8737	0.7013	-0.8565	4.9014	0.3925	-1.0461
4.8545	0.3776	0.3096	4.8548	0.3777	-0.2198	4.9258	0.4003	-0.5923	5.8792	0.7030	-0.8583	4.9016	0.3926	-1.0492
4.8547	0.3777	0.3094	4.8709	0.3828	-0.2150	4.9259	0.4003	-0.5909	5.8794	0.7031	-0.8543	4.9267	0.4005	-1.0396
4.8705	0.3827	0.3158	4.8710	0.3829	-0.2155	4.9328	0.4025	-0.5903	6.6917	0.9611	-1.0279	4.9268	0.4006	-1.0424
4.8707	0.3828	0.3174	4.8778	0.3850	-0.2116	4.9330	0.4025	-0.5892	6.6919	0.9611	-1.0363	4.9336	0.4027	-1.0420
4.8775	0.3849	0.3199	4.8780	0.3851	-0.2100	4.9485	0.4075	-0.5936	6.6968	0.9627	-1.0403	4.9338	0.4028	-1.0409
4.8776	0.3850	0.3169	4.8928	0.3898	-0.2060	4.9487	0.4075	-0.5963	6.6970	0.9628	-1.0331	4.9493	0.4077	-1.0524
4.8924	0.3897	0.3263	4.8929	0.3898	-0.2027	4.9565	0.4100	-0.5851	6.7017	0.9642	-1.0241	4.9495	0.4078	-1.0447
4.8926	0.3897	0.3304	4.8999	0.3920	-0.2109	4.9567	0.4101	-0.5869	6.7018	0.9643	-1.0290	4.9575	0.4103	-1.0378
4.8996	0.3919	0.3251	4.9001	0.3921	-0.2063	5.8731	0.7011	-0.6681	6.7158	0.9687	-1.0346	4.9576	0.4104	-1.0398
4.8997	0.3920	0.3233	4.9253	0.4001	-0.2005	5.8733	0.7012	-0.6686	6.7160	0.9688	-1.0331	5.8742	0.7014	-1.0781
4.9250	0.4000	0.3310	4.9255	0.4002	-0.2009	5.8788	0.7029	-0.6716	6.7205	0.9702	-1.0234	5.8743	0.7015	-1.0817
4.9251	0.4001	0.3345	4.9323	0.4023	-0.1987	5.8790	0.7030	-0.6729	6.7207	0.9703	-1.0241	5.8799	0.7033	-1.0694
4.9319	0.4022	0.3331	4.9324	0.4024	-0.2021	5.8844	0.7047	-0.6709	6.7255	0.9718	-1.0197	5.8801	0.7033	-1.0742
4.9321	0.4023	0.3364	4.9479	0.4073	-0.1897	5.8957	0.7083	-0.6775	6.7426	0.9773	-1.0256	5.8854	0.7050	-1.0784

4.9475	0.4072	0.3355	4.9480	0.4073	-0.1884	5.8959	0.7084	-0.6811	6.7428	0.9773	-1.0288	5.8856	0.7051	-1.0765
4.9477	0.4072	0.3428	4.9557	0.4098	-0.1829	6.6964	0.9626	-0.8811	6.7474	0.9788	-1.0294	6.6922	0.9613	-1.2017
4.9554	0.4097	0.3446	5.8783	0.7027	-0.3580	6.6966	0.9626	-0.8905	6.7475	0.9788	-1.0196	6.6924	0.9613	-1.2184
4.9556	0.4097	0.3389	5.8784	0.7028	-0.3542	6.7013	0.9641	-0.8849	6.7521	0.9803	-1.0254	6.6975	0.9629	-1.2157
5.8779	0.7026	0.1099	5.8838	0.7045	-0.3539	6.7155	0.9686	-0.8802	6.7523	0.9803	-1.0216	6.7022	0.9644	-1.2183
5.8781	0.7027	0.1135	5.8840	0.7046	-0.3493	6.7156	0.9687	-0.8868	6.7674	0.9851	-1.0372	6.7024	0.9645	-1.2067
5.8834	0.7044	0.1116	5.8952	0.7081	-0.3286	6.7202	0.9701	-0.8822	6.7676	0.9852	-1.0293	6.7164	0.9689	-1.2223
5.8836	0.7045	0.1039	6.6959	0.9624	-0.6373	6.7204	0.9702	-0.8945	6.7723	0.9867	-1.0262	6.7165	0.9690	-1.2205
5.8948	0.7080	0.0946	6.7008	0.9640	-0.6414	6.7249	0.9716	-0.8858	6.7725	0.9867	-1.0235	6.7210	0.9704	-1.2079
5.8950	0.7081	0.1041	6.7010	0.9640	-0.6403	6.7423	0.9771	-0.8872	6.7771	0.9882	-1.0277	6.7212	0.9705	-1.2119
6.6904	0.9607	-0.2322	6.7149	0.9685	-0.6520	6.7425	0.9772	-0.8878	6.7773	0.9883	-1.0370	6.7258	0.9719	-1.2133
6.6906	0.9607	-0.2284	6.7151	0.9685	-0.6569	6.7470	0.9786	-0.8790	6.7985	0.9950	-1.0310	6.7260	0.9720	-1.2128
6.6957	0.9624	-0.2478	6.7197	0.9700	-0.6490	6.7472	0.9787	-0.8790	6.7986	0.9950	-1.0317	6.7432	0.9774	-1.2160
6.7005	0.9639	-0.2319	6.7199	0.9700	-0.6435	6.7518	0.9802	-0.8794	6.8116	0.9992	-1.0354	6.7433	0.9775	-1.2183
6.7007	0.9639	-0.2187	6.7418	0.9770	-0.6578	6.7520	0.9802	-0.8811	6.8118	0.9992	-1.0311	6.7479	0.9789	-1.2121
6.7147	0.9684	-0.2393	6.7419	0.9770	-0.6504	6.7671	0.9850	-0.8899	6.8163	0.0007	-1.0416	6.7481	0.9790	-1.2212
6.7193	0.9699	-0.2100	6.7465	0.9785	-0.6474	6.7673	0.9851	-0.9005	6.8165	0.0007	-1.0446	6.7527	0.9804	-1.2142
6.7195	0.9699	-0.2219	6.7467	0.9785	-0.6509	6.7720	0.9866	-0.8770	6.8417	0.0087	-1.0243	6.7528	0.9805	-1.2232
6.7240	0.9714	-0.2192	6.7513	0.9800	-0.6555	6.7721	0.9866	-0.8777	6.8447	0.0097	-1.0375	6.7679	0.9853	-1.2152
6.7242	0.9714	-0.2167	6.7515	0.9801	-0.6558	6.7768	0.9881	-0.8949	6.8477	0.0106	-1.0430	6.7681	0.9853	-1.2240
6.7414	0.9769	-0.2334	6.7666	0.9849	-0.6571	6.7770	0.9882	-0.8974	6.8500	0.0113	-1.0411	6.7728	0.9868	-1.2067
6.7416	0.9769	-0.2303	6.7668	0.9849	-0.6541	6.7932	0.9933	-0.8821	6.8530	0.0123	-1.0353	6.7730	0.9869	-1.2050
6.7462	0.9784	-0.2246	6.7715	0.9864	-0.6633	6.7934	0.9934	-0.8808	8.6940	0.5970	-0.7799	6.7776	0.9884	-1.2189
6.7463	0.9784	-0.2191	6.7717	0.9865	-0.6501	6.7981	0.9949	-0.8830	8.6942	0.5970	-0.7765	6.7778	0.9884	-1.2215
6.7509	0.9799	-0.2288	6.7880	0.9917	-0.6455	6.7983	0.9949	-0.8856	8.8525	0.6473	-0.8043	6.7894	0.9921	-1.2156
6.7511	0.9800	-0.2190	6.7976	0.9947	-0.6493	6.8112	0.9990	-0.8801	8.8527	0.6474	-0.8082	6.7896	0.9922	-1.2217

6.7663	0.9848	-0.2231	6.7978	0.9948	-0.6525	6.8114	0.9991	-0.8879	8.8565	0.6486	-0.8133	6.7941	0.9936	-1.2191
6.7664	0.9848	-0.2192	6.8107	0.9989	-0.6471	6.8159	0.0005	-0.8966	8.8567	0.6487	-0.8044	6.7943	0.9937	-1.2185
6.7713	0.9864	-0.2242	6.8109	0.9989	-0.6457	6.8161	0.0006	-0.8961	8.8609	0.6500	-0.8021	6.7990	0.9951	-1.2074
6.7759	0.9878	-0.2353	6.8202	0.0019	-0.6479	6.8415	0.0087	-0.8921	8.8611	0.6500	-0.8089	6.7991	0.9952	-1.2111
6.7761	0.9879	-0.2443	6.8437	0.0094	-0.6509	6.8446	0.0096	-0.8902	8.8714	0.6533	-0.8261	6.8121	0.9993	-1.2200
6.7877	0.9916	-0.2303	6.8467	0.0103	-0.6493	6.8469	0.0104	-0.8828	8.8715	0.6534	-0.8130	6.8122	0.9994	-1.2060
6.7878	0.9916	-0.2274	6.8490	0.0110	-0.6440	6.8498	0.0113	-0.8807	8.8759	0.6547	-0.8097	6.8168	0.0008	-1.2239
6.7973	0.9946	-0.2276	6.8519	0.0120	-0.6473	6.8521	0.0120	-0.8940	8.8801	0.6561	-0.8154	6.8170	0.0009	-1.2226
6.7974	0.9947	-0.2215	8.6935	0.5968	-0.1942	6.8618	0.0151	-0.8982	8.8906	0.6594	-0.8104	6.8426	0.0090	-1.2346
6.8104	0.9988	-0.2148	8.8517	0.6471	-0.2620	8.6937	0.5969	-0.5706	8.8974	0.6616	-0.8359	6.8456	0.0099	-1.2190
6.8106	0.9988	-0.2109	8.8519	0.6471	-0.2792	8.6938	0.5969	-0.5840	8.8975	0.6616	-0.8275	6.8479	0.0107	-1.2220
6.8151	0.0003	-0.2510	8.8559	0.6484	-0.2635	8.8520	0.6472	-0.6179	8.9017	0.6630	-0.8301	6.8508	0.0116	-1.2248
6.8153	0.0003	-0.2486	8.8560	0.6484	-0.2657	8.8522	0.6472	-0.6236	8.9019	0.6630	-0.8236	6.8532	0.0124	-1.2256
6.8198	0.0018	-0.2503	8.8601	0.6497	-0.2664	8.8562	0.6485	-0.6107	8.9132	0.6666	-0.8256	8.6943	0.5971	-1.0195
6.8200	0.0018	-0.2447	8.8603	0.6498	-0.2565	8.8564	0.6485	-0.6128	8.9172	0.6679	-0.8223	8.6945	0.5971	-1.0132
6.8404	0.0083	-0.2326	8.8705	0.6530	-0.2655	8.8605	0.6498	-0.6133	8.9174	0.6679	-0.8280	8.8529	0.6474	-1.0369
6.8458	0.0100	-0.2304	8.8707	0.6531	-0.2745	8.8606	0.6499	-0.6158	8.9214	0.6692	-0.8369	8.8530	0.6475	-1.0452
6.8488	0.0110	-0.2190	8.8749	0.6544	-0.2616	8.8709	0.6531	-0.6227	8.9216	0.6693	-0.8252	8.8569	0.6487	-1.0341
6.8511	0.0117	-0.2179	8.8751	0.6545	-0.2745	8.8710	0.6532	-0.6235	8.9322	0.6726	-0.8321	8.8570	0.6488	-1.0305
6.8605	0.0147	-0.2320	8.8792	0.6558	-0.2751	8.8753	0.6545	-0.6155	8.9324	0.6727	-0.8315	8.8613	0.6501	-1.0384
8.6931	0.5967	0.3244	8.8898	0.6592	-0.2854	8.8754	0.6546	-0.6328	8.9365	0.6740	-0.8492	8.8717	0.6534	-1.0398
8.8514	0.6469	0.2243	8.8965	0.6613	-0.2891	8.8796	0.6559	-0.6247	8.9367	0.6741	-0.8323	8.8719	0.6535	-1.0341
8.8555	0.6483	0.2208	8.8967	0.6613	-0.2870	8.8798	0.6560	-0.6156	8.9412	0.6755	-0.8357	8.8761	0.6548	-1.0417
8.8557	0.6483	0.2320	8.9009	0.6627	-0.2909	8.8902	0.6593	-0.6317	8.9414	0.6755	-0.8523	8.8762	0.6549	-1.0458
8.8598	0.6496	0.2331	8.9011	0.6627	-0.2969	8.8904	0.6593	-0.6247	8.9525	0.6791	-0.8380	8.8804	0.6562	-1.0378
8.8600	0.6497	0.2124	8.9122	0.6663	-0.2850	8.8968	0.6614	-0.6445	8.9526	0.6791	-0.8222	8.8806	0.6562	-1.0414

8.8702	0.6529	0.2145	8.9123	0.6663	-0.2750	8.8970	0.6614	-0.6395	8.9568	0.6804	-0.8497	8.8911	0.6596	-1.0545
8.8704	0.6530	0.2171	8.9164	0.6676	-0.2919	8.9014	0.6629	-0.6292	8.9570	0.6805	-0.8413	8.8912	0.6596	-1.0500
8.8746	0.6543	0.2058	8.9166	0.6677	-0.2743	8.9125	0.6664	-0.6456	8.9571	0.6805	-0.8275	8.8977	0.6617	-1.0408
8.8747	0.6544	0.2153	8.9207	0.6690	-0.2959	8.9127	0.6664	-0.6290	8.9612	0.6818	-0.8237	8.8979	0.6617	-1.0428
8.8789	0.6557	0.1851	8.9208	0.6690	-0.2867	8.9167	0.6677	-0.6350	8.9613	0.6819	-0.8323	8.9021	0.6631	-1.0550
8.8791	0.6557	0.2146	8.9314	0.6724	-0.2950	8.9169	0.6678	-0.6271	8.9726	0.6855	-0.8385	8.9022	0.6631	-1.0437
8.8895	0.6591	0.2074	8.9316	0.6724	-0.2853	8.9210	0.6691	-0.6255	8.9728	0.6855	-0.8463	8.9133	0.6666	-1.0526
8.8897	0.6591	0.1869	8.9357	0.6737	-0.2903	8.9212	0.6691	-0.6288	8.9769	0.6868	-0.8514	8.9135	0.6667	-1.0387
8.8962	0.6612	0.2099	8.9359	0.6738	-0.3010	8.9317	0.6725	-0.6421	8.9770	0.6869	-0.8400	8.9176	0.6680	-1.0511
8.8963	0.6612	0.2124	8.9400	0.6751	-0.3206	8.9319	0.6725	-0.6454	8.9817	0.6884	-0.8461	8.9177	0.6680	-1.0371
8.9006	0.6626	0.1905	8.9402	0.6752	-0.3048	8.9361	0.6738	-0.6316	9.7115	0.9201	-1.0228	8.9218	0.6693	-1.0455
8.9008	0.6626	0.2107	8.9403	0.6752	-0.2895	8.9362	0.6739	-0.6385	9.7117	0.9202	-1.0159	8.9220	0.6694	-1.0585
8.9118	0.6662	0.1778	8.9516	0.6788	-0.3191	8.9405	0.6753	-0.6379	9.7159	0.9215	-1.0224	8.9326	0.6727	-1.0723
8.9120	0.6662	0.1855	8.9518	0.6788	-0.3111	8.9407	0.6753	-0.6442	9.7161	0.9216	-1.0180	8.9327	0.6728	-1.0770
8.9161	0.6675	0.1970	8.9560	0.6802	-0.3316	8.9408	0.6754	-0.6313	9.7202	0.9229	-1.0083	8.9369	0.6741	-1.0341
8.9162	0.6675	0.1870	8.9562	0.6802	-0.2954	8.9520	0.6789	-0.6520	9.7204	0.9229	-1.0146	8.9370	0.6742	-1.0598
8.9203	0.6688	0.1821	8.9603	0.6816	-0.3194	8.9521	0.6790	-0.6497	9.7730	0.9396	-1.0255	8.9415	0.6756	-1.0645
8.9205	0.6689	0.1666	8.9605	0.6816	-0.2943	8.9563	0.6803	-0.6511	9.7731	0.9397	-1.0294	8.9417	0.6756	-1.0445
8.9310	0.6723	0.1592	8.9718	0.6852	-0.3318	8.9565	0.6803	-0.6418	9.7773	0.9410	-1.0208	8.9528	0.6792	-1.0811
8.9312	0.6723	0.1836	8.9720	0.6853	-0.3396	8.9607	0.6817	-0.6522	9.7774	0.9411	-1.0236	8.9530	0.6792	-1.0515
8.9354	0.6736	0.1664	8.9760	0.6865	-0.3221	8.9608	0.6817	-0.6299	9.7817	0.9424	-1.0227	8.9573	0.6806	-1.0508
8.9355	0.6737	0.1749	8.9762	0.6866	-0.3049	8.9722	0.6853	-0.6546	9.7819	0.9425	-1.0217	8.9575	0.6807	-1.0590
8.9397	0.6750	0.1701	8.9808	0.6880	-0.3285	8.9723	0.6854	-0.6666	9.7923	0.9458	-1.0310	8.9615	0.6819	-1.0739
8.9399	0.6751	0.1769	8.9809	0.6881	-0.3093	8.9811	0.6882	-0.6513	9.7924	0.9458	-1.0310	8.9617	0.6820	-1.0607
8.9513	0.6787	0.1701	9.7107	0.9198	-0.6435	8.9813	0.6882	-0.6556	9.7964	0.9471	-1.0316	8.9730	0.6856	-1.0504
8.9514	0.6787	0.1433	9.7108	0.9199	-0.6402	9.7110	0.9200	-0.8677	9.7966	0.9471	-1.0300	8.9731	0.6856	-1.0611

8.9557	0.6801	0.1452	9.7151	0.9213	-0.6316	9.7112	0.9200	-0.8577	9.8006	0.9484	-1.0257	8.9772	0.6869	-1.0588
8.9558	0.6801	0.1520	9.7153	0.9213	-0.6493	9.7155	0.9214	-0.8806	9.8008	0.9485	-1.0310	8.9774	0.6870	-1.0438
8.9600	0.6814	0.1426	9.7193	0.9226	-0.6504	9.7156	0.9214	-0.8661	9.8118	0.9520	-1.0309	8.9819	0.6884	-1.0700
8.9602	0.6815	0.1412	9.7195	0.9227	-0.6396	9.7197	0.9227	-0.8675	9.8119	0.9520	-1.0364	8.9821	0.6885	-1.0733
8.9715	0.6851	0.1455	9.7722	0.9394	-0.6510	9.7198	0.9228	-0.8799	9.8160	0.9533	-1.0319	9.7119	0.9202	-1.1969
8.9716	0.6851	0.1566	9.7724	0.9394	-0.6447	9.7725	0.9395	-0.8861	9.8162	0.9534	-1.0354	9.7120	0.9203	-1.2083
8.9757	0.6864	0.1451	9.7764	0.9407	-0.6530	9.7727	0.9395	-0.8872	9.8202	0.9546	-1.0308	9.7162	0.9216	-1.2086
8.9759	0.6865	0.1417	9.7766	0.9408	-0.6524	9.7768	0.9408	-0.8799	9.8204	0.9547	-1.0329	9.7164	0.9217	-1.1961
8.9804	0.6879	0.1459	9.7809	0.9421	-0.6508	9.7769	0.9409	-0.8879	9.8306	0.9579	-1.0287	9.7206	0.9230	-1.2018
8.9806	0.6880	0.1380	9.7810	0.9422	-0.6556	9.7812	0.9423	-0.8813	9.8308	0.9580	-1.0313	9.7207	0.9230	-1.1972
9.7103	0.9197	-0.2174	9.7914	0.9455	-0.6574	9.7814	0.9423	-0.8814	9.8348	0.9593	-1.0295	9.7733	0.9398	-1.2143
9.7105	0.9198	-0.2034	9.7916	0.9456	-0.6558	9.7918	0.9456	-0.8864	9.8349	0.9593	-1.0314	9.7735	0.9398	-1.2140
9.7148	0.9212	-0.2210	9.7956	0.9468	-0.6563	9.7919	0.9457	-0.8884	9.8391	0.9606	-1.0300	9.7776	0.9411	-1.2153
9.7190	0.9225	-0.2127	9.7958	0.9469	-0.6516	9.7960	0.9469	-0.8888	9.8392	0.9607	-1.0315	9.7778	0.9412	-1.2119
9.7192	0.9225	-0.2254	9.7998	0.9482	-0.6507	9.7961	0.9470	-0.8862	9.8498	0.9640	-1.0259	9.7820	0.9425	-1.2116
9.7719	0.9393	-0.2262	9.8000	0.9482	-0.6462	9.8001	0.9483	-0.8833	9.8499	0.9641	-1.0233	9.7822	0.9426	-1.2098
9.7720	0.9393	-0.2201	9.8110	0.9517	-0.6628	9.8003	0.9483	-0.8747	9.8540	0.9654	-1.0272	9.7926	0.9459	-1.2143
9.7761	0.9406	-0.2351	9.8111	0.9518	-0.6598	9.8113	0.9518	-0.8914	9.8542	0.9654	-1.0289	9.7928	0.9459	-1.2128
9.7763	0.9407	-0.2292	9.8152	0.9530	-0.6533	9.8115	0.9519	-0.8943	9.8582	0.9667	-1.0261	9.7968	0.9472	-1.2192
9.7805	0.9420	-0.2297	9.8153	0.9531	-0.6553	9.8155	0.9531	-0.8901	9.8584	0.9668	-1.0235	9.7969	0.9473	-1.2184
9.7807	0.9421	-0.2355	9.8194	0.9544	-0.6509	9.8157	0.9532	-0.8889	9.9330	0.9904	-1.0316	9.8009	0.9485	-1.2139
9.7911	0.9454	-0.2281	9.8196	0.9544	-0.6519	9.8198	0.9545	-0.8795	9.9331	0.9905	-1.0304	9.8011	0.9486	-1.2133
9.7913	0.9454	-0.2260	9.8298	0.9577	-0.6564	9.8199	0.9546	-0.8821	9.9373	0.9918	-1.0439	9.8121	0.9521	-1.2161
9.7953	0.9467	-0.2294	9.8300	0.9577	-0.6573	9.8301	0.9578	-0.8865	9.9374	0.9919	-1.0378	9.8123	0.9521	-1.2171
9.7955	0.9468	-0.2242	9.8339	0.9590	-0.6541	9.8303	0.9578	-0.8917	9.9416	0.9932	-1.0405	9.8163	0.9534	-1.2183
9.7994	0.9480	-0.2260	9.8341	0.9590	-0.6570	9.8343	0.9591	-0.8905	9.9417	0.9932	-1.0361	9.8165	0.9535	-1.2140

9.7996	0.9481	-0.2245	9.8383	0.9604	-0.6625	9.8344	0.9592	-0.8919	9.9527	0.9967	-1.0320	9.8206	0.9548	-1.2166
9.8106	0.9516	-0.2286	9.8384	0.9604	-0.6579	9.8386	0.9605	-0.8841	9.9528	0.9968	-1.0277	9.8207	0.9548	-1.2188
9.8108	0.9516	-0.2382	9.8490	0.9638	-0.6550	9.8388	0.9605	-0.8857	9.9572	0.9982	-1.0291	9.8309	0.9580	-1.2083
9.8148	0.9529	-0.2254	9.8491	0.9638	-0.6603	9.8493	0.9639	-0.8832	9.9574	0.9982	-1.0325	9.8311	0.9581	-1.2096
9.8150	0.9530	-0.2307	9.8532	0.9651	-0.6542	9.8495	0.9639	-0.8878	9.9615	0.9995	-1.0325	9.8351	0.9594	-1.2194
9.8191	0.9543	-0.2304	9.8534	0.9652	-0.6542	9.8535	0.9652	-0.8851	9.9616	0.9996	-1.0321	9.8353	0.9594	-1.2179
9.8192	0.9543	-0.2274	9.8574	0.9665	-0.6609	9.8537	0.9653	-0.8870	9.9778	0.0047	-1.0261	9.8394	0.9607	-1.2179
9.8295	0.9576	-0.2289	9.8576	0.9665	-0.6535	9.8578	0.9666	-0.8889	9.9779	0.0047	-1.0213	9.8396	0.9608	-1.2129
9.8296	0.9576	-0.2354	9.9321	0.9902	-0.6505	9.8579	0.9666	-0.8865	9.9820	0.0060	-1.0312	9.8501	0.9641	-1.2033
9.8336	0.9589	-0.2343	9.9323	0.9902	-0.6564	9.9325	0.9903	-0.8889	9.9822	0.0061	-1.0317	9.8503	0.9642	-1.2044
9.8338	0.9589	-0.2344	9.9364	0.9915	-0.6565	9.9326	0.9903	-0.8916	9.9866	0.0075	-1.0437	9.8544	0.9655	-1.2129
9.8379	0.9603	-0.2317	9.9366	0.9916	-0.6569	9.9368	0.9917	-0.8962	9.9868	0.0075	-1.0338	9.8546	0.9655	-1.2182
9.8381	0.9603	-0.2343	9.9407	0.9929	-0.6550	9.9411	0.9930	-0.8878	10.8041	0.2671	-0.8897	9.8586	0.9668	-1.2142
9.8486	0.9637	-0.2351	9.9409	0.9930	-0.6586	9.9412	0.9931	-0.8885	10.8043	0.2672	-0.8897	9.8587	0.9669	-1.2093
9.8488	0.9637	-0.2334	9.9518	0.9964	-0.6517	9.9522	0.9965	-0.8816	10.8090	0.2687	-0.8868	9.9333	0.9906	-1.2116
9.8529	0.9650	-0.2271	9.9520	0.9965	-0.6470	9.9523	0.9966	-0.8812	10.8092	0.2687	-0.8865	9.9335	0.9906	-1.2156
9.8530	0.9651	-0.2222	9.9564	0.9979	-0.6488	9.9567	0.9980	-0.8881	10.8946	0.2958	-0.8698	9.9376	0.9919	-1.2206
9.8571	0.9663	-0.2292	9.9566	0.9979	-0.6466	9.9569	0.9981	-0.8794	10.8948	0.2959	-0.8700	9.9377	0.9920	-1.2170
9.8572	0.9664	-0.2351	9.9607	0.9993	-0.6465	9.9610	0.9994	-0.8784	10.8990	0.2973	-0.8598	9.9419	0.9933	-1.2151
9.9318	0.9901	-0.2272	9.9609	0.9993	-0.6536	9.9612	0.9994	-0.8821	10.8992	0.2973	-0.8632	9.9421	0.9933	-1.2257
9.9319	0.9901	-0.2233	9.9768	0.0044	-0.6474	9.9771	0.0045	-0.8781	10.9033	0.2986	-0.8628	9.9530	0.9968	-1.2051
9.9361	0.9914	-0.2293	9.9770	0.0044	-0.6468	9.9773	0.0045	-0.8795	10.9034	0.2987	-0.8643	9.9532	0.9969	-1.2053
9.9363	0.9915	-0.2193	9.9812	0.0058	-0.6554	9.9775	0.0046	-0.8833	10.9122	0.3014	-0.8596	9.9576	0.9983	-1.2158
9.9404	0.9928	-0.2258	9.9813	0.0058	-0.6537	9.9815	0.0059	-0.8905	10.9124	0.3015	-0.8625	9.9577	0.9983	-1.2192
9.9405	0.9929	-0.2275	9.9858	0.0072	-0.6550	9.9817	0.0059	-0.8923	10.9164	0.3028	-0.8583	9.9618	0.9996	-1.2194
9.9515	0.9963	-0.2274	9.9859	0.0073	-0.6545	9.9863	0.0074	-0.8997	10.9166	0.3028	-0.8623	9.9620	0.9997	-1.2146

9.9516	0.9964	-0.2161	10.8031	0.2668	-0.3437	10.8035	0.2669	-0.6880	10.9206	0.3041	-0.8635	9.9781	0.0048	-1.2093
9.9561	0.9978	-0.2310	10.8033	0.2668	-0.3467	10.8037	0.2670	-0.6822	10.9208	0.3042	-0.8631	9.9783	0.0048	-1.2125
9.9562	0.9978	-0.2240	10.8081	0.2684	-0.3422	10.8085	0.2685	-0.6957	10.9290	0.3068	-0.8552	9.9823	0.0061	-1.2231
9.9604	0.9991	-0.2340	10.8083	0.2684	-0.3469	10.8086	0.2685	-0.7008	10.9292	0.3068	-0.8594	9.9825	0.0062	-1.2264
9.9605	0.9992	-0.2379	10.8937	0.2956	-0.3084	10.8125	0.2698	-0.6903	10.9333	0.3081	-0.8626	9.9870	0.0076	-1.2257
9.9765	0.0043	-0.2330	10.8938	0.2956	-0.3017	10.8127	0.2698	-0.6931	10.9334	0.3082	-0.8632	9.9871	0.0076	-1.2214
9.9766	0.0043	-0.2371	10.8982	0.2970	-0.3030	10.8940	0.2957	-0.6688	10.9374	0.3094	-0.8562	10.8045	0.2672	-1.1161
9.9808	0.0056	-0.2285	10.8984	0.2971	-0.3053	10.8942	0.2957	-0.6671	10.9376	0.3095	-0.8567	10.8047	0.2673	-1.1093
9.9810	0.0057	-0.2292	10.9024	0.2983	-0.3005	10.8986	0.2971	-0.6705	11.8234	0.5908	-0.7819	10.8094	0.2688	-1.1055
9.9854	0.0071	-0.2130	10.9026	0.2984	-0.2992	10.8987	0.2972	-0.6714	11.8236	0.5909	-0.7823	10.8096	0.2689	-1.1015
9.9856	0.0072	-0.2277	10.9114	0.3012	-0.2983	10.9028	0.2984	-0.6724	11.8274	0.5921	-0.7821	10.8949	0.2960	-1.0996
10.8027	0.2667	0.1445	10.9115	0.3012	-0.2927	10.9029	0.2985	-0.6682	11.8276	0.5921	-0.7822	10.8951	0.2960	-1.0979
10.8029	0.2667	0.1476	10.9156	0.3025	-0.2985	10.9117	0.3013	-0.6614	11.8314	0.5934	-0.7791	10.8994	0.2974	-1.0873
10.8077	0.2683	0.1571	10.9158	0.3026	-0.2947	10.9119	0.3013	-0.6581	11.8316	0.5934	-0.7827	10.8996	0.2974	-1.0863
10.8079	0.2683	0.1533	10.9198	0.3038	-0.2982	10.9160	0.3026	-0.6669	11.8393	0.5959	-0.7794	10.9036	0.2987	-1.1000
10.8933	0.2954	0.1996	10.9199	0.3039	-0.2971	10.9161	0.3027	-0.6692	11.8394	0.5959	-0.7754	10.9038	0.2988	-1.0977
10.8935	0.2955	0.1979	10.9284	0.3066	-0.2870	10.9201	0.3039	-0.6614	11.8433	0.5971	-0.7834	10.9126	0.3016	-1.0993
10.8979	0.2969	0.2016	10.9324	0.3079	-0.2990	10.9203	0.3040	-0.6620	11.8435	0.5972	-0.7846	10.9127	0.3016	-1.0989
10.8981	0.2969	0.1974	10.9326	0.3079	-0.2981	10.9285	0.3066	-0.6643	11.8474	0.5984	-0.7816	10.9168	0.3029	-1.1052
10.9021	0.2982	0.2099	10.9366	0.3092	-0.2872	10.9287	0.3067	-0.6680	11.8476	0.5985	-0.7881	10.9169	0.3029	-1.1023
10.9022	0.2983	0.2040	10.9367	0.3092	-0.2865	10.9328	0.3080	-0.6622	11.8554	0.6010	-0.7807	10.9210	0.3042	-1.0984
10.9110	0.3011	0.2064	11.8226	0.5906	-0.1969	10.9329	0.3080	-0.6664	11.8556	0.6010	-0.7836	10.9211	0.3043	-1.1011
10.9112	0.3011	0.2095	11.8227	0.5906	-0.2017	10.9369	0.3093	-0.6460	11.8597	0.6023	-0.7868	10.9293	0.3069	-1.0899
10.9153	0.3024	0.2063	11.8266	0.5918	-0.1951	10.9371	0.3093	-0.6460	11.8599	0.6024	-0.7868	10.9295	0.3069	-1.0937
10.9154	0.3025	0.2087	11.8268	0.5919	-0.1945	11.8229	0.5907	-0.5835	11.8638	0.6037	-0.7844	10.9336	0.3082	-1.0980
10.9194	0.3037	0.2121	11.8306	0.5931	-0.1957	11.8231	0.5907	-0.5828	11.8640	0.6037	-0.7863	10.9338	0.3083	-1.0951

10.9196	0.3038	0.2077	11.8308	0.5932	-0.1935	11.8270	0.5920	-0.5800	11.9000	0.6151	-0.7955	10.9378	0.3095	-1.0781
10.9321	0.3077	0.2091	11.8384	0.5956	-0.1971	11.8271	0.5920	-0.5836	11.9001	0.6152	-0.7987	10.9379	0.3096	-1.0759
10.9322	0.3078	0.2144	11.8386	0.5956	-0.1972	11.8310	0.5932	-0.5766	11.9042	0.6165	-0.7913	11.8238	0.5909	-1.0203
10.9362	0.3091	0.2137	11.8425	0.5969	-0.1952	11.8311	0.5933	-0.5744	11.9043	0.6165	-0.7938	11.8239	0.5910	-1.0224
10.9364	0.3091	0.2165	11.8426	0.5969	-0.1994	11.8388	0.5957	-0.5744	11.9083	0.6178	-0.7943	11.8278	0.5922	-1.0211
11.8222	0.5904	0.3168	11.8466	0.5982	-0.2009	11.8389	0.5958	-0.5749	11.9085	0.6178	-0.7985	11.8279	0.5923	-1.0175
11.8224	0.5905	0.3225	11.8468	0.5982	-0.2019	11.8428	0.5970	-0.5786	11.9165	0.6204	-0.7947	11.8318	0.5935	-1.0164
11.8263	0.5917	0.3218	11.8546	0.6007	-0.2023	11.8430	0.5970	-0.5831	11.9167	0.6204	-0.7884	11.8320	0.5935	-1.0138
11.8265	0.5918	0.3243	11.8548	0.6008	-0.2035	11.8470	0.5983	-0.5763	11.9207	0.6217	-0.7898	11.8396	0.5960	-1.0149
11.8303	0.5930	0.3247	11.8589	0.6021	-0.2018	11.8471	0.5983	-0.5763	11.9209	0.6218	-0.7941	11.8398	0.5960	-1.0148
11.8305	0.5931	0.3200	11.8590	0.6021	-0.2009	11.8549	0.6008	-0.5807	11.9250	0.6231	-0.7968	11.8436	0.5972	-1.0215
11.8381	0.5955	0.3166	11.8630	0.6034	-0.2041	11.8551	0.6009	-0.5779	11.9252	0.6231	-0.7979	11.8438	0.5973	-1.0194
11.8383	0.5955	0.3123	11.8632	0.6035	-0.2045	11.8592	0.6022	-0.5806	11.9332	0.6257	-0.8024	11.8477	0.5985	-1.0247
11.8421	0.5968	0.3111	11.8991	0.6149	-0.2208	11.8594	0.6022	-0.5804	11.9334	0.6257	-0.8016	11.8479	0.5986	-1.0255
11.8423	0.5968	0.3157	11.8993	0.6149	-0.2214	11.8634	0.6035	-0.5756	11.9372	0.6270	-0.8045	11.8558	0.6011	-1.0156
11.8463	0.5981	0.3175	11.9034	0.6162	-0.2190	11.8635	0.6036	-0.5776	11.9374	0.6270	-0.8067	11.8559	0.6011	-1.0169
11.8464	0.5981	0.3114	11.9035	0.6163	-0.2156	11.8995	0.6150	-0.5967	11.9413	0.6283	-0.7959	11.8601	0.6025	-1.0266
11.8542	0.6006	0.3175	11.9075	0.6175	-0.2243	11.8996	0.6150	-0.5959	11.9415	0.6283	-0.7991	11.8602	0.6025	-1.0269
11.8544	0.6007	0.3088	11.9077	0.6176	-0.2290	11.9037	0.6163	-0.5827	11.9499	0.6310	-0.8041	11.8642	0.6038	-1.0178
11.8585	0.6020	0.3101	11.9157	0.6201	-0.2270	11.9039	0.6164	-0.5718	11.9501	0.6311	-0.8039	11.8644	0.6038	-1.0156
11.8587	0.6020	0.3111	11.9159	0.6202	-0.2249	11.9079	0.6176	-0.5937	11.9542	0.6324	-0.8008	11.9003	0.6152	-1.0306
11.8627	0.6033	0.3063	11.9199	0.6215	-0.2324	11.9080	0.6177	-0.5958	11.9544	0.6324	-0.8000	11.9005	0.6153	-1.0343
11.8628	0.6033	0.3066	11.9201	0.6215	-0.2287	11.9161	0.6202	-0.5923	11.9584	0.6337	-0.7998	11.9045	0.6166	-1.0290
11.8988	0.6148	0.2877	11.9242	0.6228	-0.2336	11.9162	0.6203	-0.5904	11.9586	0.6337	-0.8022	11.9047	0.6166	-1.0279
11.8989	0.6148	0.2896	11.9243	0.6229	-0.2319	11.9203	0.6216	-0.5973	11.9665	0.6363	-0.8052	11.9087	0.6179	-1.0306
11.9030	0.6161	0.2798	11.9324	0.6254	-0.2328	11.9204	0.6216	-0.5956	11.9666	0.6363	-0.8092	11.9088	0.6179	-1.0268

11.9032	0.6162	0.2828	11.9325	0.6255	-0.2311	11.9245	0.6229	-0.6037	11.9705	0.6375	-0.8025	11.9169	0.6205	-1.0293
11.9072	0.6174	0.2791	11.9364	0.6267	-0.2348	11.9247	0.6230	-0.6007	11.9707	0.6376	-0.8003	11.9170	0.6206	-1.0300
11.9073	0.6175	0.2796	11.9366	0.6268	-0.2325	11.9327	0.6255	-0.6005	11.9747	0.6389	-0.8090	11.9210	0.6218	-1.0249
11.9154	0.6200	0.2713	11.9405	0.6280	-0.2362	11.9329	0.6256	-0.6005	11.9749	0.6389	-0.8100	11.9212	0.6219	-1.0273
11.9155	0.6201	0.2759	11.9407	0.6281	-0.2363	11.9368	0.6268	-0.6025	11.9831	0.6415	-0.8111	11.9253	0.6232	-1.0354
11.9196	0.6214	0.2771	11.9491	0.6307	-0.2437	11.9369	0.6269	-0.6071	11.9833	0.6416	-0.8148	11.9255	0.6232	-1.0352
11.9197	0.6214	0.2759	11.9492	0.6308	-0.2400	11.9409	0.6281	-0.5958	11.9873	0.6429	-0.8136	11.9335	0.6258	-1.0359
11.9238	0.6227	0.2728	11.9534	0.6321	-0.2367	11.9410	0.6282	-0.5970	11.9875	0.6429	-0.8169	11.9337	0.6258	-1.0370
11.9240	0.6228	0.2728	11.9536	0.6322	-0.2345	11.9494	0.6308	-0.6157	11.9915	0.6442	-0.8058	11.9376	0.6271	-1.0362
11.9320	0.6253	0.2642	11.9576	0.6334	-0.2453	11.9496	0.6309	-0.6068	11.9917	0.6442	-0.8098	11.9377	0.6271	-1.0377
11.9322	0.6254	0.2656	11.9578	0.6335	-0.2466	11.9537	0.6322	-0.5933	12.0017	0.6474	-0.8128	11.9417	0.6284	-1.0278
11.9361	0.6266	0.2665	11.9656	0.6360	-0.2509	11.9539	0.6323	-0.5868	12.0018	0.6475	-0.8103	11.9418	0.6284	-1.0316
11.9362	0.6266	0.2622	11.9658	0.6360	-0.2426	11.9579	0.6335	-0.6047	12.0061	0.6488	-0.8129	11.9503	0.6311	-1.0372
11.9402	0.6279	0.2574	11.9697	0.6373	-0.2481	11.9581	0.6336	-0.6094	12.0062	0.6489	-0.8169	11.9504	0.6312	-1.0361
11.9403	0.6280	0.2669	11.9699	0.6373	-0.2441	11.9660	0.6361	-0.6067	12.0102	0.6501	-0.8202	11.9545	0.6325	-1.0322
11.9487	0.6306	0.2535	11.9739	0.6386	-0.2543	11.9661	0.6361	-0.6015	12.0104	0.6502	-0.8214	11.9547	0.6325	-1.0310
11.9489	0.6307	0.2574	11.9741	0.6387	-0.2518	11.9700	0.6374	-0.6049	12.8320	0.9111	-1.0117	11.9587	0.6338	-1.0277
11.9531	0.6320	0.2494	11.9823	0.6413	-0.2586	11.9702	0.6374	-0.6061	12.9134	0.9370	-1.0195	11.9589	0.6339	-1.0318
11.9532	0.6320	0.2593	11.9825	0.6413	-0.2589	11.9742	0.6387	-0.6165	12.9571	0.9508	-1.0277	11.9668	0.6364	-1.0317
11.9573	0.6333	0.2464	11.9865	0.6426	-0.2570	11.9744	0.6388	-0.6115	12.9578	0.9511	-1.0239	11.9670	0.6364	-1.0301
11.9574	0.6334	0.2542	11.9866	0.6427	-0.2622	11.9826	0.6414	-0.6117	12.9585	0.9513	-1.0333	11.9708	0.6376	-1.0333
11.9653	0.6359	0.2459	11.9907	0.6439	-0.2601	11.9828	0.6414	-0.6146	12.9813	0.9585	-1.0275	11.9710	0.6377	-1.0305
11.9655	0.6359	0.2418	11.9908	0.6440	-0.2526	11.9868	0.6427	-0.6124	12.9820	0.9588	-1.0269	11.9751	0.6390	-1.0463
11.9694	0.6372	0.2461	12.0009	0.6472	-0.2618	11.9870	0.6428	-0.6185	12.9827	0.9590	-1.0280	11.9752	0.6390	-1.0473
11.9695	0.6372	0.2390	12.0010	0.6472	-0.2631	11.9910	0.6440	-0.6127	13.0018	0.9651	-1.0236	11.9834	0.6416	-1.0403
11.9736	0.6385	0.2411	12.0052	0.6486	-0.2648	11.9912	0.6441	-0.6088	13.0025	0.9653	-1.0248	11.9836	0.6417	-1.0391

11.9737	0.6386	0.2420	12.0054	0.6486	-0.2727	12.0012	0.6473	-0.6080	13.0031	0.9655	-1.0242	11.9876	0.6430	-1.0421
11.9819	0.6412	0.2222	12.0094	0.6499	-0.2577	12.0014	0.6473	-0.6141	13.0164	0.9697	-1.0372	11.9878	0.6430	-1.0439
11.9821	0.6412	0.2316	12.0096	0.6499	-0.2537	12.0056	0.6487	-0.6216	13.0170	0.9699	-1.0347	11.9918	0.6443	-1.0437
11.9861	0.6425	0.2228	12.9077	0.9352	-0.6596	12.0057	0.6487	-0.6230	13.0361	0.9759	-1.0426	11.9920	0.6444	-1.0383
11.9863	0.6425	0.2219	12.9091	0.9356	-0.6449	12.0097	0.6500	-0.6153	13.7146	0.1914	-0.9396	12.0020	0.6475	-1.0371
11.9903	0.6438	0.2242	12.9541	0.9499	-0.6380	12.0099	0.6500	-0.6108	13.7153	0.1916	-0.9465	12.0022	0.6476	-1.0369
11.9905	0.6439	0.2312	12.9769	0.9571	-0.6466	12.9099	0.9359	-0.8896	13.7571	0.2049	-0.9325	12.0064	0.6489	-1.0484
12.0005	0.6471	0.2146	12.9775	0.9573	-0.6508	12.9113	0.9363	-0.8793	13.7578	0.2052	-0.9317	12.0066	0.6490	-1.0448
12.0007	0.6471	0.2124	12.9782	0.9575	-0.6575	12.9549	0.9502	-0.8810	13.7850	0.2138	-0.9211	12.0106	0.6503	-1.0455
12.0049	0.6485	0.2171	12.9975	0.9637	-0.6429	12.9556	0.9504	-0.8849	13.7856	0.2140	-0.9270	12.0107	0.6503	-1.0462
12.0051	0.6485	0.2150	12.9982	0.9639	-0.6489	12.9562	0.9506	-0.8835	13.7963	0.2174	-0.9225	12.9170	0.9381	-1.2103
12.0091	0.6498	0.2129	13.0121	0.9683	-0.6633	12.9791	0.9578	-0.8843	13.7970	0.2176	-0.9219	12.9593	0.9516	-1.2166
12.0092	0.6498	0.2039	13.0128	0.9686	-0.6639	12.9797	0.9580	-0.8886	13.8103	0.2218	-0.9177	12.9600	0.9518	-1.2150
12.8248	0.9088	-0.2152	13.0335	0.9751	-0.6664	12.9804	0.9583	-0.8861	13.8110	0.2220	-0.9201	12.9606	0.9520	-1.2154
12.9054	0.9344	-0.2177	13.7103	0.1900	-0.4599	13.0003	0.9646	-0.8847	13.8243	0.2262	-0.9193	12.9848	0.9597	-1.2144
12.9512	0.9490	-0.2272	13.7109	0.1903	-0.4698	13.0010	0.9648	-0.8894	13.8249	0.2265	-0.9183	13.0039	0.9657	-1.2119
12.9519	0.9492	-0.2139	13.7530	0.2036	-0.4422	13.0141	0.9690	-0.8927	13.8343	0.2294	-0.9148	13.0047	0.9660	-1.2106
12.9744	0.9563	-0.2390	13.7537	0.2038	-0.4394	13.7123	0.1907	-0.7727	13.8349	0.2296	-0.9130	13.0053	0.9662	-1.2150
12.9751	0.9566	-0.2380	13.7810	0.2125	-0.4263	13.7130	0.1909	-0.7721	13.8448	0.2328	-0.9163	13.0183	0.9703	-1.2227
12.9758	0.9568	-0.2329	13.7816	0.2127	-0.4291	13.7551	0.2043	-0.7522	13.8455	0.2330	-0.9126	13.0189	0.9705	-1.2212
12.9954	0.9630	-0.2114	13.7922	0.2161	-0.4187	13.7558	0.2045	-0.7539	13.8814	0.2444	-0.9019	13.0300	0.9740	-1.2006
12.9960	0.9632	-0.2505	13.7928	0.2163	-0.4248	13.7830	0.2131	-0.7415	13.8821	0.2446	-0.9041	13.0373	0.9763	-1.2175
12.9966	0.9634	-0.2204	13.8062	0.2205	-0.4183	13.7836	0.2133	-0.7440	13.9046	0.2518	-0.8892	13.7166	0.1921	-1.1580
13.0109	0.9680	-0.2497	13.8069	0.2207	-0.4139	13.7942	0.2167	-0.7418	13.9053	0.2520	-0.8943	13.7172	0.1923	-1.1584
13.0322	0.9747	-0.2282	13.8201	0.2249	-0.4037	13.7949	0.2169	-0.7446	13.9148	0.2550	-0.8952	13.7593	0.2056	-1.1462
13.7082	0.1894	-0.0018	13.8207	0.2251	-0.4092	13.8084	0.2212	-0.7316	13.9155	0.2552	-0.8945	13.7599	0.2058	-1.1493

13.7088	0.1896	-0.0092	13.8303	0.2282	-0.4043	13.8090	0.2214	-0.7363	13.9283	0.2593	-0.8905	13.7870	0.2144	-1.1462
13.7510	0.2030	0.0235	13.8310	0.2284	-0.4023	13.8222	0.2256	-0.7353	13.9290	0.2595	-0.8878	13.7876	0.2146	-1.1446
13.7517	0.2032	0.0212	13.8404	0.2314	-0.4009	13.8229	0.2258	-0.7301				13.7983	0.2180	-1.1411
13.7788	0.2118	0.0485	13.8412	0.2316	-0.4005	13.8323	0.2288	-0.7308				13.7989	0.2182	-1.1430
13.7794	0.2120	0.0462	13.8770	0.2430	-0.3764	13.8330	0.2290	-0.7342				13.8124	0.2225	-1.1381
13.7902	0.2154	0.0532	13.8779	0.2433	-0.3785	13.8427	0.2321	-0.7261				13.8130	0.2227	-1.1395
13.7909	0.2157	0.0549	13.9003	0.2504	-0.3670	13.8435	0.2323	-0.7314				13.8263	0.2269	-1.1360
13.8042	0.2199	0.0614	13.9009	0.2506	-0.3706	13.8794	0.2437	-0.7135				13.8270	0.2271	-1.1370
13.8048	0.2201	0.0697	13.9108	0.2537	-0.3628	13.8800	0.2440	-0.7198				13.8362	0.2300	-1.1310
13.8181	0.2243	0.0758	13.9114	0.2539	-0.3659	13.9026	0.2511	-0.7091				13.8368	0.2302	-1.1328
13.8188	0.2245	0.0747	13.9234	0.2577	-0.3579	13.9032	0.2513	-0.7151				13.8469	0.2334	-1.1319
13.8284	0.2276	0.0741	13.9241	0.2580	-0.3550	13.9127	0.2544	-0.7046				13.8475	0.2336	-1.1278
13.8290	0.2277	0.0680				13.9134	0.2546	-0.7040				13.8963	0.2491	-1.1250
13.8383	0.2307	0.0871				13.9263	0.2587	-0.7043				13.8969	0.2493	-1.1210
13.8390	0.2309	0.0847				13.9271	0.2589	-0.7027				13.9066	0.2524	-1.1197
13.8733	0.2418	0.0992										13.9073	0.2526	-1.1175
13.8744	0.2422	0.1090										13.9174	0.2558	-1.1108
13.8983	0.2498	0.1174										13.9181	0.2560	-1.1123
13.8990	0.2500	0.1212										13.9304	0.2600	-1.1161
13.9087	0.2531	0.1236										13.9311	0.2602	-1.1129
13.9094	0.2533	0.1234												
13.9213	0.2571	0.1314												
13.9219	0.2573	0.1294												